COO-1195-238

THE REACTION K-PLUS NEUTRON GOES TO K-PLUS PI-MINUS PROTON AT 3.8 GeV/c

BY

DON ALLEN MARSHALL

B.S., University of Idaho, 1966
M.S., University of Illinois, 1967

THESIS

Submitted in partial fulfillment of the requirements
for the degree of Doctor of Philosophy in Physics
in the Graduate College of the
University of Illinois, 1972

Urbana, Illinois
October, 1972

This research was supported in part by the
U.S. Atomic Energy Commission Under Contract
AT(11-1)-1195

DISCLAIMER

COO-1195-238

THE REACTION K-PLUS NEUTRON GOES TO K-PLUS PI-MINUS PROTON AT 3.8 GeV/c

BY

DON ALLEN MARSHALL

B.S., University of Idaho, 1966
M.S., University of Illinois, 1967

THESIS

Submitted in partial fulfillment of the requirements
for the degree of Doctor of Philosophy in Physics
in the Graduate College of the
University of Illinois, 1972

Urbana, Illinois
October, 1972

This research was supported in part by the
U.S. Atomic Energy Commission Under Contract
AT(11-1)-1195

THE REACTION K-PLUS NEUTRON GOES TO K-PLUS PI-MINUS PROTON AT 3.8 GeV/c

Don Allen Marshall, Ph.D.
Department of Physics
University of Illinois at Urbana-Champaign, 1972

The ANL 30-inch bubble chamber was exposed to a separated K^+ beam at 3.8 GeV/c. The 300,000 pictures were scanned for 3 and 4-prong events. After measuring all of the 4-prong events with a stopping track and 61% of the 3-prong events, 4919 events were reconstructed which kinematically fit the reaction $K^+D \rightarrow K^+\pi^-PP$; this cross section was found to be 1.78 ± .10 mb. The reaction is dominated by the quasi-two body interaction $K^+N \rightarrow K^{*o}(890)P$; this cross section was found to be 0.80 ± .07 mb. Results of an analysis of the spin density matrix elements indicate 0^- exchange is dominant. The reaction $K^+N \rightarrow K^{*o}(1420)P$ was examined for the effect reported by Firestone et al.[1] The effect was confirmed, but the interpretation of the effect at 3.8 GeV/c as a broad S-wave resonance is clouded by a possible interpretation involving a secondary scattering between the spectator proton and the decay products of the K*(1420).

1. A. Firestone, G. Goldhaber and D. Lissauer, Phys. Rev. Letters 26, 1460 (1971).

ACKNOWLEDGEMENTS

It is a pleasure to acknowledge the many people who have helped make this thesis possible. First I want to thank my adviser Professor T. A. O'Halloran who has given me much insight into experimental particle physics. Also I want to thank Professor B. I. Eisenstein, who was a co-sponsor of the experiment. I want to thank Dr. J. Kim for many helpful discussions concerning the cross section determination and for many helpful comments following a careful reading of the thesis. I want to thank my colleagues, Drs. W. R. Moniger and M. R. Robinson, for their help in processing and analysing the data. The support of the University of Illinois Measuring Staff under the direction of Mrs. Mary Jo Pelafas as well as the help of the librarian for the experiment, Mrs. Jo Ann Kazenski, is gratefully acknowledged. I also want to thank Dr. D. V. Brockway for many helpful discussions of the generalized density matrix formalism and Dr. G. D. Chandler for help in data analysis programming.

I greatly appreciate the sympathy and moral support of my wife, Jean, who also volunteered to type the thesis, and the guidance and support of my parents; their confidence in me has always inspired me to try to do my best.

The early part of my graduate program was supported by a National Aeronautics and Space Administration Traineeship in Physics. The final part was supported in part by the United States Atomic Energy Commission under Contract Number AT(11-1)-1195.

TABLE OF CONTENTS

I. INTRODUCTION

During the last ten years the mechanisms producing three and four body final states produced in meson nucleon interactions at laboratory momenta above 1 GeV/c have become qualitatively understood in terms of quasi two body interactions. The general features of these interactions are succintly expressed in terms of Feynman diagrams.

As an example consider reaction I-1 and its Feynman diagram I-2.

$$A + B \rightarrow C + D \qquad \text{I-1}$$

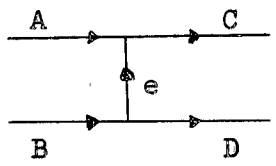

I-2

Here A and B interact forming states C and D either or both of which may decay into one or more particles. The quantum numbers of the states B and D are determined by the quantum numbers of the incident particles A and B and the quantum members of the virtual intermediate state e. The virtual nature of the exchanged particle e means that it will carry little momentum from particle B to particle A; hence in the center of momentum frame for the reaction the momentum of C (D) is nearly the same as the momentum A (B).

The allowed quantum numbers of the particles in the Feynman diagram has been systematized by group theory in terms of SU3. The momentum transfer of the virtual intermediate state e has been systematized by Regge theory.

Although these two models have provided a qualitative formalism for understanding three and four body final states, their predictive power is disappointing. Basically the problem is that many virtual states, e, are allowed in reaction I-1. Hence many parameters are brought into any mathematical description for reaction I-1. Although at high energies there is reason to believe that only a few parameters will be important, unfortunately this is not true for reactions between 1 and 10 GeV/c. Fortunately the formalism does relate different reactions. Hence by studying related reactions there is the possibility of establishing the values of the parameters. At the present time more data is still needed.

This thesis forms a part of a continuing effort by laboratories all over the world to gather more data on quasi two body interactions in the laboratory momentum range above 1 GeV/c. In particular this thesis is a report on a 300,000 picture exposure of the 30" MURA bubble chamber to a separated K^+ beam at 3.8 GeV/c. During the exposure the bubble chamber was filled with deuterium. The pictures were scanned for three and four-prong events. After measuring all of the four-prong events with a stopping track and about 65% of the three-prong events, 4830 events were found which fit reaction I-3.

$$K^+N \rightarrow K^+\pi^-P \qquad \text{I-3}$$

In this reaction the $K^+\pi^-$ system is the only two body final state which shows any significant structure. The $K\pi$ system is dominated by $K^{*o}(890)$ production although there is some $K^{*o}(1420)$ production. The

decay angular distribution of the $K\pi$ system suggests that pion exchange is dominant.

In contrast reaction I-4 shows structure in the $K^+\pi^-$, $P\pi^+$ and $K^+\pi^+\pi^-$ systems.

$$K^+P \rightarrow K^+\pi^-\pi^+P \qquad \text{I-4}$$

For those events where the $P\pi^+$ system lies in the region of the Δ^{++}, a large fraction of the events appear to be described by reaction I-5 (for example see Abrams et al.[1])

$$K^+P \rightarrow K^+\pi^-\Delta^{++} \qquad \text{I-5}$$

Pion exchange dominates this reaction. Because of the large mass of the Δ^{++} reaction I-5 is kinematically restricted to higher values of momentum transfer than reaction I-3, especially at high $K\pi$ masses.

In contrast to both reactions I-3 and I-5, ω exchange appears to be the dominant exchange mechanism for the production of the $K^0\pi^+$ system in reaction I-6 (see for example Shufeldt[2]).

$$K^+P \rightarrow K^0\pi^+P \qquad \text{I-6}$$

This reaction also shows structure in both the $K^0\pi^+$ and $P\pi^+$ systems.

The K^+N reaction I-3 offers an opportunity to study the $K\pi$ system which has been produced by pion exchange and which is free of backgrounds from other channels.

In the past the $K\pi$ system in reactions I-3 and I-5 have been studied by Chew Low extrapolation techniques.[3] This method consists of extrapolating to the pion pole and then parameterizing $K\pi$ scattering in terms of phase shifts. Chapter IV develops an alternative method for studying the mass dependence of the decay angular distributions of the $K^+\pi^-$ system. The method is found to have some definite advantages. However unphysical values of some of the density matrix elements suggest that the method could be improved if the density matrix elements were written down in terms of amplitudes.

SU3 suggests that there may be an S-wave enhancement in the $K\pi$ system and Regge theory suggests that it may lie under the $K^{*o}(1420)$. Firestone et al.[4] has found evidence for an enhancement in the $K^{*o}(1420)$ region for reaction I-3. Although the effect seen by Firestone et al. at 12 GeV/c was also seen in this experiment, no conclusive result could be reached. The data does, however, suggest that a broad S-wave enhancement may be present.

Both S and P-waves in the $K\pi$ system contribute to the $K\pi$ mass plot in the $K^{*o}(890)$ region. Models such as one pion exchange with absorption make predictions about the P-wave density matrix elements[5] while models such as the Reggeized one pion exchange model of Abrams and Maor make predictions about only one of the P-wave density matrix elements.[6] For this reason it is important to develop methods of studying the contribution of the S and P-waves separately. In Chapter VI this was done using the method of Chapter IV. The t dependence of the P-wave was compared with the predictions of the above two models and found in fair agreement with them.

Reaction I-3 and reaction I-7 are very closely related since the same t-channel exchanges are allowed in both reactions and since the couplings of the exchanges are equal within a sign.

$$K^-P \rightarrow K^-\pi^+N \qquad \text{I-7}$$

For this reason a model for quasi two body interactions should be able to explain both reactions. Chapter VII compares these two reactions by comparing the data from this experiment with the corresponding data from a K^-P experiment at 3.9 and 4.6 GeV/c.[7]

II. EXPERIMENTAL PROCEDURE

A. Data Acquisition

The experiment is based upon an exposure of nearly 300,000 pictures in the MURA 30" bubble chamber filled with deuterium at the Argonne 7° separated meson beam. A good description of the beam transport system and the bubble chamber may be found in a Ph.D. Thesis by J. Park.[8]

B. Scanning

Non physicists scanned the film for all event types except for one-prong events without vees. The scanning was supervised by physicists using the Illinois Master Event Library System.[9]

Of the 263 rolls of film in the experiment 141 rolls were double scanned. For each event the Master Event Library System generated a record for the results of each of the two scans and an "indicative" record which contained all the information necessary to identify the event. A list of discrepancies between the two scans was generated and a scan of these events was made by a discrepancy scanner. The result of this scan was used to update the "indicative" record.

At the end of the experiment it was discovered that some double-scanned events contained no record of the first and second scans. This arose in two ways. In the first case the discrepancy scanner found an event or events in a frame for which neither of the first two scans was correct. In this case it was easier to rescan the frame thereby deleting the records of each of the first two scans. In the second case a measurer

decided that the event was wrongly identified. In fixing up the indicative record, information about the previous scans was lost.

Since the double-scanned events were used to calculate the scanning efficiency, the loss of information about the results of each scan means an uncertainty is introduced into the calculation of the scan efficiencies. The simplest solution is to divide the events without any scan information in the same ratio as events found by scan one only, scan two only and both scans. An upper limit on the error for the scan efficiency may be found by assuming that half of the events without scan information records were found by each of the two scans. Table II-1 gives the numbers of events in 52 double-scanned rolls in the last half of the experiment and the efficiencies for these rolls. The calculation of the efficiency uses the assumption that the scans are independent so that the efficiency for an event being found by both scans is just the product of the efficiencies for each of the single scans. Hence the total number of events which is unknown is given by equation II-1.

$$\text{Total number of events} = \frac{\left(\begin{matrix}\text{number of events}\\ \text{found by scan 1}\end{matrix}\right)\left(\begin{matrix}\text{number of events}\\ \text{found by scan 2}\end{matrix}\right)}{\text{number of events found by both scans}} \qquad \text{II-1}$$

The single scan efficiency ϵ_s is given by equation II-2.

$$\epsilon_s = \tfrac{1}{2}\,\frac{\left(\begin{matrix}\text{number of events}\\ \text{found by scan 1}\end{matrix}\right)+\left(\begin{matrix}\text{number of events}\\ \text{found by scan 2}\end{matrix}\right)}{\text{total number of events}} \qquad \text{II-2}$$

The double scan efficiency, ϵ_d, is the efficiency that an event will be found by either scan; ϵ_d is given by equation II-3 which calculates the probability that an event will be unfound after two scans.

	events found by both scans	events found by scan 1 only	events found by scan 2 only	events without scan information	single scan efficiency	double scan efficiency	overall scan efficiency
3-prong	4291	423	415	145	.911 ± .019	.992 ± .004	.951 ± .009
4-prong with stopping track	2505	211	163	77	.931 ± .018	.995 ± .003	.965 ± .009

TABLE II-1. Table II-1 shows the number of events found by both scans, by scan one, by scan two and the number of events without scan information records for 52 double scanned rolls of film in the last half of the experiment. The single and double scan efficiencies and errors as well as the overall scan efficiency for the entire experiment is also given. The calculation of these efficiencies and their errors is described in the text.

$$1 - \epsilon_d = (1-\epsilon_s)^2 \qquad \text{II-3}$$

If F is the fraction of the film double scanned, then the overall scanning efficiency, ϵ_T, is given by equation II-4.

$$\epsilon_T = F\ \epsilon_d + (1-F)\ \epsilon_s \qquad \text{II-4}$$

The three-prong events were measured on only 167 rolls. Of these rolls only 83 were double scanned. Consequently for the four-prong events F is .536 while for the three-prong events it is .497.

A study of the efficiencies shows that the efficiency is lowest for frames with two or more events. Moreover these frames also contain a larger portion of events without scan information.

The errors on the efficiencies were calculated for frames with only one event as well as for frames with two or more events. The error appearing in Table II-1 is the maximum of the errors calculated. This error is taken as an upper limit to the error on the scanning efficiencies.

C. Path Length

The number of beam tracks entering the up-stream end of the scanning volume was recorded every fiftieth frame. The average number of beam tracks for the entire experiment was 10.56 ± .05 per frame.

An event was taken as being in the fiducial volume providing its x coordinate lay between -22.0 and 22.0 cm where the beam travels primarily in the direction of increasing x. The lower edge of the fiducial volume was taken because it was observed at x equal -22 cm that the number of

fit 4C three and four-prong events started dropping off. The upper edge of the fiducial volume was taken because it was observed that at x equal 22 cm, the number of constraint reductions abruptly rose owing to the fact that the SMP mirror arrangement prevented long measurements of one or more outgoing tracks.

The path length inside the fiducial volume was calculated from the average beam track angles for events at the beginning and end of the fiducial volume. The average path length was 45.08 ± .20 cm.

The total number of good pictures was 294,407.

The total fiducial track length was $(1.402 \pm .009)\ 10^8$ cm.

Moninger[10] examined the pion contamination and concluded that it was less than 1%. This estimate agrees well with a more careful study of the pion contamination in the Argonne 7° beam made by Eisenstein[11] at a slightly lower energy of 3.2 GeV/c.

D. Density of Deuterium

The density of deuterium was found by measuring the range of muons from pion decays. The equivalent density of hydrogen was then adjusted until the range-momentum tables gave the correct muon momentum. The deuterium density was found to be .134 ± .005 gm/cm^3. The corresponding density of scattering centers, ρ_{sc}, is $(4.00 \pm .15)\ 10^{22}$/cm^3.

E. Attenuation

As the beam traverses the chamber, it decays and interacts; hence the beam intensity is attenuated. The attenuation factor, A, takes into account this depletion of the beam. The attenuation of the beam is given by equation II-5.

$$A = \frac{1}{L}\int_0^L e^{-Bx}\,dx = (1 - e^{-BL})/(BL)$$

$$B = \sigma_t \rho_{sc} + \frac{1}{\gamma c\tau}$$

σ_t = total K^+D interaction cross section[12]
= 34.1 ± .3 mb at 3.3 GeV/c

$c\tau$ = (370.2 ± 1.2)cm II-5

$\gamma = E_{beam}/m_K$ = 7.760 ± .076

L = average path length of a beam track
= 45.08 ± .20 cm

ρ_{sc} = (4.00 ± .15) $10^{22}/cm^3$

From the data following equation II-6, B is calculated to be (1.71 ± .05) 10^{-3}/cm. The attenuation factor, A, is then found to be .962 ± .001.

F. Measurement Efficiency

The events were measured at the University of Illinois on SMP's which were connected on line to the CSX-1 computer. The measurements were processed through the standard University of Illinois reconstruction and fitting programs, SPACE[8] and ILLFIT,[13] on an IBM 7094 computer.

1. Four-Prong Events with Stopping Tracks

After processing the four-prong events with a visible stopping track, it was found that .141 ± .008 of the events either lay outside the fiducial volume or should not have been included in the data sample

due to scanning errors. Events which failed or got no fit or which were missed by the first measurement pass were remeasured. It was found that .992 ± .001 of the good events were measured. For those events which were measured, the measurement efficiency was calculated as one minus the ratio of N_R to N_T where N_R is the number of events which failed in the fitting or reconstruction program and N_T is the total number of events. The measuring efficiency was calculated to be .92 ± .02.

2. Three-Prong Events

The three-prong events contain tau decays as well as interactions with the deuterium. At the scanning stage a template was used to classify events as possible candidates for tau decays. After processing the tau candidates, it was found that .139 ± .016 of the events either lay outside the fiducial volume or should not have been included in the data sample due to scanning errors. Events which failed or got no fit or which were missed by the first measurement pass were remeasured. It was found that .995 ± .001 of the good events were measured. For the measured events, the measurement efficiency was calculated as was done for the four-prongs. The measurement efficiency was found to be .91 ± .03. Only .0092 ± .0018 (27 events) of the tau candidates fit the final state $PPK^+\pi^-$.

After processing the three-prong non tau candidates, it was found that .142 ± .003 of the events lay outside the fiducial volume or should not have been included in the data sample due to scanning errors. Only .612 ± .004 of the three-prong non tau candidates were measured. The measurement efficiency was found to be .83 ± .02.

Since the tau candidates amount to about .11 of the three-prong events and since less than .01 of the tau candidates fit the final state $PPK^+\pi^-$, the tau candidates can be ignored when the measurement efficiency is calculated for the events leading to the final state $PPK^+\pi^-$.

G. Hypothesis Selection

Table II-2 shows the hypotheses tried in fitting the three-prong and the four-prong events with a visible stopping track. For the three-prong events the unfitted momentum of the unseen spectator was set to 0. ± 30 MeV/c in the x and y directions and 0. ± 40 MeV/c in the z direction. For the four-prong events, the momentum of the stopping tracks shorter than about 5 cm was determined by range-momentum tables while for longer stopping tracks the momentum was determined by both range-momentum tables and curvature.

When there were several fits for an event, the fits were ranked according to their likelihood, which is defined to be the chi square probability times the cube of the number of constraints. In the case of missing mass fits which have zero constraints, the likelihood was set to .1. Fits were considered ambiguous if their likelihoods were within a factor of 25 of each other.

All of the four-prong events with fits, except for the missing mass fits, and all of the three-prong events with fits having no missing neutral particle were ion scanned in order to eliminate fits which were inconsistent with the bubble densities of the tracks. According to Robinson[14] about 2% of the events were misidentified after the ion scan. Whenever a fit with no missing neutral particles was ruled inconsistent, the event was ion scanned again.

Hypotheses for 3-prong events

$$K^+ \rightarrow \pi^+\pi^+\pi^-$$

$$K^+D \rightarrow P(P_s)K^+\pi^-$$

$$K^+D \rightarrow P(P_s)K^+\pi^-(\pi^o)$$

$$K^+D \rightarrow P(P_s)\pi^+\pi^-(K^o)$$

$$K^+D \rightarrow P(P_s)K^+K^-(K^o)$$

$$K^+D \rightarrow (D)K^+\pi^+\pi^-$$

$$K^+D \rightarrow (P_s)(N)K^+\pi^+\pi^-$$

Hypotheses for 4-prong events with stopping track

$$K^+D \rightarrow PPK^+\pi^-$$

$$K^+D \rightarrow PPK^+\pi^-(\pi^o)$$

$$K^+D \rightarrow PP\pi^+\pi^-(K^o)$$

$$K^+D \rightarrow PPK^+K^-(K^o)$$

$$K^+D \rightarrow P(N)K^+\pi^+\pi^-$$

$$K^+D \rightarrow P(N)K^+K^-(K^o)$$

$$K^+D \rightarrow DK^+\pi^+\pi^-$$

$$K^+D \rightarrow DK^+K^+K^-$$

TABLE II-2. Table II-2 shows the hypotheses tried for four-prong events with a stopping track and three-prong events. The tracks in parentheses represent particles that are not associated with a measured track.

For events in the final data sample, it was found that the 4C hypothesis, $K^+D \rightarrow K^+\pi^-PP_s$, was unambiguous with any other hypothesis for 90.9% of the three-prong events and 95.4% of the four-prong events. It was found that a hypothesis with a missing neutral ranked higher than the 4C for 1.2% of the three-prong events and 0.7% of the four-prong events. A 4C hypothesis was always chosen over a hypothesis with a missing neutral. Another ambiguity arises when there are two fast positive tracks; then the hypothesis $K^+D \rightarrow K^+\pi^-PP_s$ may be ambiguous with itself. This ambiguity in the rest of this section will be referred to as a 4C-4C ambiguity. There was a 4C-4C ambiguity for 5.6% of the three-prong events and 1.6% of the four-prong events. These 4C-4C events tend to populate high $K^+\pi^-$ masses. In all cases of 4C-4C ambiguities, the fit with the higher likelihood was accepted.

H. Fitting Efficiency

The fitting efficiency for the final state $K^+\pi^-PP$ was determined by remeasuring and then fitting ion scanned fits which were inside the fiducial volume and which had a likelihood greater than 0.3. Out of 152 three-prong events the fitting efficiency was found to be .99 ± .02. Out of 132 four-prong events the fitting efficiency was found to be .98 ± .02.

A plot of the number of events versus chi squared probability should be flat according to the theory of statistics. All bubble chamber experiments, however, find an excess of events with very low chi squared probability. Some of the events in this low probability tail are spurious fits. Good events show a K*(890)peak, while spurious events should have

a relatively featureless mass plot. By looking at the strength of the K*(890) signal as a function of likelihood, it was found that for likelihoods less than 3.9 for three-prong events and less and 0.3 for four-prong events, the K*(890) signal starts to decrease. Once a likelihood cut has been imposed, it is necessary to estimate the number of good events lost. This was done by assuming that for good events the K*(890) signal to background is independent of likelihood while spurious events will not exhibit a K*(890) signal. A background subtraction was then used to determine the number of good events in the low likelihood region. Using this estimate it was possible to calculate the fraction of the good events lost by accepting events with a likelihood larger than some fixed limit. For three-prong events, it was found that .939 ± .012 of the good fits will be seen if only fits with a likelihood greater than 3.9 are accepted. In the case of the four-prong events with a stopping track, it was estimated that .932 ± .012 of the good fits will be seen if only fits with a likelihood greater than 0.3 are accepted.

I. Corrections Resulting from the Use of Deuterium as a Source of Neutrons

The deuteron is a weakly bound (2.2 MeV) neutron proton system which is an isospin singlet, spin triplet and has orbital angular momentum zero with a small admixture of orbital angular momentum two. To a first approximation for interactions at high lab momenta, only one of the nucleons interacts. Therefore the momentum distribution of the other nucleon, the spectator, may be predicted from the wave function of the deuteron. This is the impulse approximation.

The impulse and closure approximation modifies the predictions of the impulse approximation to take into account the effect of the Pauli

Exclusion Principle when a nucleon charge exchange takes place. A detailed treatment may be found in a thesis by W. Lee.[15] The impulse and closure approximation predicts that the differential cross section will be given by equation II-6.

$$\frac{d\sigma}{dt} = (1-H)\left.\frac{d\sigma}{dt}\right)_{nf} + (1-H/3)\left.\frac{d\sigma}{dt}\right)_{f} \qquad \text{II-6}$$

Here H is a form factor which equals 1 when t equals 0. The subscript f means spin flip and nf means spin non flip. Although H is still above 0.15 for t as large as $0.1(\text{GeV/c})^2$, the differential cross sections for quasi two body interactions can not be corrected for the variation of the form factor until a specific model is assumed to predict the spin flip and spin non flip amplitudes.

The finite size of the nucleons means that sometimes one of the nucleons will shield the other. This is called Glauber Screening.[16] Moninger[10] has calculated the effect for Glauber screening at 3.8 GeV/c and found that the observed cross section off deuterium is a factor $0.984 \pm .014$ smaller than the cross section would be off a neutron alone.

The motion of the target nucleon inside the deuterium nucleus has two effects. The first of these is that the center of momentum energy is not unique but rather smeared out. For 3.8 GeV/c the width of the center of momentum energy distribution is about 140 MeV. The second effect is that for a spectator moving in the beam direction, the target nucleon will be moving so that the flux is larger than when the spectator is moving back along the beam direction. This effect biases the spectator distribution so that it is not isotropic as would be expected from the impulse approximation.

When the experimental spectator momentum distribution is compared with the distribution predicted by the Hulthen[17] wave function, it is seen that there is an excess of events with momenta larger than about 250 MeV/c. This excess is usually attributed to double scattering in the deuteron. In discussing reactions such as $K^+D \rightarrow PPX^o$ it is clear that all events in the tail of the spectator distribution should be included. However when reactions such as $K^+N \rightarrow PX^o$ are discussed, it is less clear what should be done. Two approaches are possible; the first includes the tail while the second chops off the tail at 250 or 300 MeV/c. The second approach appears to be the more popular in the literature of the reaction $K^+N \rightarrow K^+\pi^-P$.

J. Spectator Escape Correction

Since only four-prong events with a visible stopping track were measured, it is necessary to correct for those events where neither proton was observed to stop. This was done by comparing the spectator distribution of this experiment with the distribution found in a π^+D experiment at 3.65 GeV/c [17] in which all four-prong events were measured regardless of whether there was a stopping track. Below 250 MeV/c a proton has a range of less than 8 cm; hence virtually all such spectators will stop inside the chamber. Because of differences in treating very short spectators, a cut on spectator momentum less than 110 MeV/c was made on the two distributions. Table II-3 shows the numbers of events found by the two experiments for different spectator momentum regions and predicts the number that would have been found by this experiment if all four-prong events had been measured.

P_s in MeV/c	Number of 4-prong events in π^+D at 3.65 GeV/c	Number of 4-prong events with a stopping track for K^+D at 3.8 GeV/c	Predicted number of 4-prong events in K^+D at 3.8 GeV/c if all 4-prong events had been measured
0-110	631	814	814
110-250	961	1563	1563
250-300	162	168	264
250-∞	723	265	1176

TABLE II-3. Table II-3 compares the spectator distributions as a function of momentum for a π^+D experiment at 3.65 GeV/c where all four-prong events were measured with this experiment where only four-prong events with a stopping track were measured and with the predicted number of four-prong events that would have been measured if all four-prong events had been measured in this experiment.

According to the impulse approximation, the interaction with the neutron should be independent of the spectator momentum distribution. Hence the spectator escape correction becomes especially simple since it merely involves scaling up the number of four-prong events with a stopping track to the number predicted if all four-prong events had been measured. The scale factor is 1.34 ± .05 for all four-prong events. If the spectator momentum is required to be less than 300 MeV/c, the scale factor is 1.04 ± .05.

K. Microbarn Equivalents

The microbarn equivalent is calculated by equation II-7.

$$n \frac{\text{event}}{\mu b} = \rho_{sc} L_f A 10^{-30} \qquad \text{II-7}$$

ρ_{sc} = density of scattering centers
= $(4.00 \pm .15) 10^{22}$ cm^{-3}

L_f = total beam track length in the fiducial volume
= $(1.402 \pm .009) 10^8$ cm

A = attenuation factor
= 0.962 ± .001

The microbarn equivalent is calculated to be 5.39 ± .22 events/μb.

When the various efficiencies are taken into account, the microbarn equivalent for three-prong events is found to be 2.41 ± .13 events/μb. The microbarn equivalent for four-prong events with a stopping track is 4.36 ± .23 events/μb; adding the spectator escape correction, the

microbarn equivalent is 3.25 ± .21 events/μb for all spectators and 4.19 ± .30 events/μb for spectators with momentum less than 300 MeV/c.

L. Spectator Distributions

Figure II-1 is a plot of the spectator momentum; the curve which is normalized to the area is the prediction of the Hulthen wave function.[18] The predicted distribution is given by equation II-8.

$$\frac{d\sigma}{dP_s} = C\, P_s^2 \left(\frac{1}{P_s^2 + \alpha^2} + \frac{1}{P_s^2 + \beta^2} \right) \qquad \text{II-8}$$

C is a constant

P_s is the spectator momentum

$\alpha = 45.778$ MeV/c

$\beta = 5.18\,\alpha$

The values of α and β are those given by Moravcsik.[18] The shaded area in Figure II-1 is the contribution of the four-prong events.

The agreement with the theoretical distribution for the spectator momentum distribution is fair. There are two sources of deviation from the theoretical distribution. The first arises at low momentum from the kinematic fitting of the three-prong events where the spectator momentum is initially set to zero with an error on P_x and P_y of 30 MeV/c and an error on P_z of 40 MeV/c. The second arises at high momentum from double scattering and rescattering of one of the final state particles with the spectator.

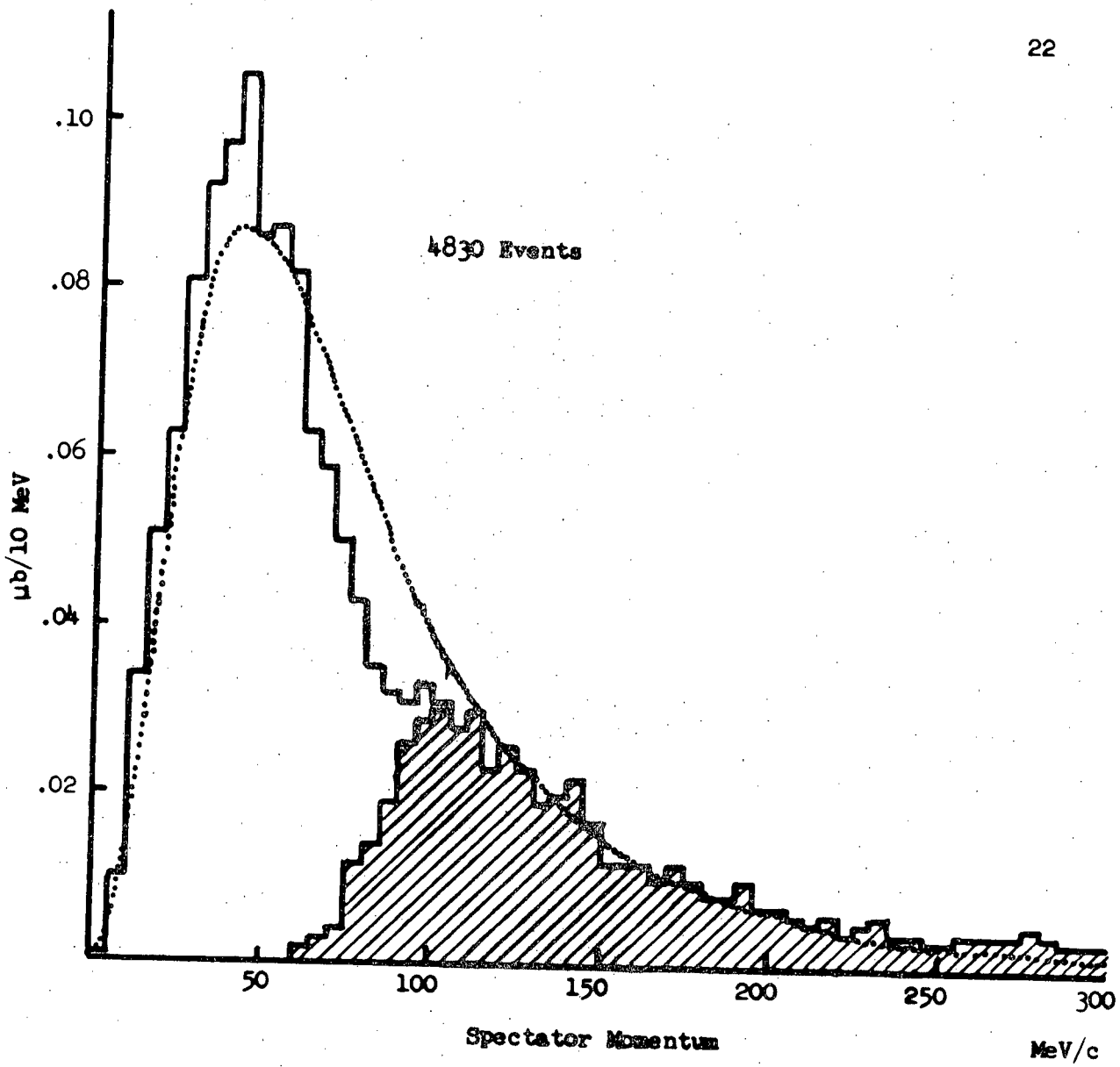

FIGURE II-1. Figure II-1 is a plot of the spectator momentum; the curve which is normalized to the area is the prediction of the Hulthén wave function. The cross-hatched area is the contribution of the 4-prong events.

Figure II-2a is a plot of cos Θ_z where Θ_z is the angle between the spectator and the normal to the film plane, the z axis. The shaded area is the contribution of the four-prong events. Scanning biases result in a loss of four-prong events when the spectator is traveling up towards the cameras or away from them. The combined plot for three and four-prong events should be flat. With the exception of the first bin for spectators traveling away from the cameras, the agreement is good.

Figure II-2b is a plot of cos Θ_b where Θ_b is the angle between the spectator and the beam. The shaded area is the contribution of the four-prong events. Scanning biases result in a loss of four-prong events when the spectator is hidden by the beam track or by an outgoing track. The combined plot for the three and four-prong events should show the effect of the flux factor which depends upon $(\beta_K - \beta_N \cos \Theta_b)$ where β_K is the beam velocity and β_N is the neutron velocity. The minus sign appears because the spectator velocity is the negative of the neutron velocity in the impulse approximation. With the exception of an excess of some events at small cos Θ_b, the agreement with the impulse approximation is fair.

Figures II-1 and II-2 indicate that the three and four-prong events have been corrected appropriately for differences in scanning and measuring.

M. Cross Section

The cross section for the reaction $K^+D \rightarrow K^+\pi^-PP$ was found to be 1.78 ± .10 mb. There were 4919 events in this sample, 2481 of which

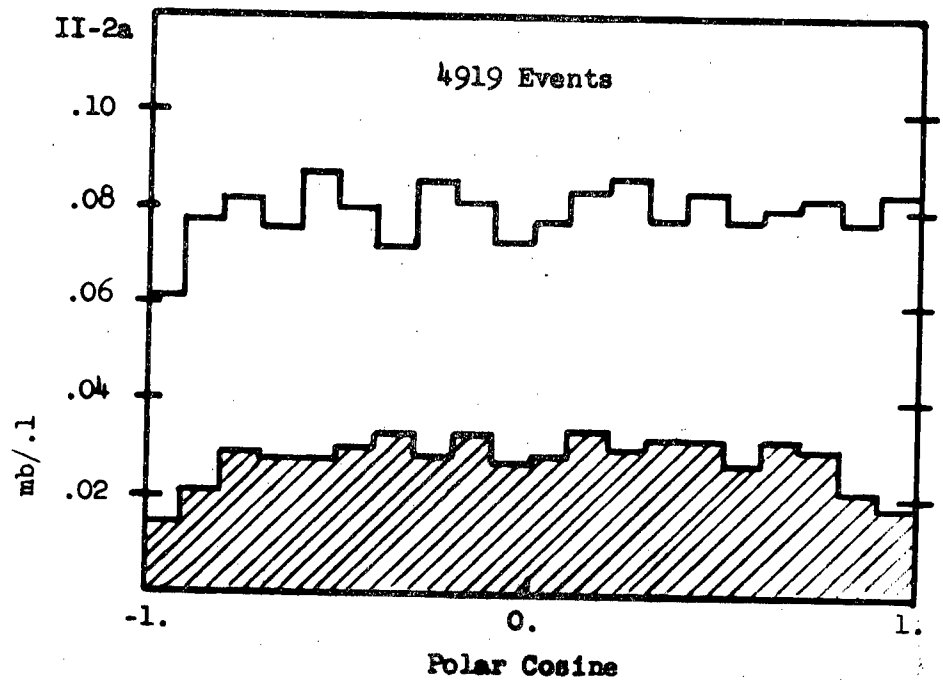

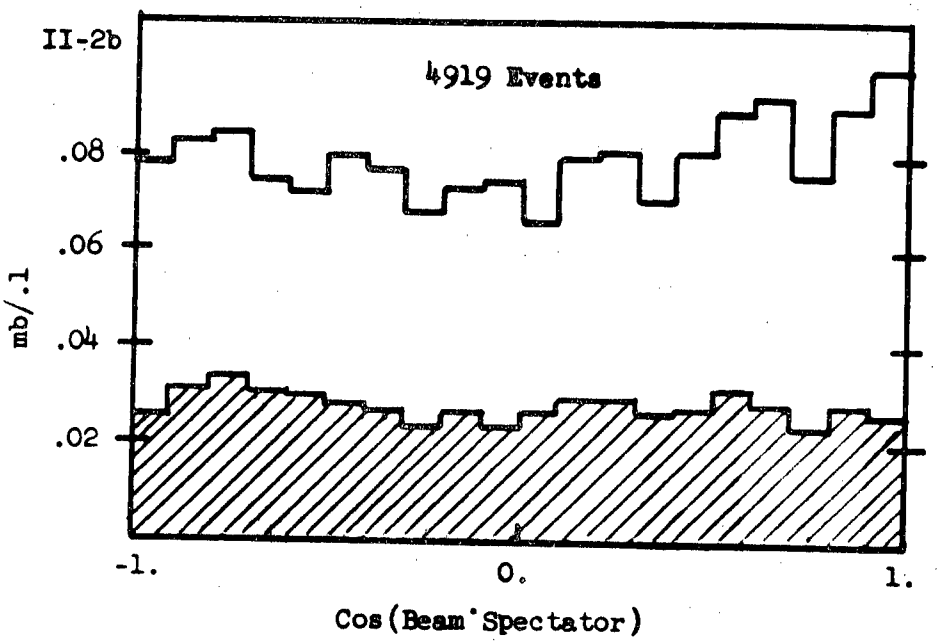

FIGURE II-2. Figure II-2a is a plot of the cosine between the spectator and the normal to the film plane. Figure II-2b is a plot of the cosine between the beam and the spectator. The cross hatched area is the contribution of the 4-prong events.

were three-prongs. The contribution of the four-prongs includes a spectator escape correction.

The cross section for the reaction $K^+N \rightarrow K^+\pi^-P$ was found to be 1.62 ± .11 mb. There were 4830 events in this sample, 2481 of which were three-prongs. The spectator momentum was required to be less than 300 MeV/c and a spectator escape correction was made. A Glauber Screening factor of .984 ± .014 has been taken into account; however no corrections were made for the effect of the Pauli Exclusion Principle.

Table II-4 lists the values of the quantities used to determine the cross section, the percent error on these quantities and the section describing the determination of the quantity.

quantity	odd prong		even prong		section
	value	percent error	value	percent error	
scanning efficiency	.951	0.9%	.965	0.9%	II-B
fraction of film measured	.612	0.6%	.992	0.1%	II-F
measurement efficiency	.83	2.4%	.92	2.2%	II-F
fitting efficiency	.98	2.0%	.99	2.0%	II-H
chi squared probability cut	.94	1.3%	.93	1.3%	II-H
microbarn equivalent	5.39	4.0%	5.39	4.0%	II-K
spectator escape correction for K^+D interaction	---	---	.746	3.7%	II-J
Glauber correction	.985	1.4%	.985	1.4%	II-I
spectator escape correction for K^+N with $P_s<300$ MeV/c	---	---	.962	4.8%	II-J

TABLE II-4. Table II-4 lists the values of the quantities used to determine the cross section, the percent error on these quantities and the section describing the determination of the quantity.

III. GENERAL FEATURES OF THE DATA

A. The Dalitz Plot

The Dalitz plot for the $K^+\pi^-P$ final state, Figure III-1, shows a strong K*(890) band and a weaker K*(1420) band. There is an excess of events at low $P\pi$ mass, but otherwise the $P\pi$ system appears featureless. The lack of a diagonal band is expected since no enhancements have ever been reported in the K^+P system where resonances would be exotic.

B. The $P\pi^-$ System

Figure III-2a shows the neutral $P\pi^-$ mass spectrum for all events; it is dominated by reflections of the $K^+\pi^-$ enhancements. The $P\pi^-$ system has a number of mass regions where enhancements might be expected; in particular there is the $\Delta^0(1236)$ and several N* resonances. A number of attempts were made to check for mass enhancements in the $P\pi^-$ system. Among the cuts tried were forward $P\pi^-$ production, removal of K* regions from the Dalitz plot and backwards decay of the π in the $P\pi^-$ Jackson frame. Figure III-2b shows the results after removing the K* bands and requiring that the π decay backwards in the Jackson frame. Figure III-2c shows the result after removing the K* bands and requiring peripheral production for the $P\pi^-$ system. In Figures III-2b and III-2c there are some hints of enhancements around the region of the $\Delta^0(1236)$, the N*(1520) and the N*(1680) - N*(1688), but none of the hints is of any statistical significance.

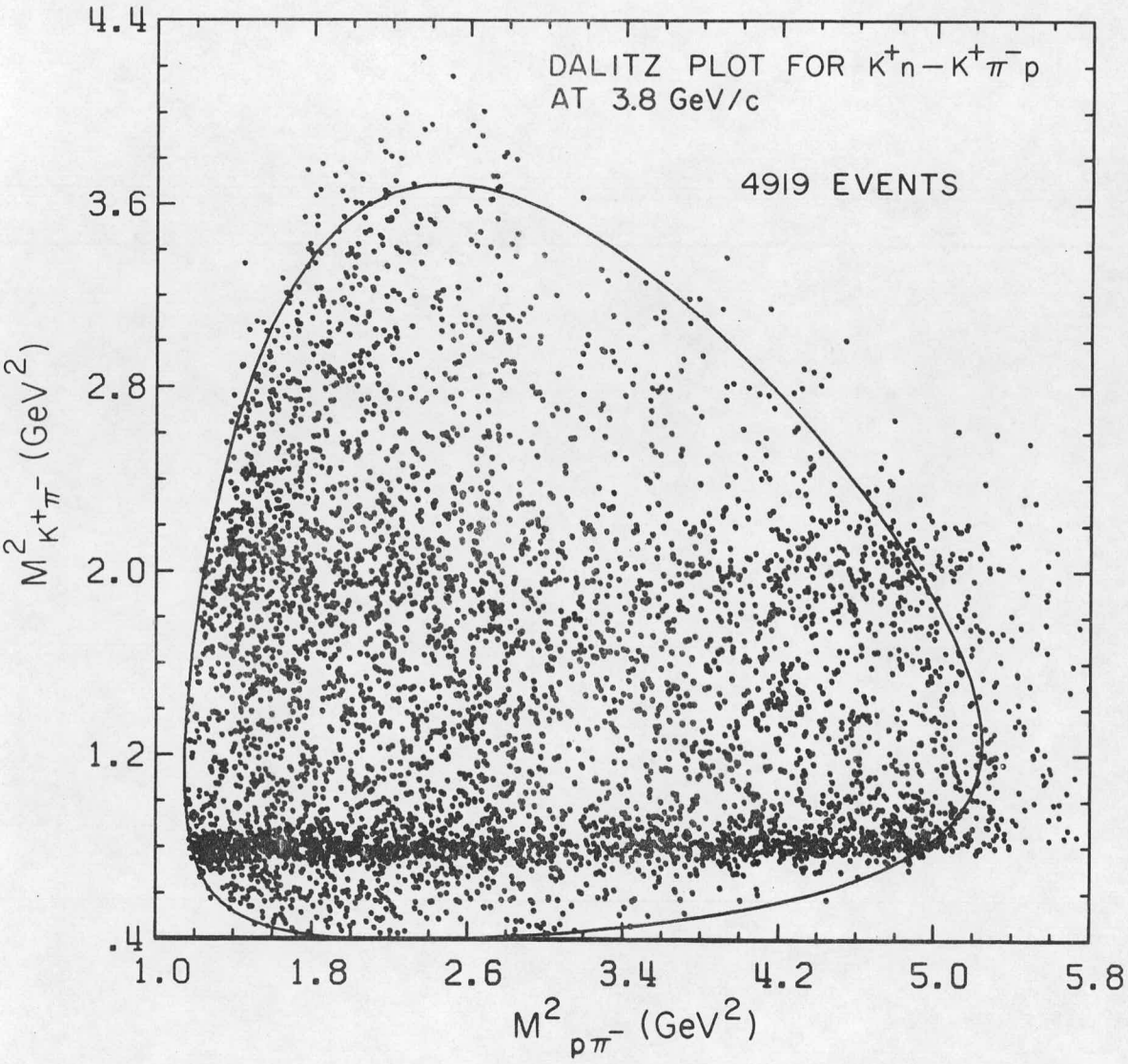

FIGURE III-1. Figure III-1 shows the Dalitz plot for the reaction $K^+N \rightarrow K^+\pi^-P$ at 3.8 GeV/c.

III-2a

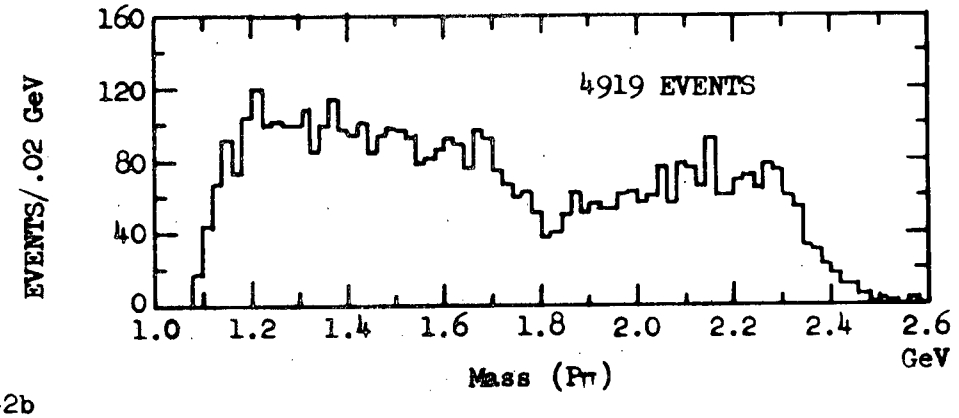

III-2b

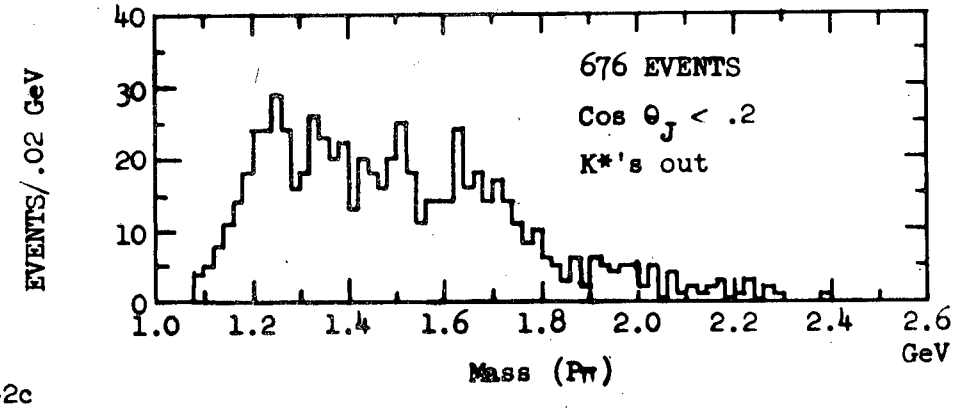

III-2c

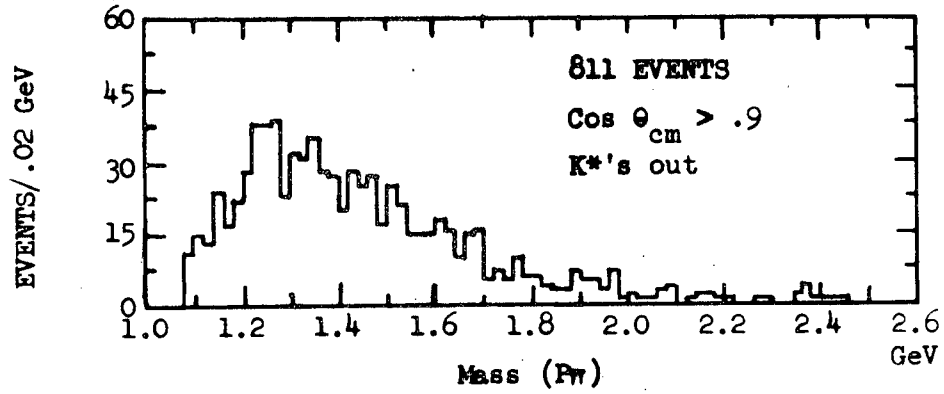

FIGURE III-2. Figure III-2a shows the $P\pi^-$ mass spectrum. Figure III-2b shows the $P\pi^-$ mass spectrum after the K* bands have been removed and for the $P\pi^-$ Jackson cosine less than 0.2 where cosine equal -1. means the π^- is decaying backwards. Figure II-2c shows the $P\pi^-$ mass spectrum after the K* bands have been removed and for the center of momentum production cosine for the $P\pi^-$ system greater than 0.9. The K* bands are defined by the mass of the $K\pi$ system between 0.84 and 0.94 or between 1.32 and 1.55 GeV.

C. The PK^+ System

Figure III-3a shows the PK^+ mass plot for all events; Figure III-3b shows the result after removing events in the K* bands. Other attempts to exhibit structure in the PK system produced results similar to those shown in Figure III-3b.

D. The $K^+\pi^-$ System

From either the Dalitz plot, Figure III-1, or the mass plot of the $K^+\pi^-$ system, Figure III-4, it is seen the K*(890) production is dominant and that there is some K*(1420) production. Fits to the mass plot using a polynomial background and 2 Breit-Wigner's attribute $(36.7 \pm 1.2)\%$ of the mass plot to K*(890) and $(18.4 \pm 1.1)\%$ to K*(1420).

The $K^+\pi^-$ system is produced peripherally. The production distributions for both the K*(890) and K*(1420) regions are shown in Figure III-5; this data has not been corrected for the dip in the forward direction which arises when the Pauli Exclusion Principle is applied to the interaction between the two protons in the final state. The results of exponential fits for the forward slope are shown in Table III-1.

	Mass range	Slope for $\frac{d\sigma}{dt}$	Range of t
K*(890)	(0.84 - 0.94)GeV	$(8.9 \pm .8)/(GeV/c)^2$	$(.02 - .20)\ (GeV/c)^2$
K*(1420)	(1.32 - 1.56)GeV	$(5.1 \pm .4)/(GeV/c)^2$	$(.12 - .66)\ (GeV/c)^2$

TABLE III-1. Table III-1 shows the results of exponential fits for the forward slope.

III-3a

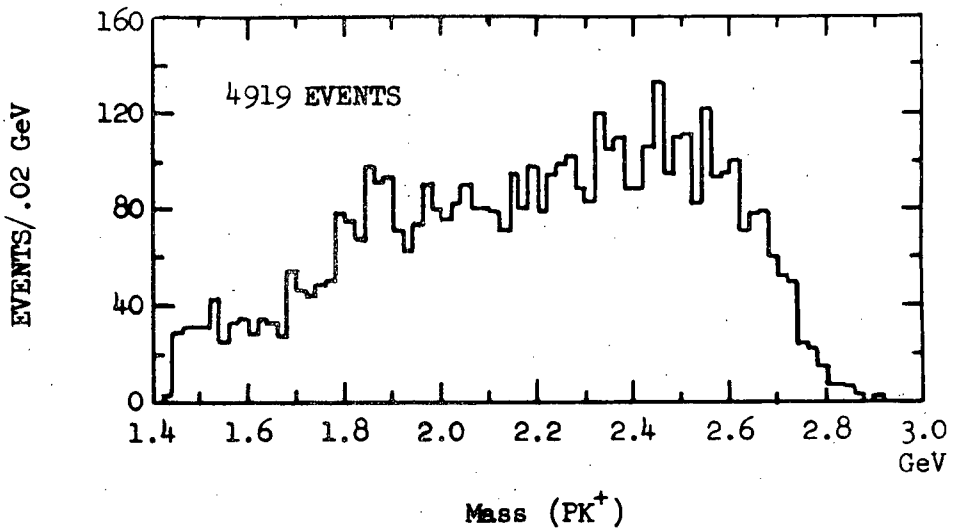

III-3b

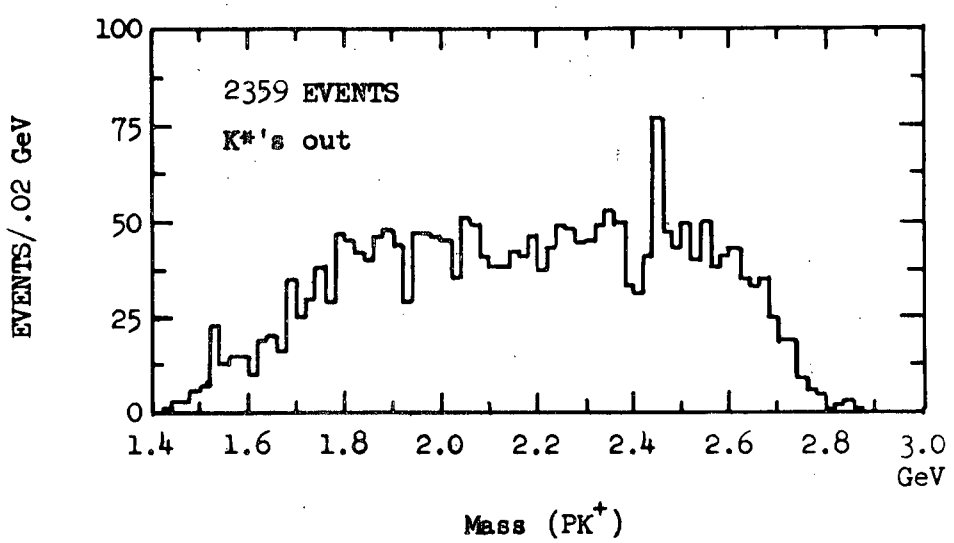

FIGURE III-3. Figure III-3a shows the PK mass spectrum. Figure III-3b shows the PK^+ mass spectrum after the K* bands have been removed. The K* bands are defined by the mass of the $K\pi$ system between 0.84 and 0.94 or between 1.32 and 1.55 GeV.

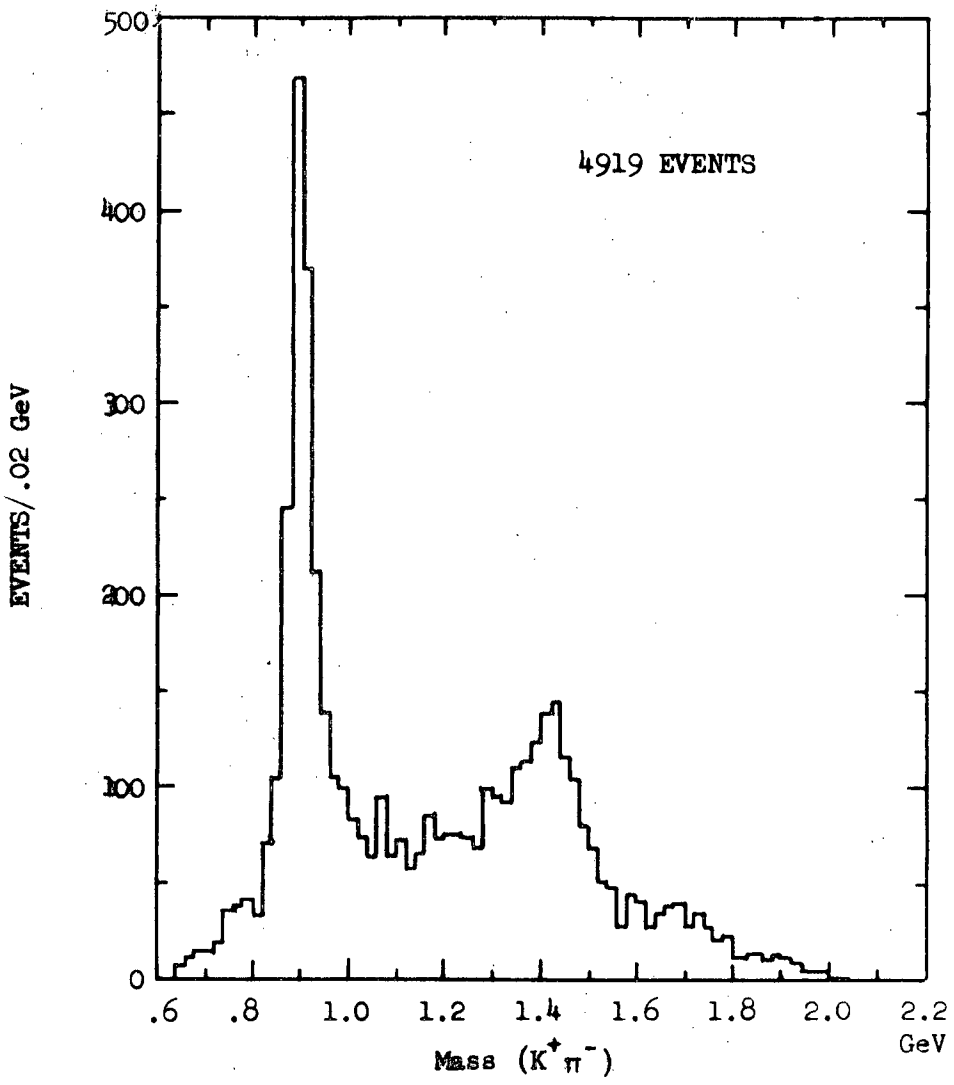

FIGURE III-4. **Figure III-4 shows the $K^+\pi^-$ mass spectrum.**

III-5a

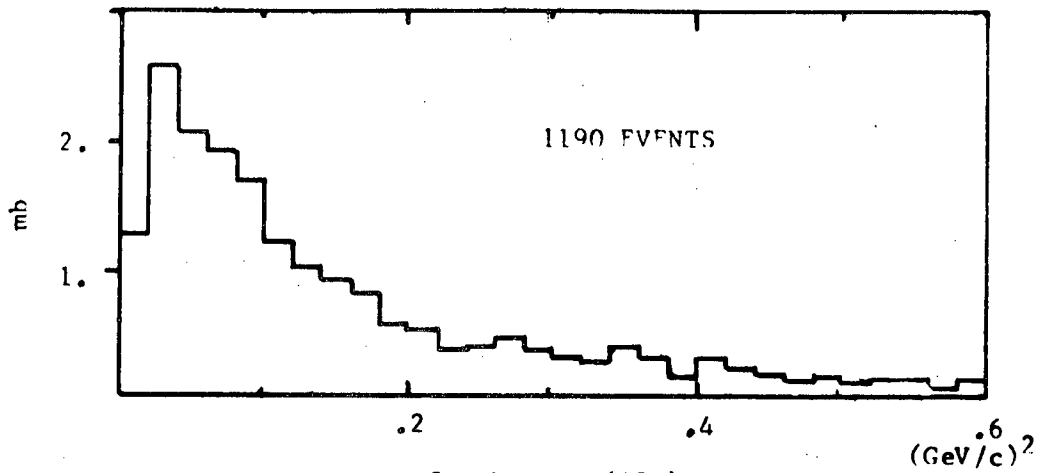

t for K to K*(890)

III-5b

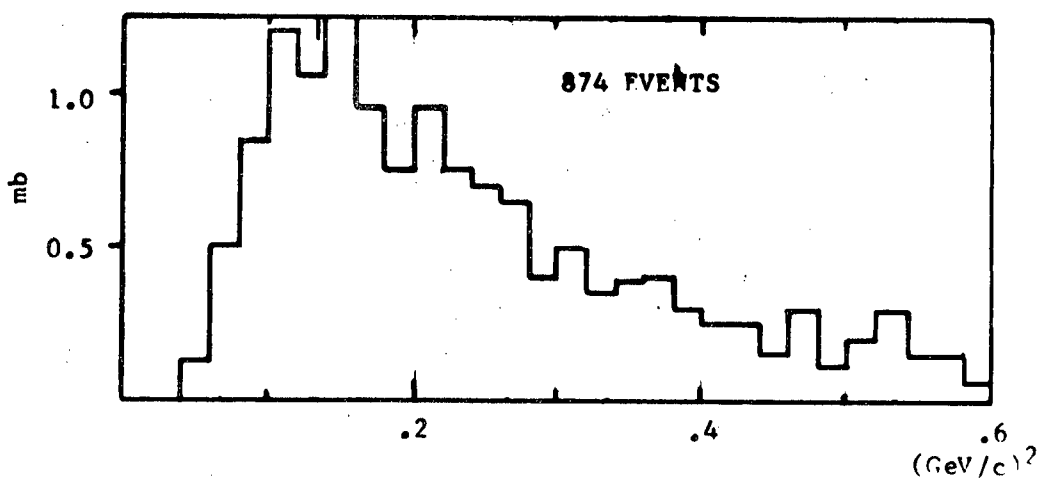

t for K to K*(1420)

FIGURE III-5. Figure III-5a shows the t distribution for the K*(890) region which is defined to be for mass values between 0.84 and 0.94 GeV. Figure III-5b shows the t distribution for the K*(1420) region which is defined by mass values between 1.32 and 1.55 GeV. No corrections have been made at low t for the Pauli Exclusion Principle.

Figure III-6 shows the Jackson decay angular distributions in the K*(890) region while Figure III-7 shows them in the K*(1420) region. General symmetry principles for the decay of a resonance show that the Jackson cosine must be symmetric about 0.0 and that the absolute value of the Jackson phi, Treiman-Yang angle, must be symmetric about 90°. The existence of an asymmetry in the Jackson angles indicates that the dominant partial waves interfere with a background. Ignoring the asymmetries, it is seen that the Jackson phi is relatively flat and that the Jackson cosine is small at the origin and large at the end points. Together these two facts indicate that the density matrix element ρ_{oo} is large and that hence pion exchange is the dominant exchange mechanism.

A closer examination of the $K^+\pi^-$ mass plot reveals that on the low mass side of the K*(1420) there is a shoulder. This shoulder will be examined later in the light of the findings of Firestone et al.[3] who in a K^+D experiment at 12 GeV/c find evidence for an additional resonance in this region.

III-6a

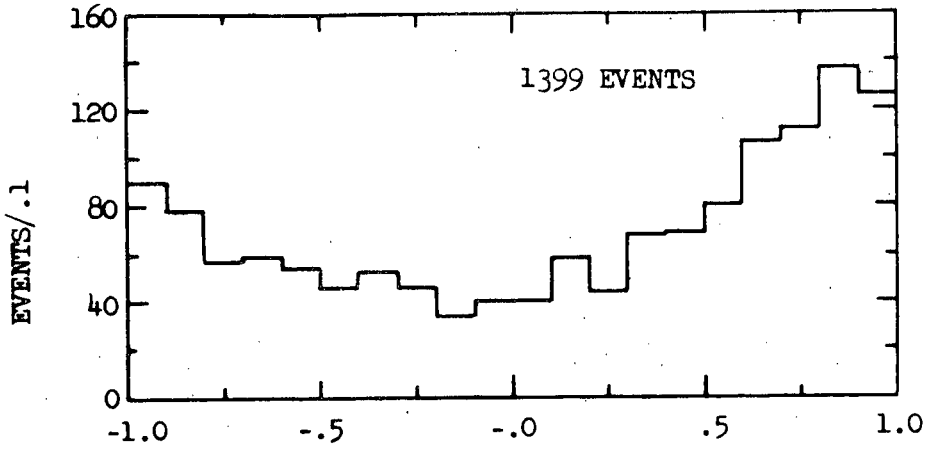

III-6b

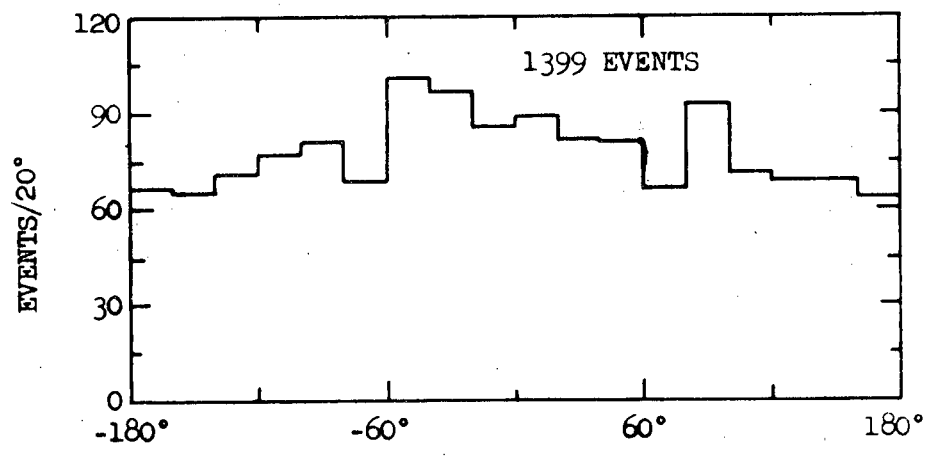

FIGURE III-6. Figure III-6a shows the $K\pi$ Jackson cosine angular distribution in the K*(890) region. Figure III-6b shows the $K\pi$ Jackson phi angular distribution, the Trieman-Yang angular distribution, in the K*(890) region. The K*(890) region is defined by $K\pi$ mass values between 0.84 and 0.94 GeV.

III-7a

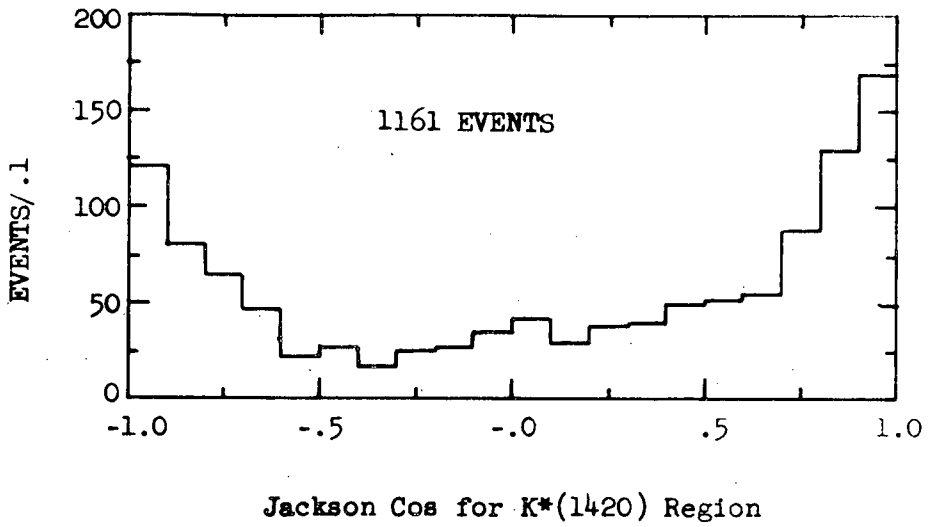

III-7b

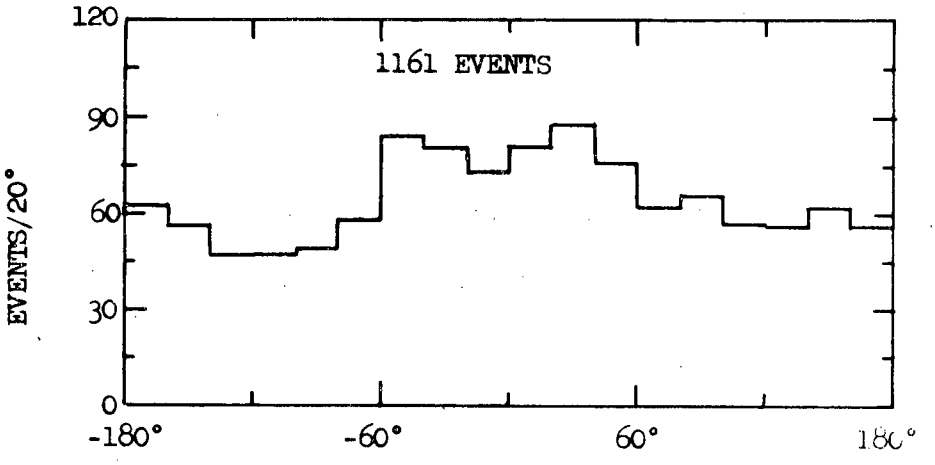

FIGURE III-7. Figure III-7a shows the $K\pi$ Jackson cosine angular distribution in the K*(1420) region. Figure III-7b shows the $K\pi$ Jackson phi angular distribution, the Trieman-Yang angular distribution, in the K*(1420) region. The K*(1420) region is defined by $K\pi$ mass values between 1.32 and 1.55 GeV.

IV. ATTEMPT TO FIT PARTIAL WAVES IN THE $K^+\pi^-$ SYSTEM

A. Theory

The ampliture for reaction IV-1 can be thought of as consisting of two parts.[19]

$$\begin{array}{l} a + b \rightarrow c + d \\ \qquad\quad \hookrightarrow e + f \end{array} \qquad \text{IV-1}$$

The first part, S_{Jm}, describes the production of the final state c + d where c is a particle of spin J with J_z equal m in the Jackson frame. The second part, $A_{\lambda_e\lambda_f}(\theta,\varphi)$, describes the angular distribution of the decay of particle c into particles e and f, where e has helicity λ_e and f has helicity λ_f. The explicit form of $A_{\lambda_e\lambda_f}$ is given in equation IV-2.

$$A_{\lambda_e\lambda_f}(\theta,\varphi) = \sum_m \sqrt{\frac{2J+1}{4\pi}}\, M_{ef,c_J}\, D^{J*}_{m\nu}(\varphi,\theta,-\varphi) \qquad \text{IV-2}$$

$$\nu = \lambda_e - \lambda_f$$

The factor M_{ef,c_J} depends only on the masses of particles c, e and f and on the spin J of particle c.

In general the final state d + e + f could have been produced in four possible ways, three of which would have involved the decay of an intermediate state. However in some special cases it appears as if particles e and f come from the decay of a number of intermediate

states, c_J. In such a case if particles e and f are spinless, the differential cross section is given by equation IV-3.

$$W = F \sum_{\substack{m,m' \\ J,J'}} \sqrt{\frac{2J+1}{4\pi}}\, M_{ef,c_J}\, D^{J*}_{mO}(\varphi,\Theta,-\varphi)\; S_{Jm}$$

$$S^*_{J'm'} D^{J'}_{m'O}(\varphi,\Theta,-\varphi) M^*_{ef,c_{J'}} \sqrt{\frac{2J'+1}{4\pi}} \qquad \text{IV-3}$$

Here F is a flux factor and is equal to $1/(P_a\sqrt{s})$ where P_a is the momentum of particle a in the center of momentum frame of the reaction and $\sqrt{s}$ is the total energy of the system in this frame. The sum over J,J' allows for the intermediate states to have different spins.

If the ampliture S_{Jm} is taken to be a function of the invariants s, t and the mass of the intermediate state c, the differential cross section is seen to be a function of five independent variables. Hence s, t, m_c and the decay angles Θ,φ form a natural set of variables to study reaction IV-1. Moreover from classical physics it is expected that neglecting spin, this parameterization should uniquely describe the reaction, providing the process is rotationally invariant around the beam direction.

The cross section for the reaction is obtained by integrating the differential cross section over phase space. In terms of the four variables, t, m_c cos Θ, φ, the differential for phase space, Φ, is given by equation IV-4.[20]

$$\Phi = \left(\frac{1}{2\pi}\right)^4 \left[\left(\frac{P'_e}{2m_c}\, 2m_c\, dm_c\, d\cos\Theta\, d\varphi\right)\left(2\pi\, \frac{dt}{2P_a P_d}\, \frac{P_d}{2\sqrt{s}}\right)\right] \qquad \text{IV-4}$$

In equation IV-4, P'_e is the momentum of particle e in the rest frame of the intermediate state c, and P_a and P_d are the momenta of particles a and d respectively in the center-of-momentum frame for reaction IV-1.

The differential cross section as a function of the invariant mass of c, $\frac{d\sigma}{dm_c}$, is obtained from W by integrating $W\Phi$ over all t, $\cos\Theta$ and φ. When "cuts" are made, the differential cross section $\frac{d\sigma}{dm_c}$ is obtained by integrating $W\Phi$ only part of the allowed region of t, $\cos\Theta$ and φ.

The moment with respect to $D^L_{\mu 0}$ is obtained by multiplying W by $D^{L*}_{\mu 0}$ and integrating over $\cos\Theta$ and φ. The terms contributing to a moment are more easily seen by making use of relation IV-5.

$$D^J_{mn}(R)\, D^{J'}_{m'n'}(R) = \sum_K C^{JJ'K}_{mn'\mu}\, C^{JJ'K}_{nn'\nu}\, D^K_{\mu\nu}(R) \qquad \text{IV-5}$$

$$\mu = m' + m$$

$$\nu = n' + n$$

The angular dependence of the differential cross section can now be expressed by equation IV-6 which involves a sum of D functions.

$$W = F \sum_{\substack{JJ' \\ mm'}} M_{ef,c_J}\, S_{Jm}\, S^*_{J'm'}\, M_{ef,c_{J'}} \sum_L (-1)^{m'} \sqrt{\frac{2J+1}{4\pi}} \sqrt{\frac{2J'+1}{4\pi}}\, C^{J\ J'\ L}_{m\ -m'\ \mu}\, C^{JJ'L}_{0\,0\,0}\, D^L_{\mu 0}(\varphi,\Theta,-\varphi) \qquad \text{IV-6}$$

$$\mu = m - m'$$

The moment may be readily obtained by remembering the orthogonality relations for the D functions. From equation IV-6, it is seen that a term will contribute to the moment of $D^{L}_{\mu 0}$ only if equation IV-7 holds.

$$\begin{aligned} &J + J' + L = 2N; \qquad N = 1,2,3,\ldots \\ &m - m' = \mu \\ &|J - J'| \leq L \\ &L \leq J + J' \end{aligned} \tag{IV-7}$$

B. Model

The theory of the previous section describes the angular distribution of the decay process. However it says very little about M_{ef,c_J} and even less about the amplitude S_{Jm}. Simple arguments based on potential theory suggest that for spinless particles e and f, M_{ef,c_J} has a threshold dependence given by equation IV-8.[21]

$$M_{ef,c_J} = \left(\frac{P'_e}{2m_c}\right)^{J_c} \tag{IV-8}$$

In this equation P'_e is the momentum of particle e in the rest frame of the intermediate state c which has spin J_c.

The functional dependence of S_{Jm} upon s, t and m_c is unknown in the above theory; hence additional theoretical assumptions are needed. Usually these assumptions are cast in the form of a model such as one particle exchanges, absorptive one particle exchanges or Regge poles. Unfortunately these models do not predict the same functional form.

However they do all have one point in common and that is that they are not capable of explaining why $\frac{d\sigma}{dm_c}$ becomes large for certain values of m_c. The usual procedure for explaining this is to say that the amplitude of the model is multiplied by a function of m_c which exhibits the proper behavior in the region of the peak. This function is universally taken to be a Breit-Wigner which has two parameters, one controlling the central value of the peak and the other the width. The functional form of the Breit-Wigner is also attractive from the point of view of field theory which suggests this functional form for a metastable intermediate state.

For this discussion the important point about the use of Breit-Wigners in model dependent calculations is that it says M_{ef,c_J} behaves like a Breit-Wigner in the region of an enhancement.

To study the dynamics of elementary particle reactions and to differentiate between the various models, it is necessary to extract the s and t dependence of the amplitudes S_{Jm}. From arguments based upon potential scattering it is assumed that the enhancements in $\frac{d\sigma}{dm_c}$ are due to resonances in single partial waves, and that two partial waves do not resonate in the same mass region. Moreover it is assumed that the non resonant partial waves are small and that their mass dependence is weak. Under these assumptions it is possible to either ignore the background or to subtract it. In either case the differential cross section, equation IV-6, reduces to a form involving a single J-value, equation IV-9.

$$W_J = F \sum_{mm'} M_{ef,c_J} S_{Jm} S^*_{Jm'} M^*_{ef,c_J}$$

$$\sum_L (-1)^{m'} \frac{2J+1}{4\pi} C^{JJL}_{m-m'\mu} C^{JJL}_{000} D^L_{\mu 0} (\varphi,\theta,-\varphi) \qquad \text{IV-9}$$

$$\mu = m - m'$$

By taking appropriate linear combinations of D functions, it is possible to project out the value of $M_{ef,c_J} S_{Jm} S^*_{Jm'} M^*_{ef,c_J}$. In this manner it is possible to study the s and t dependence of $S_{Jm} S^*_{Jm'}$.

In order to simplify the notation, it is helpful to make the definitions of equations IV-10 and IV-11.

$$B_J = M_{ef,c_J} \qquad \text{IV-10}$$

$$R^{JJ'}_{mm'} = S_{Jm} S^*_{Jm'} \qquad \text{IV-11}$$

With these definitions equation IV-9 reduces to equation IV-12.

$$W_J = F \sum_{mm'} R^{JJ}_{mm'} B_J B^*_J \sum_L (-1)^{m'} \frac{2J+1}{4\pi} C^{J\,J\,L}_{m-m'\mu} C^{JJL}_{000} D^L_{\mu 0} (\varphi,\theta,-\varphi) \qquad \text{IV-12}$$

From equation IV-12 it is apparent that $R^{JJ}_{mm'}$ is a density matrix element; the superscripts merely indicate the spin of the resonance. In the more general case where several spin states are present, the differential cross section is given by equation IV-13.[19]

$$W = F \sum_{\substack{JJ' \\ mm'}} R^{JJ'}_{mm'} B_J B^*_{J'} \sum_L (-1)^{m'} \sqrt{\frac{2J+1}{4\pi}} \sqrt{\frac{2J'+1}{4\pi}}$$

$$C^{J\,J'\,L}_{m-m'\,\mu} C^{JJ'L}_{00\,0} D^L_{\mu 0}(\varphi,\Theta,-\varphi) \qquad \text{IV-13}$$

$$\mu = m - m'$$

Here $R^{JJ'}_{mm'}$ is seen to be a generalized density matrix describing the interference of a spin state $[J,m\rangle$ with a spin state $[J',m'\rangle$.

The existence of asymetries in the angular distributions in the resonance region indicates that the background partial waves interfere with the resonant partial waves. A study of these asymetries indicates that they have a weak mass dependence; however that mass dependence is strong enough to make background subtraction techniques questionable. Moreover the existence of nonignorable or nonsubtractable background alters the experimental procedure for extracting $R^{JJ'}_{mm'}$. For example, the existence of an S-wave background in the region of a P-wave resonance means that only $R^{11}_{00} - R^{11}_{11}$ can be determined; whereas without the S-wave background R^{11}_{00} and R^{11}_{11} could be determined separately.

In addition Veneziano models which give the complete differential cross section for two particles going into three particles suggest that when there is one resonance in the Jth partial wave, there will also be resonances in the same mass region for some or all of the lower partial waves.

An examination of the differential cross section as expressed by equation IV-13 reveals that each moment has contributions from only a

few of the generalized density matrix elements $R^{JJ'}_{mm'}$. For example if there is a P-wave resonance and an S-wave background, the moment for D^0_{00} involves a sum of R^{00}_{00}, R^{11}_{00} and R^{11}_{11} while the moment with respect to D^2_{00} involves a sum of R^{11}_{00} and R^{11}_{11}. Moreover these three generalized density matrix elements only appear in those two moments. Since the $R^{JJ'}_{mm'}$ enter into the moments in a linear manner, it is possible to make a least-squares fit for the $R^{JJ'}_{mm'}$, providing the experimental mass dependence of the moment is known and a mass dependent parameterization of B_J has been hypothesized. This type of fit is especially simple since it involves only matrix algebra. In the above example a 3 by 3 matrix inversion and a matrix multiplication determine R^{00}_{00}, R^{11}_{00}, and R^{11}_{11}.

The experimental mass dependence is very easy to obtain from data. The mass dependent parameterization of the dominant resonant partial wave is given by a Breit-Wigner. There is little theoretical guidance for the mass behavior of the background waves; however their threshold behavior is indicated by equation IV-8. Assuming that the background partial waves are small and have a weak mass dependence when compared to the resonant partial waves suggests that the exact functional form of the mass dependence of the background partial waves is relatively unimportant. Moreover since B_J enters into many different moments which are uncorrelated in the limit of infinite statistics, some discrimination should be possible in selecting a parameterization for the background partial waves, B_J, when all the moments are fit simultaneously.

In summary, the following assumptions are used in attempting to fit partial waves in the $K^+\pi^-$ system for the final state $K^+\pi^-P$:

1. Experimentally no structure is seen in the $p\pi^-$ or pK^+ system while structure is seen in the $K^+\pi^-$ system. Hence $\frac{d\sigma}{dm_{K\pi}}$ is assumed to be given by equation IV-13.

2. It is assumed that the isospin 3/2 contribution to $\frac{d\sigma}{dm_{K\pi}}$ is negligible in comparison to the isospin 1/2 part. This assumption is based upon the fact that no structure has been seen in $K^+\pi^+$ or $K^-\pi^-$ systems. Moreover the 3/2 isospin state is exotic.

3. In the region of the K*(890) the P-wave is assumed to be given by a Breit-Wigner; in the region of the K*(1420), the D-wave is assumed to be given by a Breit-Wigner. The background partial waves are assumed to be small and to have a weak mass dependence when compared with the mass dependence of the resonance.

4. The generalized density matrix elements $R^{JJ'}_{mm'}$ may be obtained by making a least-squares fit to the moments which are experimentally known.

5. Since the background partial waves appear in many moments, there is some discrimination in selecting a parameterization for them.

The model may be criticized on the following two grounds:

1. In the limit of infinite statistics, the moments are independent; experimentally, however, the moments are somewhat correlated.

2. Since the density matrix elements are composed of bilinear terms in the amplitudes, there are certain constraint equations which must be satisfied by a physical solution for the density matrix. Equations IV-14 and IV-15 are examples of such equations.

$$R^{11}_{10}{}^2 \leq R^{11}_{00} R^{11}_{11} \qquad \text{IV-14}$$

$$R^{11}_{mm} \geq 0 \qquad \text{IV-15}$$

The least-squares fitting procedure does not guarantee that the generalized density matrix elements satisfy these equations of constraint. However if the correct parameterizations of the partial waves were used, the generalized density matrix elements would satisfy the equations of constraint.

The model has the following virtues:

1. The fitting is very fast because it involves a linear chi squared fit.

2. The results of the fit for each set of correlated moments may be displayed at once so that it is possible to visually check the quality of the fit for a given set of functional dependences for B_J.

3. A second fitting program may be used to adjust parameters associated with B_J. This allows the selection of a best set of parameters for a given functional dependence for B_J. Again this is a very fast fitting procedure.

C. Three Fits For the Moments in the $K\pi$ System

A number of parameterizations for the factors B_J in equation IV-13 were tried. Of these parameterizations three of the most interesting and successful are described in detail below.

1. First Parameterization

In the first of these, the mass dependence of each partial wave was parameterized by equation IV-16.

$$B_J = (1 - \alpha_J)\, BW_J + \alpha_J\, BG_J\, e^{i\varphi_J}$$

$$BG_J = \left(\frac{2P}{m_c}\right)^J$$

$$BW_J = \frac{2P_o}{m_o}\,\frac{m_c}{2P}\left(\frac{P_o}{P}\right)^{2J+1} \sin\delta\, e^{i\delta} \qquad \text{IV-16}$$

$$\tan\delta = \frac{m_o\,\Gamma}{m_o^2 - m^2}\left(\frac{P}{P_o}\right)^{2J+1}$$

$$0 \le \alpha_J \le 1$$

$$0 \le \varphi_J \le 2\pi$$

In this equation α_J and φ_J are constants, m_c is the mass of the $K\pi$ system, P is the momentum of the π in the rest frame of the $K\pi$ system, m_o is the mass of the resonance and P_o is the momentum at the resonant mass. This parameterization for the Breit-Wigner has been chosen so that it agrees with the formalization given by Jackson[22] and so that BW will equal 1 at the resonant mass. The term BG in equation IV-16 has been added to account for any non resonant contributions to the partial wave. The functional behavior of BG has been chosen so that the term has the proper threshold behavior for the decay of a particle out of a potential well and so that BG will be 1 at infinite $K\pi$ masses.

In order to obtain the mass dependence of the moments the differential cross section needs to be multiplied by phase space. Rather than using a peripheralized phase space, a polynomial in $m_{K\pi}$ was used

for Φ. This polynomial was obtained by making a chi square fit to the mass plot using equation IV-17.

$$Y = \left(\sum_{J=0}^{3} \alpha_J \left| BW_J \right|^2 + 1 + \sum_{J=1}^{3} \beta_J \left| BG_J \right|^2 \right) P_n(m-m_c) \qquad \text{IV-17}$$

In this equation P_n is an nth order polynomial in mass expanded about m_c. The constants α_J, β_J and the coefficients of the polynomial were adjusted so as to obtain a minimum chi square. The polynomial was expanded about m_c where m_c is any mass inside the allowed mass region for the $K\pi$ system; this type of an expansion tends to minimize correlations among the coefficients of the polynomial. It was found that β was very small for all J-values and could in general be ignored. The order of the polynomial was chosen so as to give a good chi square and yet not be so high that there was structure in the region of the resonances. In general the appearance of the polynomial agreed well with what would be expected for a peripheralized phase space. Table IV-1 lists the central values and widths of the resonances used in equation IV-17. The shape of the polynomial appears to be independent of whether one or two resonances are in the region of the K*(1420). Figure IV-1a shows the fit to the mass plot and Figure IV-1b shows the shape of phase space. The F-wave resonance was included because prior fits indicated that F-wave is needed in the fitting of the odd L-valued moments. The values of the F-wave resonance are taken as those determined by Cords et al.[23]

IV-1a

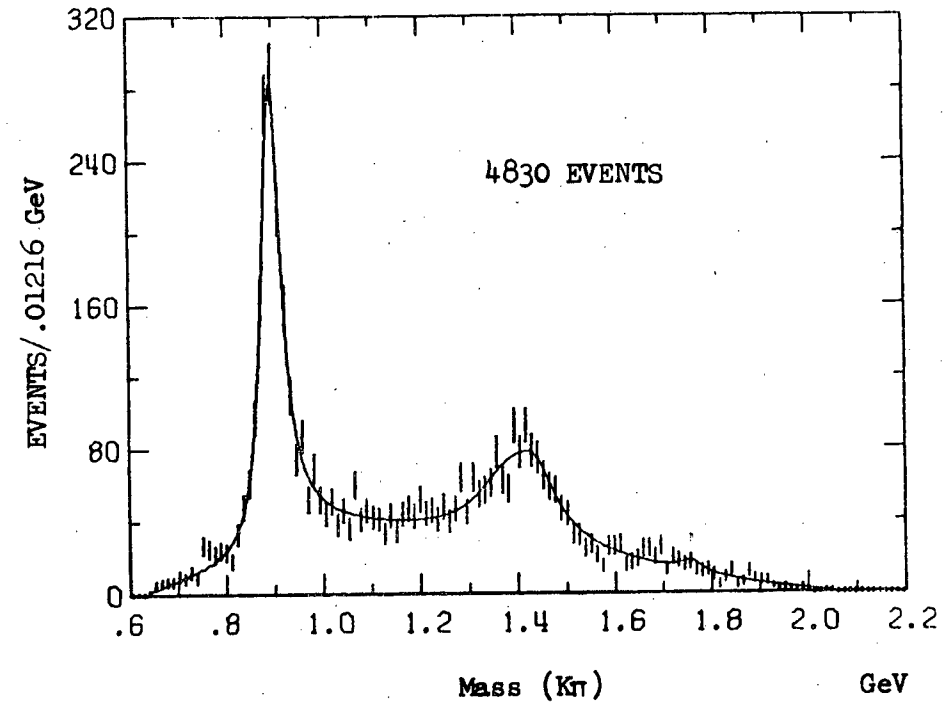

IV-1b

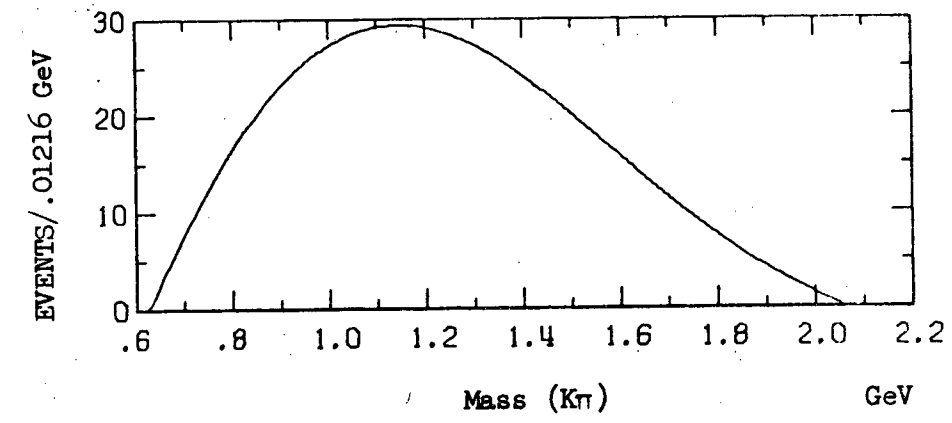

FIGURE IV-1. Figure IV-1a shows the fit to the mass plot using a polynomial for the mass dependence of phase space. Figure IV-1b shows the mass dependence of the polynomial.

Wave	Mass (GeV)	Width (GeV)
S	1.385	.150
P	.896	.05
D	1.448	.115
F	1.760	.06

TABLE IV-1. Table IV-1 shows the central values and widths of the resonances used in fitting the mass plot in Figure IV-1. This fit was used to determine the coefficients in a polynomial expansion for phase space.

A survey of the moments for m values greater than 1 fails to show either structure or significant nonzero behavior. Consequently only the moments for m less than 2 and L less than 7 were fit. In addition in an attempt to reduce the number of parameters all generalized density matrix elements with m values larger than 1 were set to zero. This is probably a fairly good assumption for exchange diagrams do not directly populate these density matrix elements if there is no absorption. Moreover adequate fits are obtained without using these density matrix elements.

In fitting the moments, the 4 α_J, 4 φ_J and the width and mass of the S, P and D-resonances were varied. Figures IV-2a-m show the moments and the resultant fit. Table IV-2 shows the fit values for α, φ and the masses and widths of the S, P and D-resonances. Table IV-3 shows the raw numbers obtained for the generalized density matrix elements and their error. Note that for interference moments where J and J'

FIGURE IV-2. Figure IV-2 shows the mass dependence of the moments with respect to Y_{Lm} in the Jackson frame for the $K\pi$ system. The curves are the result of a fit with a Breit-Wigner and a background term in the S, P, D and F-Partial waves, and with a polynomial for peripheralized phase space.

IV-2a

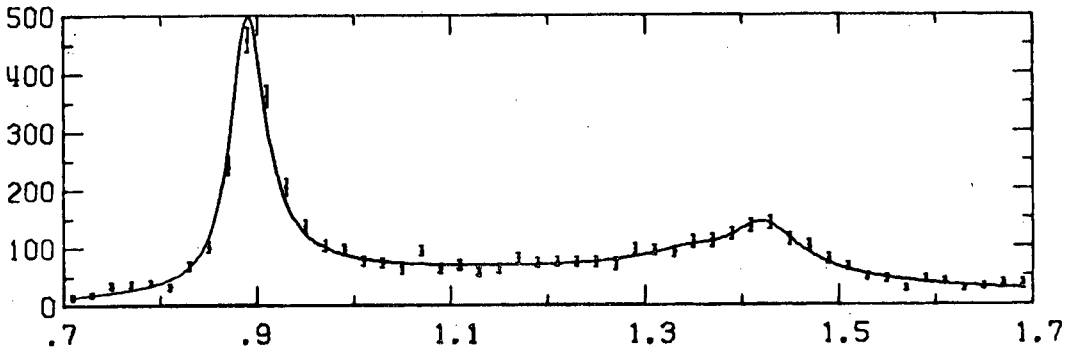

IV-2b

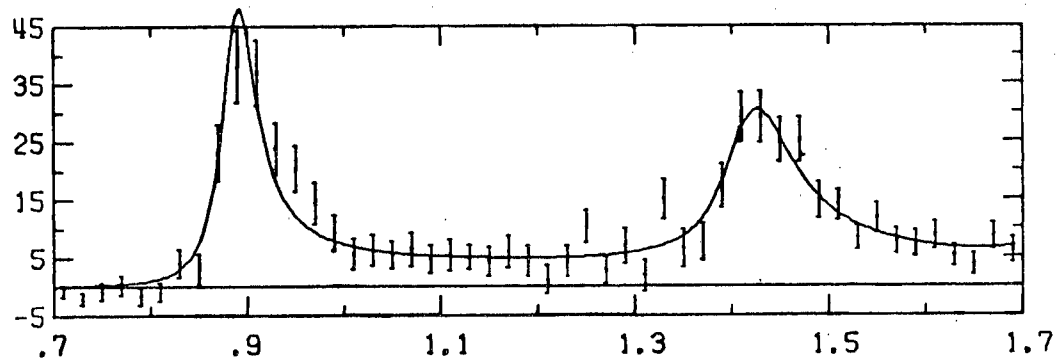

IV-2c

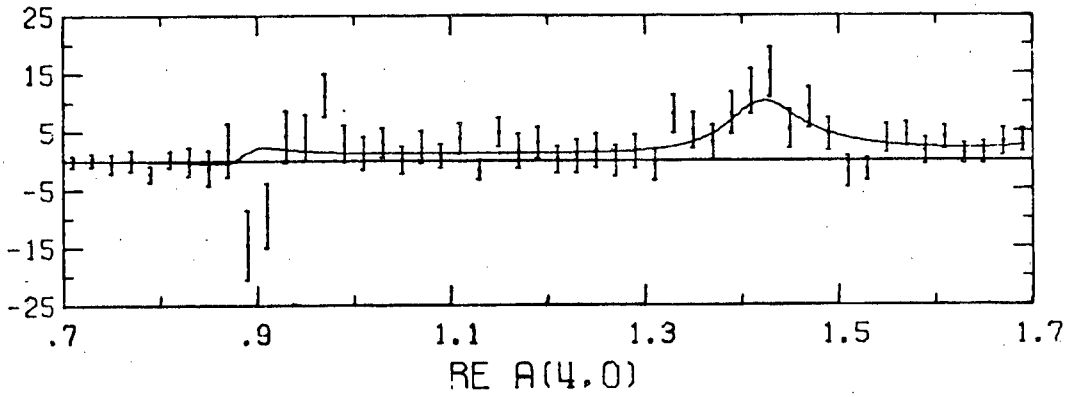

IV-2d

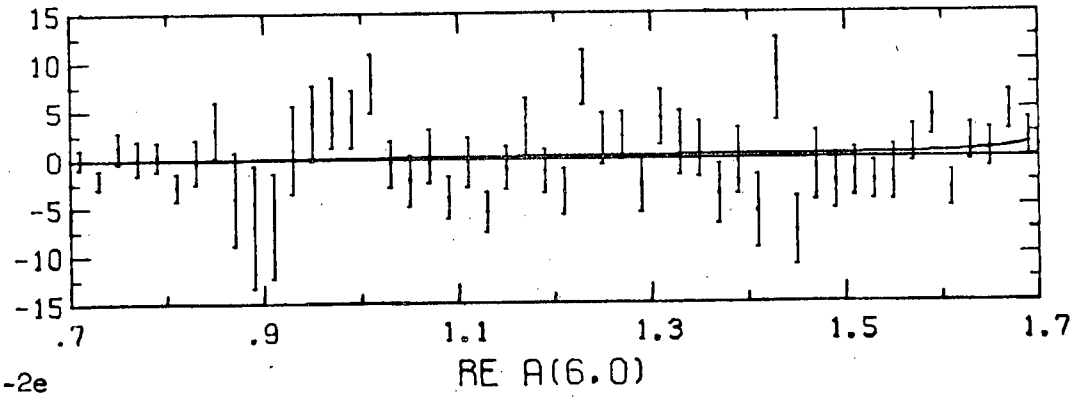

IV-2e

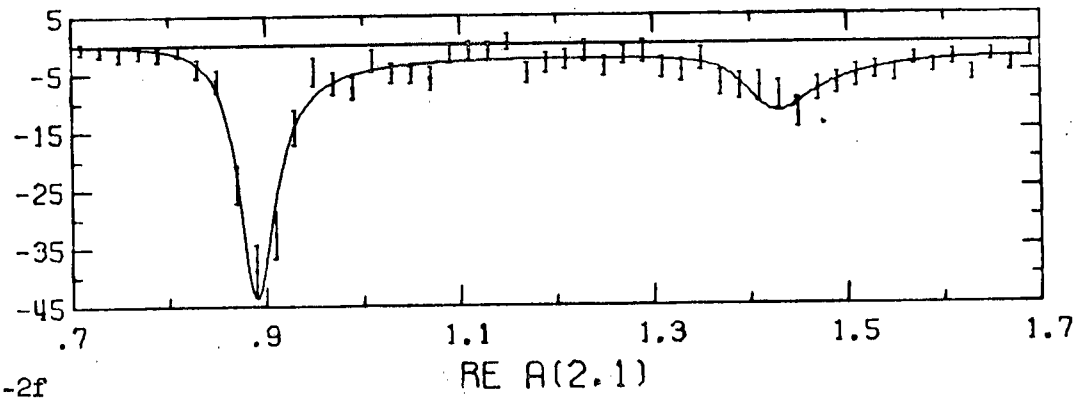

IV-2f

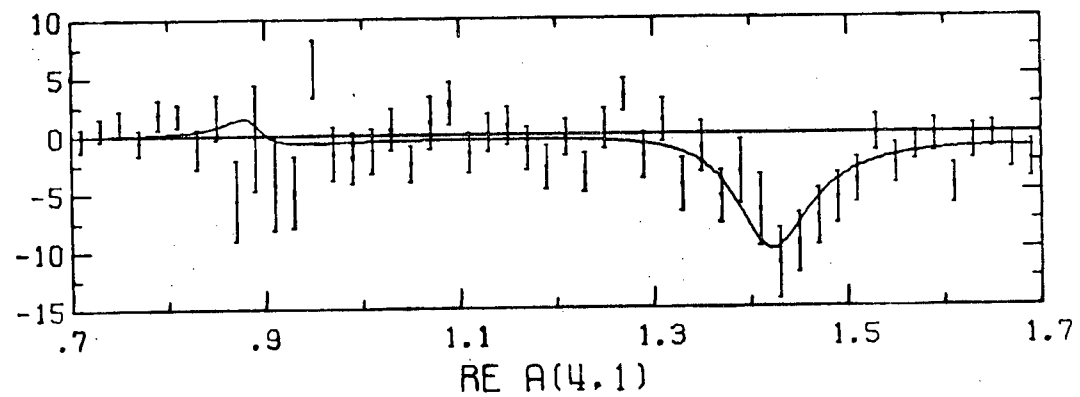

IV-2g

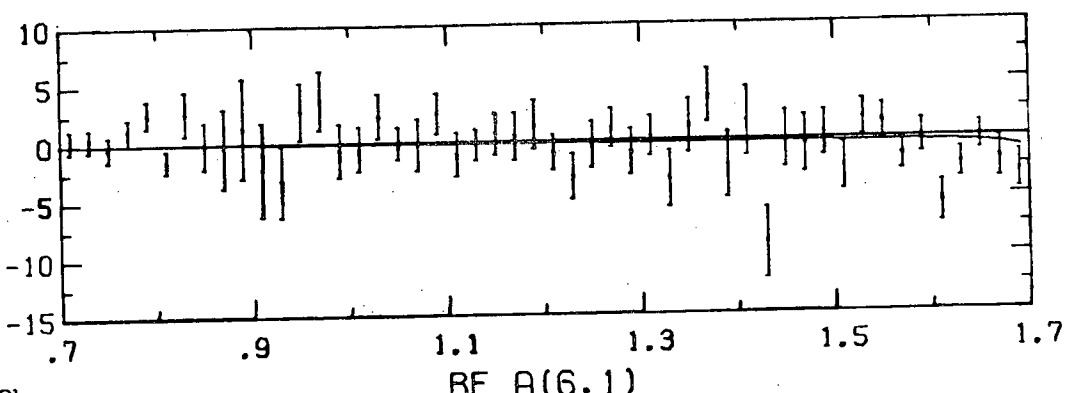

IV-2h

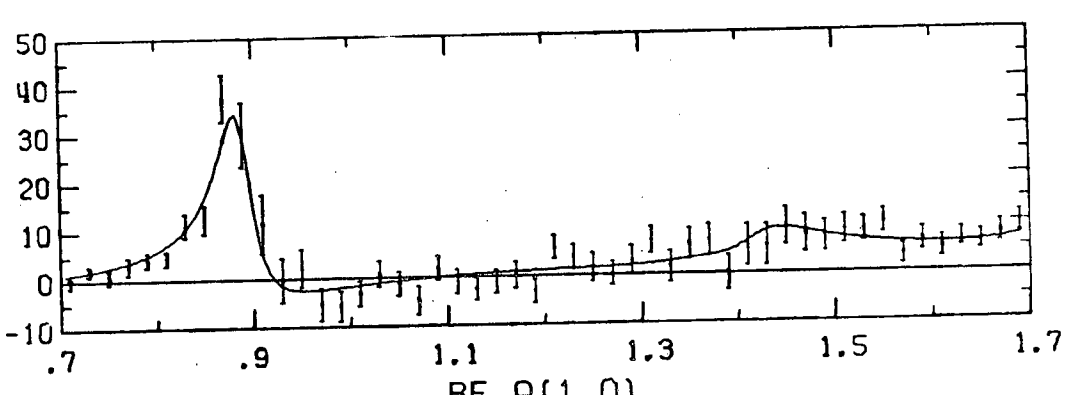

IV-2i

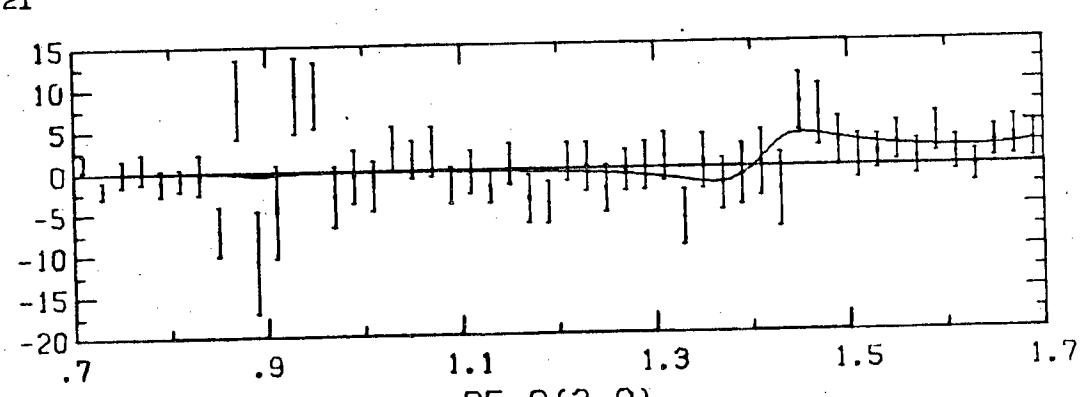

IV-2j

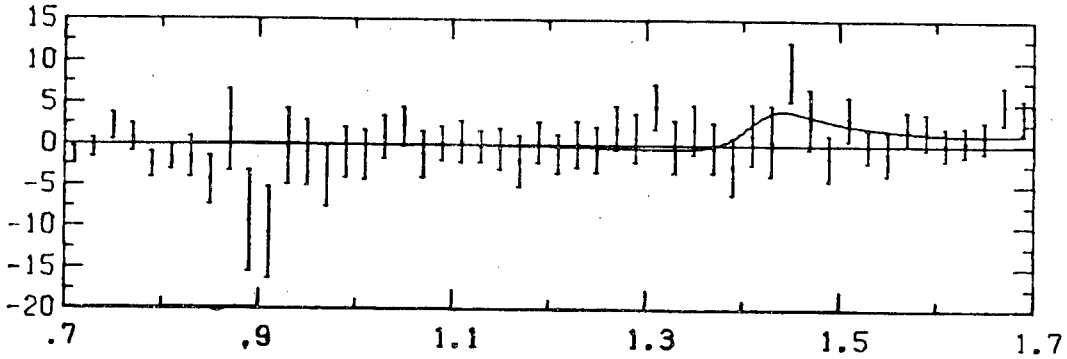

IV-2k

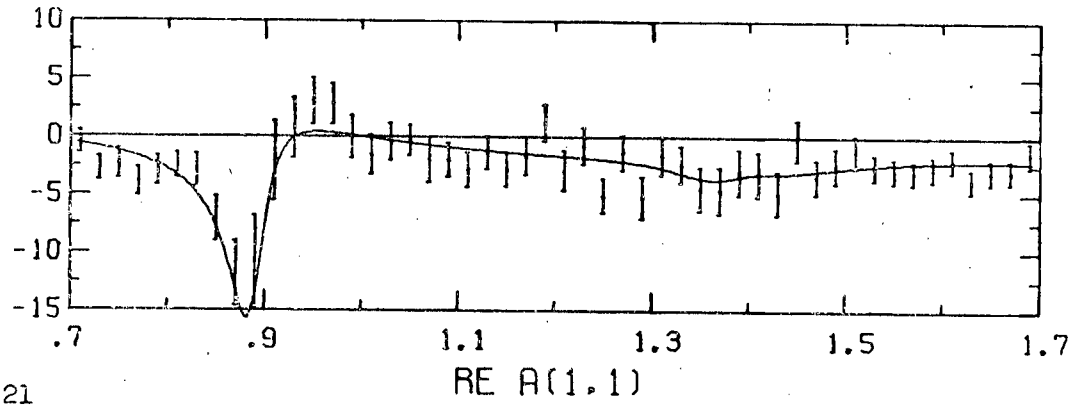

IV-2l

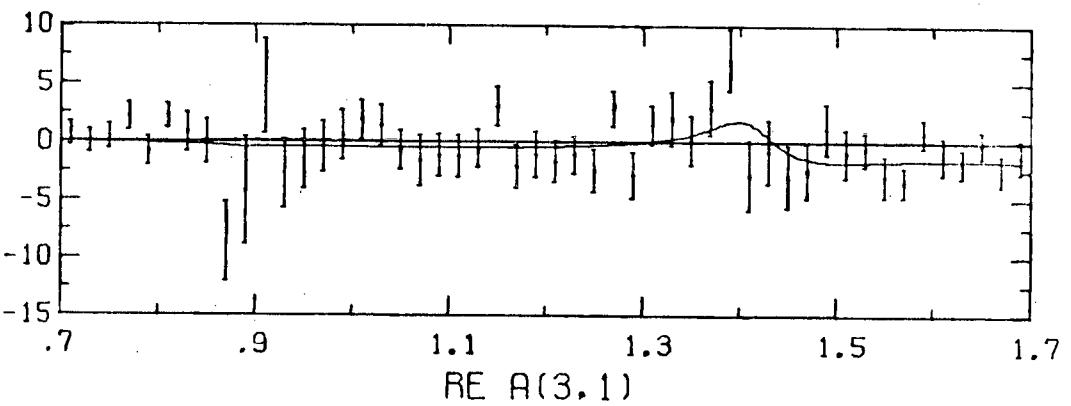

IV-2m

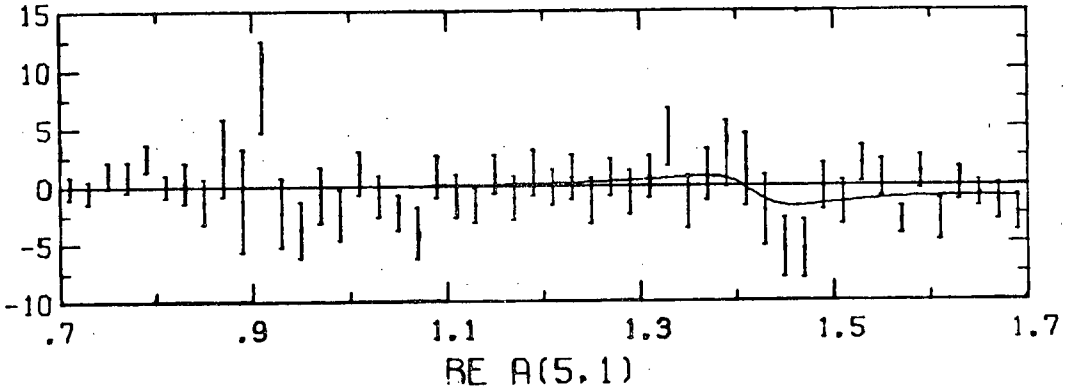

are not equal there is a real part, $R^{JJ'}_{mm'}$, and an imaginary part, $I^{JJ'}_{mm'}$, which contribute to the real part of the moment (see equation IV-13).

wave	S	P	D	F
α	.66 ± .04	.13 ± .02	.06 ± .03	.21 ± .05
φ (rad)	.59 ± .26	1.37 ± .13	3.1 ± .9	.9 ± .4
m_o (GeV)	1.37 ± .01	.8959 ± .0009	1.431 ± .003	---
Γ (GeV)	.11 ± .03	.046 ± .002	.097 ± .008	---

TABLE IV-2. Table IV-2 shows the fit values for α_J, φ_J, m_{oJ} and Γ_J.

Figure IV-3 shows the contribution of each of the partial waves to the mass plot; the contribution is proportional to $B_J B_J^*$. From the figure it is possible to estimate the number of events in the background under the K*(890) and K*(1420). Table IV-4 shows the results of these estimates.

2. Second Parameterization

Although the first parameterization fits the moments well, it can be criticized because the mass dependence of phase space was obtained by fitting the mass plot with a polynomial. The second parameterization overcomes this criticism by using a peripheralized phase space given by equation IV-18.[24]

$$\varphi = \frac{1}{(4\pi)^3 P_a \sqrt{s}} \frac{(m_d - m_b)^2 - t}{(\mu^2 - t)^2} P'_e m_c^2 \, dm_c \, d\cos\theta \, d\varphi \, dt \qquad \text{IV-18}$$

Density matrix elements contributing to the moments Y_{00} (mass plot), Y_{20}, Y_{40} and Y_{60}.

R(JJ';mm')		I(JJ';mm')	
R(00;00)	3.1 ± 0.1		
R(11;00)	12.8 ± 0.6		
R(11;11)	4.6 ± 0.4		
R(22;00)	3.1 ± 0.3		
R(22;11)	0.9 ± 0.2		
R(33;00)	2.3 ± 0.4		
R(33;11)	- .4 ± 0.2		
R(20;00)	0.7 ± 0.2	I(20;00)	1.4 ± 0.3
R(31;00)	0.0 ± 2.3	I(31;00)	-8.0 ± 1.4
R(31;11)	0.1 ± 1.5	I(31;11)	-2.8 ± 1.0

Density matrix elements contributing to the moments Y_{21}, Y_{41}, and Y_{61}.

R(11;10)	-2.3 ± 0.2		
R(22;10)	-0.5 ± 0.1		
R(33;10)	-0.5 ± 0.1		
R(20;10)	-0.2 ± 0.1	I(20;10)	-0.4 ± 0.1
R(31;10)	0.6 ± 0.7	I(31;10)	1.6 ± 0.5
R(31;0-1)	1.3 ± 0.9	I(31;0-1)	0.7 ± 0.7

Density matrix elements contributing to the moments Y_{10}, Y_{30}, and Y_{50}.

R(10;00)	4.9 ± 0.4	I(10;00)	0.7 ± 0.3
R(21;00)	-0.2 ± 5.9	I(21;00)	-8.4 ± 6.8
R(21;11)	-0.2 ± 1.6	I(21;11)	-2.8 ± 2.0
R(32;00)	-4.3 ± 4.3	I(32;00)	-5.9 ± 1.4
R(32;11)	-3.3 ± 3.0	I(32;11)	-2.2 ± 1.0
R(30;00)	-0.6 ± 0.7	I(30;00)	1.0 ± 2.0

Density matrix elements contributing to the moments Y_{11}, Y_{31}, and Y_{51}.

R(10;10)	-1.0 ± 0.1	I(10;10)	-0.2 ± 0.1
R(21;0-1)	-0.5 ± 0.9	I(21;0-1)	0.3 ± 1.0
R(21;10)	-0.2 ± 1.0	I(21;10	-0.8 ± 1.2
R(32;10)	0.0 ± 1.0	I(32;10)	0.1 ± 0.5
R(32;0-1)	-0.3 ± 1.0	I(32;0-1)	-0.7 ± 0.5
R(30;10)	-0.3 ± 0.1	I(30;10)	0.1 ± 0.3

TABLE IV-3. Table IV-3 shows generalized density matrix elements and their errors from the fit.

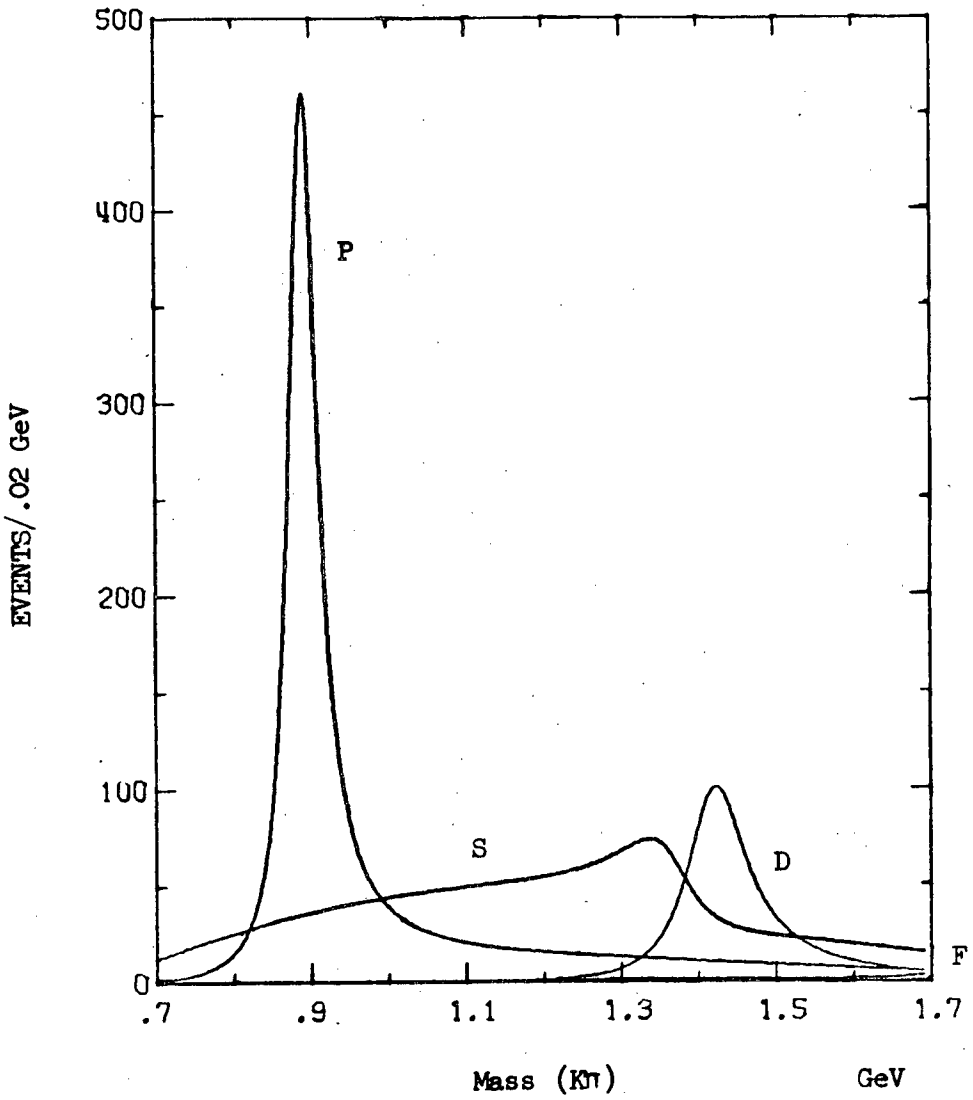

FIGURE IV-3. Figure IV-3 shows the contribution of each of the partial waves to the mass plot for the fit with a Breit-Wigner and a background term in the S, P, D and F-waves, and a polynomial for peripheralized phase space.

K*(890) region (.84-.94 GeV) has 1374.2 events in the fit.

partial wave	events	percent of total events in the fit
S	174.5 ± 6.6	(12.7 ± 0.5)%
P	1199.0 ± 48.9	(87.3 ± 3.6)%
D	0.0 ± 0.0	(0.0 ± 0.0)%
F	0.6 ± 0.2	(0.0 ± 0.0)%

K*(1420) region (1.34-1.54 GeV) has 1018.2 events in the fit.

S	377.2 ± 14.2	(37.0 ± 1.4)%
P	97.0 ± 4.0	(9.5 ± 0.4)%
D	534.8 ± 42.2	(52.5 ± 4.1)%
F	9.2 ± 2.3	(0.9 ± 0.2)%

TABLE IV-4. Table IV-4 gives the number of events and percentage of the total events in the K*(890) and K*(1420) regions according to the fit using Breit-Wigner functions and a background term in each partial wave. Because of rounding, the sum of the percentages may not add to 100%.

Here μ is the pion mass. The form of peripheralized phase space was obtained from a pole approximation for pion exchange involving two nucleons at one vertex.

In extrapolations to the pion pole, the differential cross section $\frac{d^2\sigma}{dm_c dt}$ is obtained by integrating equation IV-18 over all cosθ and φ, and multiplying by $g^2\sigma_1(m_c)F(m_c,t)$ where g is a coupling constant, σ_1 is the cross section for physical $K\pi$ scattering and $F(m_c,t)$ is a product of form factors.[25] The cross section σ_1 is given by equation IV-19.

$$\sigma_1 = \frac{4\pi}{(P'_e)^2}\left(|S|^2 + 3\,|P|^2 + 5\,|D|^2 + \ldots \right) \qquad \text{IV-19}$$

The threshold behavior of S, P and D in equation IV-19 is given by equation IV-20.

$$\begin{aligned} S &\sim P'_e \\ P &\sim (P'_e)^2 \\ D &\sim (P'_e)^3 \end{aligned} \qquad \text{IV-20}$$

The pole extrapolation technique suggests that the factors B_J in equation IV-13 should be parameterized according to equation IV-21.

$$\begin{aligned} B_J &= (1-\alpha_J)\,BW_J + \alpha_J BG_J\, e^{i\theta_J} \\ BW_J &= \frac{1}{2P}\left(\frac{P_o}{P}\right)^J \sin\delta_J\, e^{i\delta_J} \\ \tan\delta_J &= \frac{m_o}{m_o^2 - m_c^2}\left(\frac{P}{P_o}\right)^{2J+1} \end{aligned} \qquad \text{IV-21}$$

$$BG_J = \frac{1}{2P}\left(\frac{2P}{m_c}\right)^{J+1}$$

$$0 \leq \alpha_J \leq 1 \qquad \text{IV-21 con't}$$

$$0 \leq \varphi_J \leq 2\pi$$

In this equation α_J and φ_J are constants, m_c is the mass of the Kπ system, P is the momentum of the final K in the rest frame of the Kπ system, m_o is the mass of the resonance, and P_o is the momentum at the resonant mass. This parameterization for the Breit-Wigner has been chosen so that it agrees with the formalism given by Jackson[22] and so that BW will equal 1/(2P) at the resonant mass. The term BG in equation IV-21 has been added to account for any non resonant contributions to the partial wave. The functional behavior of BG has been chosen so that the term has the proper threshold behavior for the decay of a particle out of a potential well and so that BG will equal 1/(2P) at infinite Kπ masses.

The mass dependence of the moments was obtained by integrating phase space, equation IV-18, from t_{min} to t_{max}, multiplying the result by equation IV-13 and using the orthogonality relations for the D-functions. This procedure may be easily modified to take into account the effects of "cuts" on either t or t' by integrating over the allowed region of t or t'.

In the fitting, only moments for m less than 2 and L less than 7 were fit. In addition all generalized density matrix elements with m values larger than 1 were set to zero. The 4 α_J, 4 φ_J and the width and mass of the S, P, and D-resonances were varied in order to obtain a best fit in a chi squared sense. Figures 4a-m show the moments and the

FIGURE IV-4. Figure IV-4 shows the mass dependence of the moments with respect to Y_{Lm} in the Jackson frame for the $K\pi$ system. The curves are the result of a fit with a Breit-Wigner and a background term in the S, P, D and F-partial waves, and with a peripheralized phase space given by a pole approximation.

IV-4a

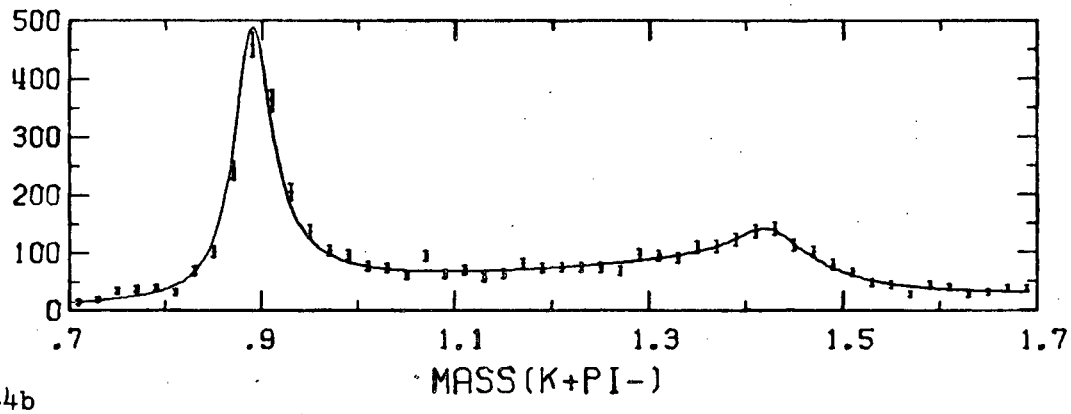

IV-4b

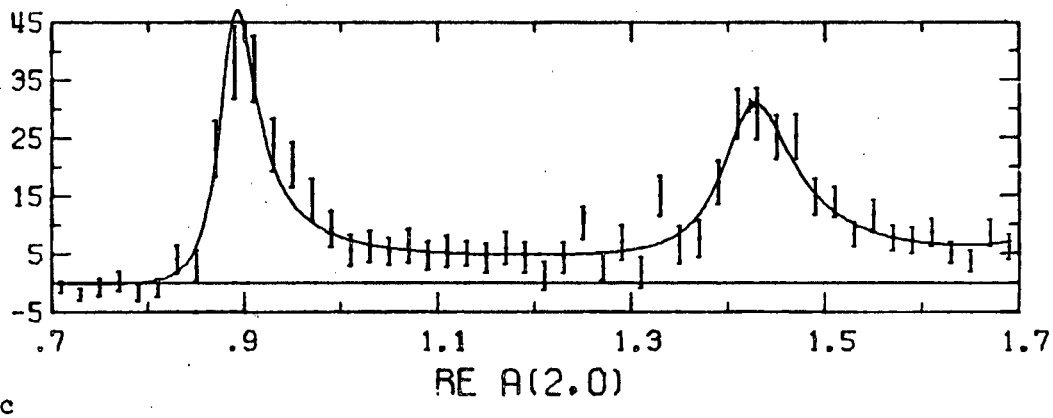

IV-4c

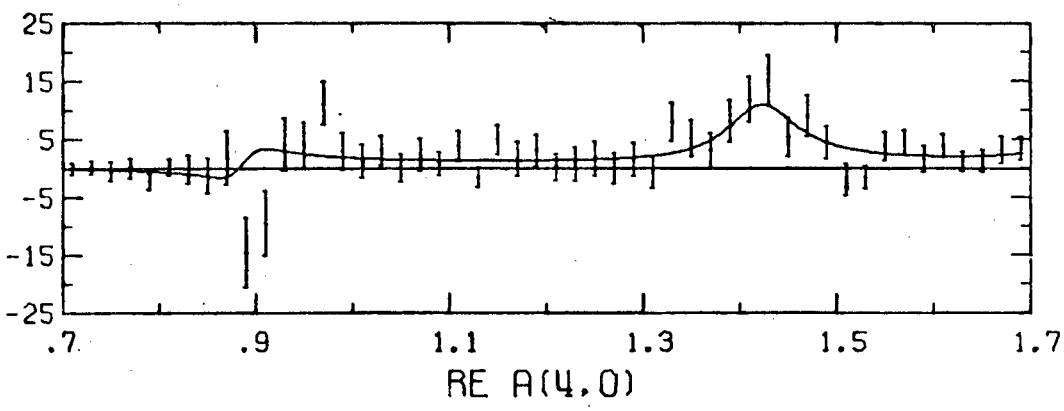

IV-4d

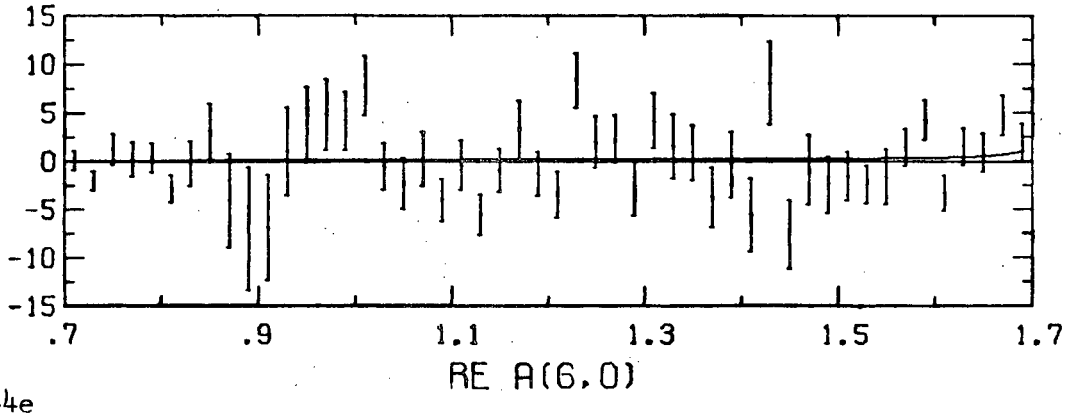

IV-4e

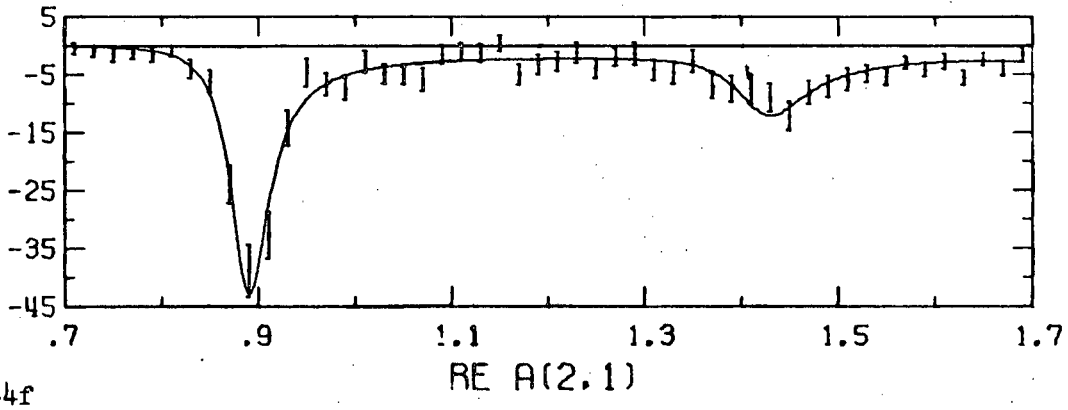

IV-4f

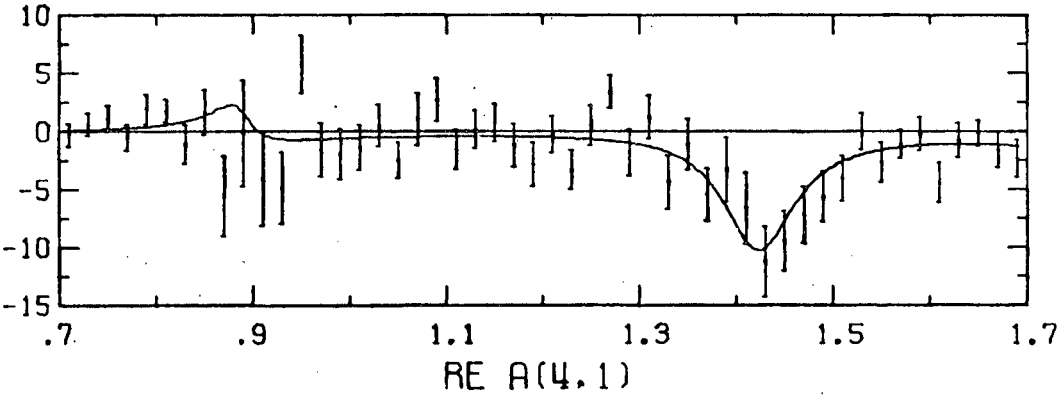

IV-4g

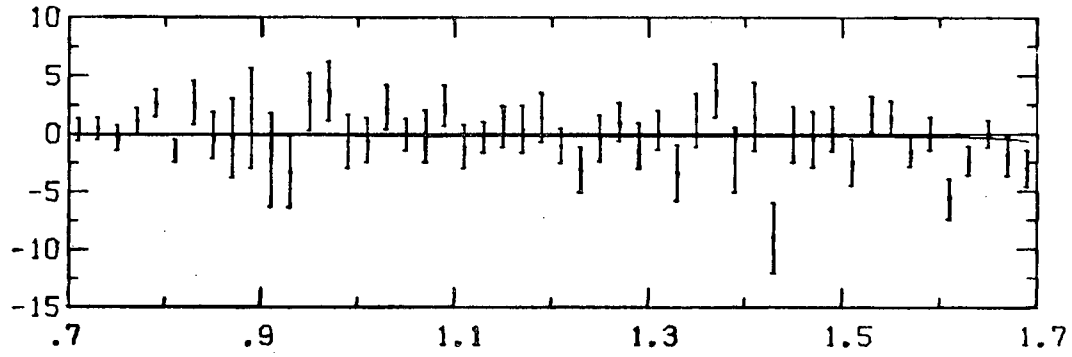

IV-4h

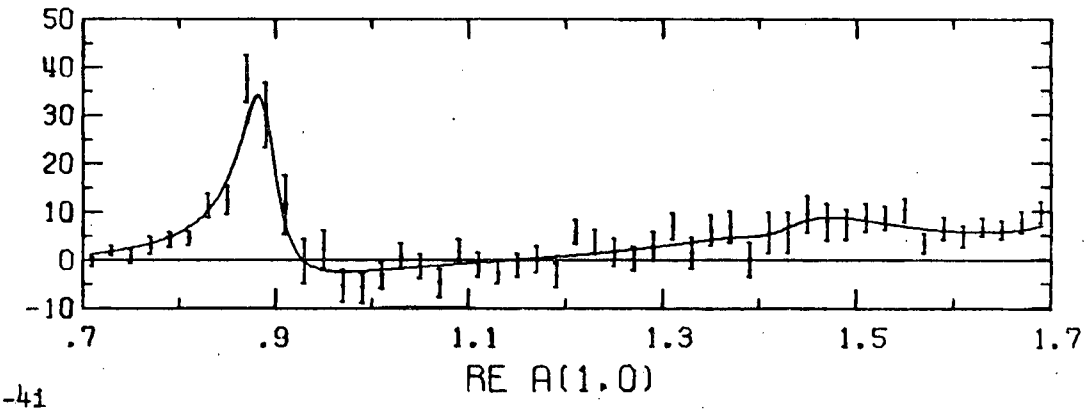

IV-4i

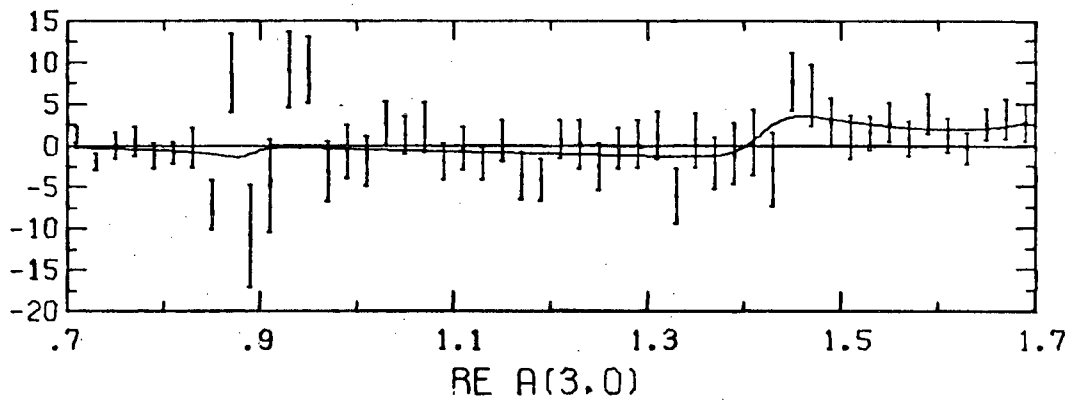

IV-4j

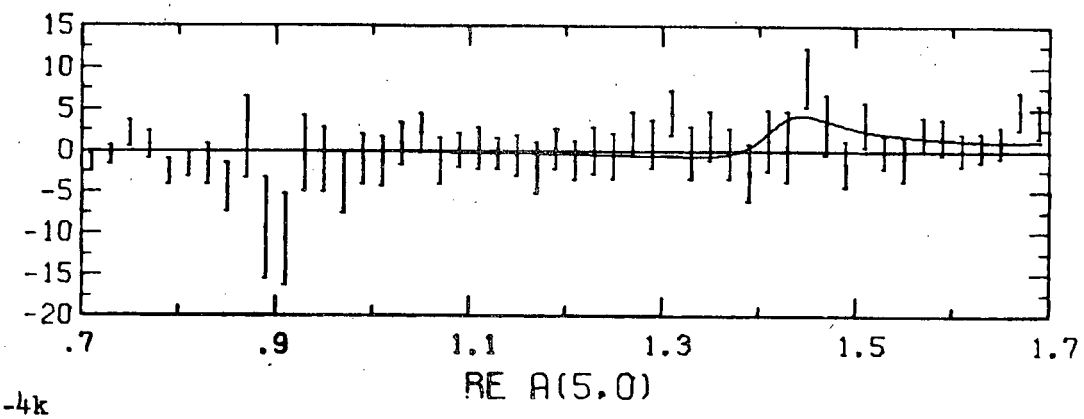

IV-4k

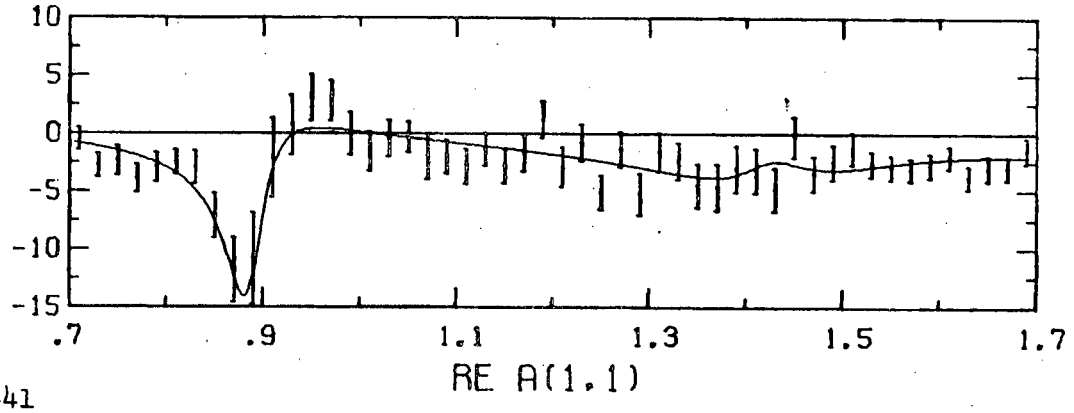

IV-4l

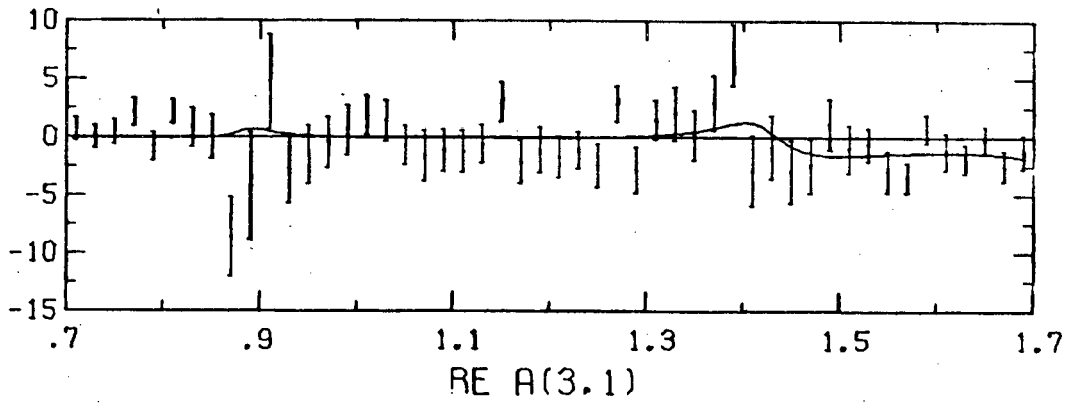

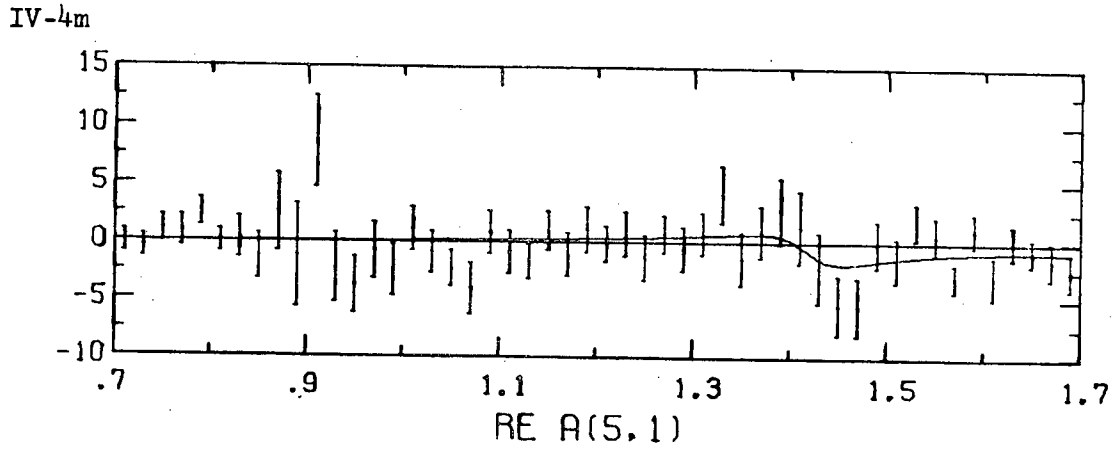
IV-4m
15
10
5
0
-5
-10
.7
.9
1.1
1.3
1.5
1.7
RE A(5,1)

resultant fit. Table IV-5 gives the fit values for α_J, φ_J and the masses and widths of the S, P and D-resonances. The mass and width of the F-resonance was held fixed at the values given in Table IV-1. Table IV-6 shows the raw numbers obtained for the generalized density matrix elements and their error.

wave	S	P	D	F
α	.64 ± .03	.16 ± .02	.10 ± .04	.21 ± .05
φ (rad)	.00 ± .08	1.10 ± .11	.23 ± .50	1.36 ± .30
m_o (GeV)	1.45 ± .02	.8962 ± .0008	1.435 ± .003	---
Γ (GeV)	.25 ± .05	.049 ± .002	.093 ± .009	---

TABLE IV-5. Table IV-5 shows the fit values for α_J, φ_J, m_{oJ} and Γ_J.

Figure IV-5 shows the contribution of each of the partial waves to the mass plot. This fit has an unphysical value of R(33;11) which causes the F-wave to have a negative contribution to the mass plot. However the total effect of the F-wave is less than 0.3% of the mass plot and its primary contribution lies at high $K\pi$ masses where phase space is falling. The problem of unphysical generalized density matrix elements will be discussed further in the last section of this chapter.

From Figure IV-5, it is possible to estimate the number of events in the background under the K*(890) and K*(1420). Table IV-7 shows the results of these estimates.

Density matrix elements contributing to the moments Y_{00} (mass plot), Y_{20}, Y_{40} and Y_{60}.

R(JJ';mm')		I(JJ';mm')	
R(00;00)	10.7 ± 0.4		
R(11;00)	25.9 ± 1.3		
R(11;11)	9.2 ± 0.7		
R(22;00)	5.0 ± 0.6		
R(22;11)	0.7 ± 0.3		
R(33;00)	1.6 ± 0.4		
R(33;11)	-1.0 ± 0.2		
R(20;00)	0.8 ± 0.5	I(20;00)	4.5 ± 0.6
R(31;00)	1.5 ± 1.9	I(31;00)	-10.1 ± 1.7
R(31;11)	0.3 ± 1.3	I(31;11)	- 2.8 ± 1.2

Density matrix elements contributing to the moments Y_{21}, Y_{41}, and Y_{61}.

R(11;10)	-4.7 ± 0.3		
R(22;10)	-12. ± 0.2		
R(33;10)	-0.5 ± 0.2		
R(20;10)	-0.1 ± 0.2	I(20;10)	-0.9 ± 0.2
R(31;10)	0.7 ± 0.6	I(31;10)	1.7 ± 0.6
R(31;0-1)	-0.7 ± 0.7	I(31;0-1)	0.0 ± 0.8

Density matrix elements contributing to the moments Y_{10}, Y_{30}, and Y_{50}.

R(10;00)	11.6 ± 1.1	I(10;00)	9.3 ± 1.3
R(21;00)	-12.8 ± 6.1	I(21;00)	-1.3 ± 9.7
R(21;11)	- 5.1 ± 2.1	I(21;11)	-0.7 ± 3.2
R(31;00)	5.7 ± 4.7	I(32;00)	-9.3 ± 3.1
R(32;11)	1.9 ± 3.3	I(32;11)	-3.7 ± 2.2
R(30;00)	2.2 ± 2.2	I(30;00)	-1.6 ± 1.1

Density matrix elements contributing to the moments Y_{11}, Y_{31} and Y_{51}.

R(10;10)	-2.1 ± 0.3	I(10;10)	-2.0 ± 0.3
R(21;0-1)	0.3 ± 1.4	I(21;0-1)	-2.0 ± 2.1
R(21;10)	0.9 ± 1.6	I(21;10)	-4.0 ± 2.3
R(32;10)	-1.5 ± 1.6	I(32;10)	-1.4 ± 1.1
R(32;0-1)	-1.2 ± 1.6	I(32;0-1)	-3.0 ± 1.1
R(30;10)	-1.0 ± 0.4	I(30;10)	0.0 ± 0.2

TABLE IV-6. Table IV-6 shows generalized density matrix elements and their errors from the fit.

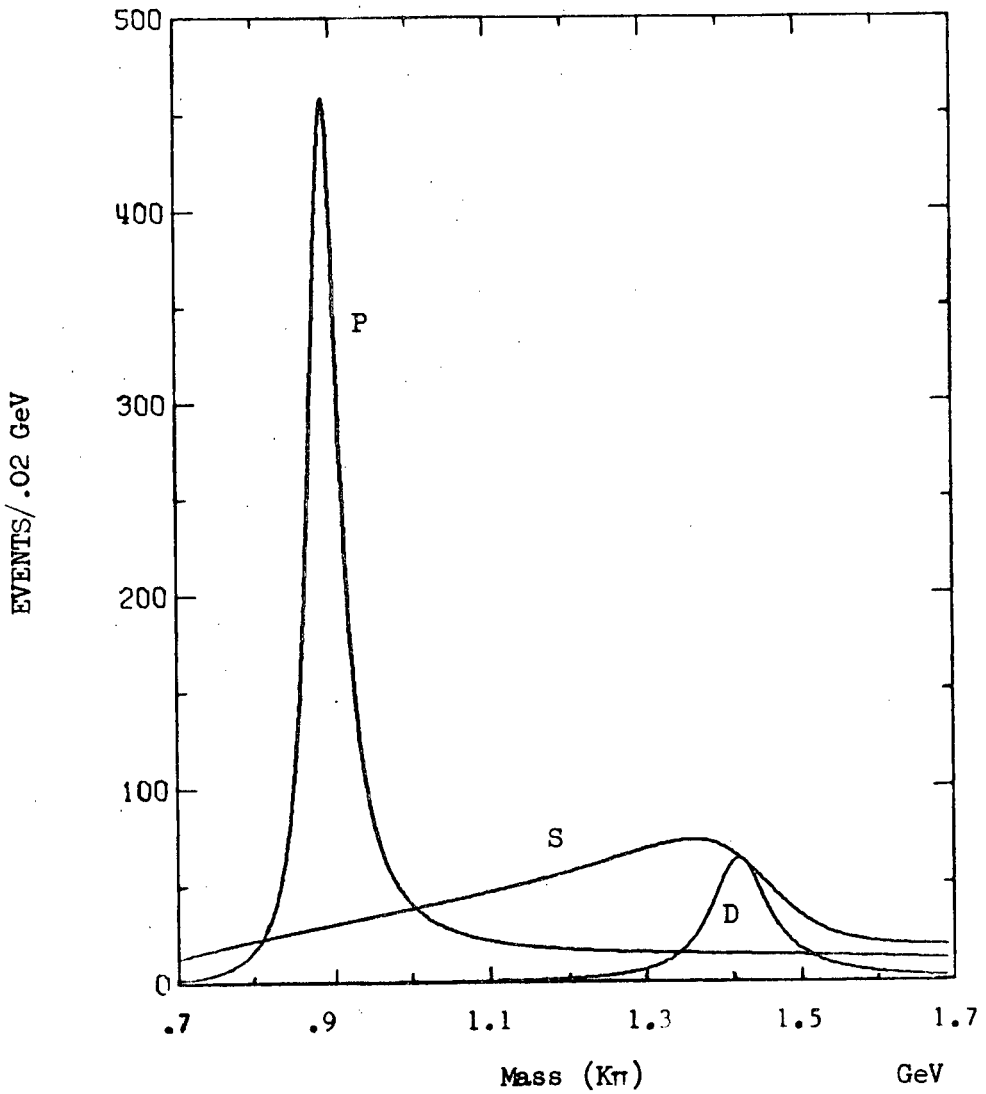

FIGURE IV-5. Figure IV-5 shows the contribution of each of the partial waves to the mass plot for the fit with a Breit-Wigner and a background term in the S, P, D and F-waves and with a peripheralized phase space given by a pole approximation. The F-wave contribution is too small to be seen in the scale used for the plot.

K*(890) region (.84-.94 GeV) has 1384.2 events in the fit.

partial wave	events	percent of total events in the fit
S	143.5 ± 5.8	(10.4 ± 0.4)%
P	1240.7 ± 55.2	(89.6 ± 4.0)%
D	0.5 ± 0.1	(0.0 ± 0.0)%
F	- 0.5 ± 0.9	(0.0 ± 0.0)%

K*(1420) region (1.34-1.54 GeV) has 1013.5 events in the fit

S	551.7 ± 22.4	(54.4 ± 2.2)%
P	137.6 ± 6.1	(13.6 ± 0.6)%
D	326.2 ± 46.0	(32.2 ± 4.5)%
F	- 2.0 ± 3.8	(-0.2 ± 0.4)%

TABLE IV-7. Table IV-7 gives the number of events and percentage of the total events in the K*(890) and K*(1420) regions according to the fit using peripheralized phase space, Breit-Wigner functions and a background term in each partial wave.

3. Third Parameterization

A. Lande has studied πP phase shifts and has concluded that they may be fit over a fairly large energy range by phase shifts obtained from a series of square well potentials.[26] In his fits a different set of square wells is used for each partial wave. It is claimed that the square well contains many relativistic features.

The following brief discussion attempts to show that relativistic features are included in the square well. Equation IV-22 is the wave equation.

$$[P_1^2 - m_1^2 + P_2^2 - m_2^2 + 2V(r)]\Psi = 0 \qquad \text{IV-22}$$

$$r = x_1 - x_2$$

Here P_1, P_2, x_1 and x_2 are 4-vectors and $V(r)$ is a "potential" which depends only upon the magnitude of the space-time separation of the two particles. The evaluation of this equation is simplest in the center of momentum frame. In this frame the change of variables of equation IV-23 simplify the problem.

$$P = P_1 + P_2$$

$$\rho = \tfrac{1}{2}(P_1 - P_2) \qquad \text{IV-23}$$

The 4-vector P is just the overall 4-momentum of the system of particles 1 and 2 while $\vec{\rho}$ is just the 3-momentum of one of the particles in the

center of momentum system. When the change of variables is made in equation IV-22, the problem separates into equations IV-24.

$$(P^2 - W^2)\Psi(X,r) = 0$$

$$[\vec{p}^2 - \vec{k}^2 + V(r)]\Psi(X,r) = 0 \qquad \text{IV-24}$$

In equation IV-24, W is just the invariant mass of the system of particles 1 and 2. The meaning of $\vec{k}$ is most easily seen in the case where V(r) vanishes for r large; in this case $\vec{k}$ is just the 3-momentum of one of the particles in the center of momentum frame. Equation IV-25 gives the relation between W and $\vec{k}^2$ in the region where V(r) vanishes.

$$\vec{k}^2 = \frac{W^4 + m_1^4 + m_2^4 - 2W^2m_1^2 - 2W^2m_2^2 - 2m_1^2m_2^2}{4W^2} \qquad \text{IV-25}$$

Equation IV-25 is just the standard equation relating the 3-momentum in the rest frame of the system of particles 1 and 2 to the invariant mass of the system. Hence outside the interaction region equations IV-24 are an expression of relativistic kinematics.

In the center of momentum frame assume that the potential is given by equation IV-26.

$$V(r) = 0 \text{ for } r^2 > A^2,\ t_1 = t_2$$

$$= -\alpha^2 \text{ for } r^2 \leq A^2,\ t_1 = t_2 \qquad \text{IV-26}$$

Once the potential has been described in the center of momentum frame, it is defined in all frames which may be reached by a Lorentz transformation.

Substituting this potential into equation IV-24, one obtains the set of differential equations of equation IV-27.

$$\vec{\rho}^2\psi = \vec{k}^2\psi \qquad r > A$$

$$\vec{\rho}^2\psi = \left(\vec{k}^2 + \alpha^2\right)\psi \qquad r \leq A \qquad \text{IV-27}$$

This is just a square well problem and the solution of the scattering phase shift may be written down at once. Following Messiah's solution for scattering from a square well, the phase shift is given by equation IV-28.[27]

$$\frac{K\, j_\ell'(KA)}{j_\ell(KA)} = \frac{k\left(\cos\delta_\ell\, j_\ell'(kA) + \sin\delta_\ell\, n_\ell'(kA)\right)}{\cos\delta_\ell\, j_\ell(kA) + \sin\delta_\ell\, n_\ell(kA)} \qquad \text{IV-28}$$

$$K^2 = k^2 + \alpha^2$$

Here j_ℓ is the spherical Bessel function of order ℓ and n_ℓ is the spherical Neumann function of order ℓ. The prime (') indicates the first derivative of the Bessel function. For an S-wave, equation IV-28 reduces to equation IV-29.

$$\delta_o = -kA + \tan^{-1}\left(\frac{k}{K}\tan KA\right) \qquad \text{IV-29}$$

in the square well parameterization, the quantities B_J of equation IV-13 are parameterized according to equation IV-30.

$$B_J = f_J \sin\delta_J e^{i\delta_J} \qquad \text{IV-30}$$

Here f_J is a form factor. Some form factor is required since for small P, δ_J goes like P^{2J+1} while it is known that at small P, B_J should go like P^J. Here P is the momentum of the final K in the rest frame of the $K\pi$ system. After studying the procedure used by Beaupre et al. in extracting $\pi\pi$ phase shifts, the form factor f_J was taken to be given by equation IV-31.[28]

$$f^2 = \frac{1}{P^2} \frac{u_J(R_J P_o)}{u_J(R_J P)}$$

$$u_J(x) = \frac{1}{2x^2} Q_J\left(1 + \frac{1}{2x^2}\right) \qquad \text{IV-31}$$

$$\sim x^{2J} \text{ for } x \ll 1$$

$$\sim \frac{1}{4x^2} \ln(4x^2) \text{ for } x \gg 1$$

Here Q_J is a Legendre function of the second kind and of order J. The functions u_J are the Benecke-Dürr functions for angular momentum J.[29] R_J is a constant; P is the momentum of the final K in the rest frame of the $K\pi$ system. P_o is a normalization constant which was usually taken as the momentum at which the phase shift passes through 90°.

This parameterization can be looked upon as being just another method of parameterizing the individual partial waves. In a sense it is entirely equivalent to the parameterization using Breit-Wigner functions plus a background term. However instead of four parameters there are only three parameters in each partial wave.

More optimistically the parameterization may have a greater validity. However the validity is only approximate because no inelasticities were put into the partial waves. Even so the resulting phase shifts may be compared with those taken from various extrapolations to the π pole. Unlike the first parameterization, once a resonance has been put into a partial wave with a fixed central value and a fixed width, only one additional parameter, R_J, remains to be adjusted. In particular the phase, δ_J, becomes a function of mass and cannot be arbitrarily adjusted outside the resonance region.

In fitting, the peripheralized phase space of the second parameterization was used. For the P, D and F-partial waves, the phase shift was required to pass through 90° at the resonant mass. This was done by adjusting the well depth, α, for a given width and resonant mass until equation IV-32 was satisfied.

$$\frac{K}{k}\,\frac{j_\ell'(KA)}{j_\ell(KA)} = \frac{n_\ell'(kA)}{n_\ell(kA)} \qquad \text{IV-32}$$

Equation IV-32 was obtained from equation IV-29 by setting δ equal 90°; k and K are evaluated at the resonant mass. In fitting the P, D and F-partial waves the width of the well, A, the resonant mass, m_o, and the constant, R_J, were adjusted.

Unfortunately the mass dependence of the S-partial wave is relatively unknown; hence much freedon is possible in determining the S-wave square well parameters. Four different types of behavior were tried for the S-wave phase shift. Some of these fits were more successful than others; however none was as successful as either of the fits which used a Breit-Wigner and a background. Nevertheless these fits are interesting and will be briefly described.

In the first case the square well parameters were adjusted so that the S-wave phase shift agreed as well as possible with the S-wave phase shift in the K*(890) region as taken from a $K\pi$ phase shift analysis in reaction IV-33.[30]

$$K^+P \rightarrow K^+\pi^-\Delta^{++} \qquad \text{IV-33}$$

In this case the S-wave phase shift was found to slowly increase but never reach 90° for $K\pi$ masses below 1.7 GeV. This solution gave good agreement in the K*(890) region; however the K*(1420) region was poorly fit partially because there were not enough events on the low mass side of the K*(1420) and partly because there were too many events on the high mass side of the K*(1420).

In the second case, the phase shift was required to be a multiple of 180° for some mass between 1.6 and 1.7 GeV as suggested by Firestone et al. who performed a pole extrapolation in reaction IV-34 at 12 GeV/c.[25]

$$K^+N \rightarrow K^+\pi^-P \qquad \text{IV-34}$$

Many sets of square well parameters gave this type of behavior. In order to restrict the parameters even further, the phase shift was required to produce an excess of events in the region of 1.3 GeV. The resulting phase shift was found to oscillate about 0° and to be small. Peaks occur in the S-wave between .74 and .75 where δ_o is -.0335 rad and between 1.30 and 1.31 GeV where δ_o is .0701 rad. The phase shift is zero between .98 and .99 GeV and between 1.70 and 1.71 GeV.

In the third case, the S-wave phase shift was required to be 90° at about .725 GeV, the mass at which a peak was once seen in the $K\pi$ mass spectrum.[31] Many sets of square well parameters gave a phase shift which goes to 90° almost at threshold and then remains near 90°. Again in order to restrict the parameters even further, the phase shift was required to produce an excess of events in the region of 1.3 GeV. The resulting phase shift was found to be antiresonant. It produced antiresonances between .76 and .77 GeV and between 1.35 and 1.36 GeV. The phase shift was a multiple of 180° between 1.02 and 1.03 GeV and between 1.69 and 1.70 GeV. Not too surprisingly $\sin^2\delta$ for the second and third square well parameters was roughly identical in shape. However the rapid variation of the S-wave phase shift of the third square well was found to give poor fits to the interference moments Y_{10} and Y_{11}. Consequently the chi square for the third square well was considerably higher than for the second square well. This suggests that the S-wave phase shift must be a slowly varying function of the mass of the $K\pi$ system.

In the fourth case, the S-wave phase shift was required to be 90° around 1.30 GeV, where the down-down solution of Firestone et al. passes through 90°.[25] In order to further restrict the S-wave square well

parameters, the phase shift was required to remain relatively constant over a fairly large $K\pi$ mass region between the K*(890) and the K*(1420) in agreement with the results of the fit by Firestone et al.[25] After fitting the moments, the resulting phase shift was found to be anti-resonant, to pass through -90° at 1.23 GeV, to remain relatively close to -78° between .85 and 1.18 GeV and to pass through -180° between 1.71 and 1.72 GeV.

The remainder of Section C3 will be devoted to elaborating further upon the fourth set of square well parameters. There are two reasons for this. First, all of the fits have many features in common which may provide further insight into the mass dependence of partial waves, especially the resonant partial waves. Second, the behavior of the absolute value of the S-wave phase shift is very similar to the S-wave behavior found by Firestone et al. in their down-down solution; hence the fit may have some truth to it.[25]

In the fourth square well fit, the resonant mass, m_{0J}, width of the square well, A_J, and the constant R_J were adjusted to obtain a best set of square well parameters in a chi squared sense. For each m_{0J} and A_J the square well depth, α_J, was adjusted so that the phase shift was an odd-integral multiple of 90°. Table IV-8 shows the values of m_{0J}, A_J, α_J, and R_J for the fit.

Unlike the fits using a Breit-Wigner and a background term in each partial wave, the F-wave resonance was not constrained to lie at 1.760 GeV and to have a width of 60 MeV. The resulting fit pushed the location of the F-wave resonance to 1.93 GeV which is nearly 20 MeV above the

	S	P	D	F
A	7.51	0.608	1.769	3.79
α	4.79	10.314	4.288	2.18
m_o	1.23	0.8934	1.430	1.93
R	2.04	0.00127	0.00132	0.012

TABLE IV-8. Table IV-8 shows the values of the square well width, A, the well depth, α, the resonant mass, m_o, and the form factor constant, R_J, for the fit.

upper edge of the mass region used in the fit. For this reason the F-wave square well parameters should not be taken seriously.

Figure IV-6 shows the mass dependence of the phase shifts for the S, P, D and F-partial waves. The behavior of the P-wave phase shift above the K*(890) is typical of the behavior of a square well phase shift above a resonance. Unlike the Breit-Wigner, the square well does not force the phase shift to go to 180° at $K\pi$ masses much higher than the resonant mass. From Figure IV-6 it can be seen that the P-wave phase shift levels off at about 160°.

Figures IV-7a-m show the moments and the results of the fit for moments with m less than 2 and L less than 7. In the fit all generalized density matrix elements with m values larger than 1 were set to zero. Table IV-9 shows the raw numbers obtained for the generalized density matrix elements and their errors.

Figure IV-8 shows the contribution of each of the partial waves to the mass plot. From the figure it is possible to estimate the number

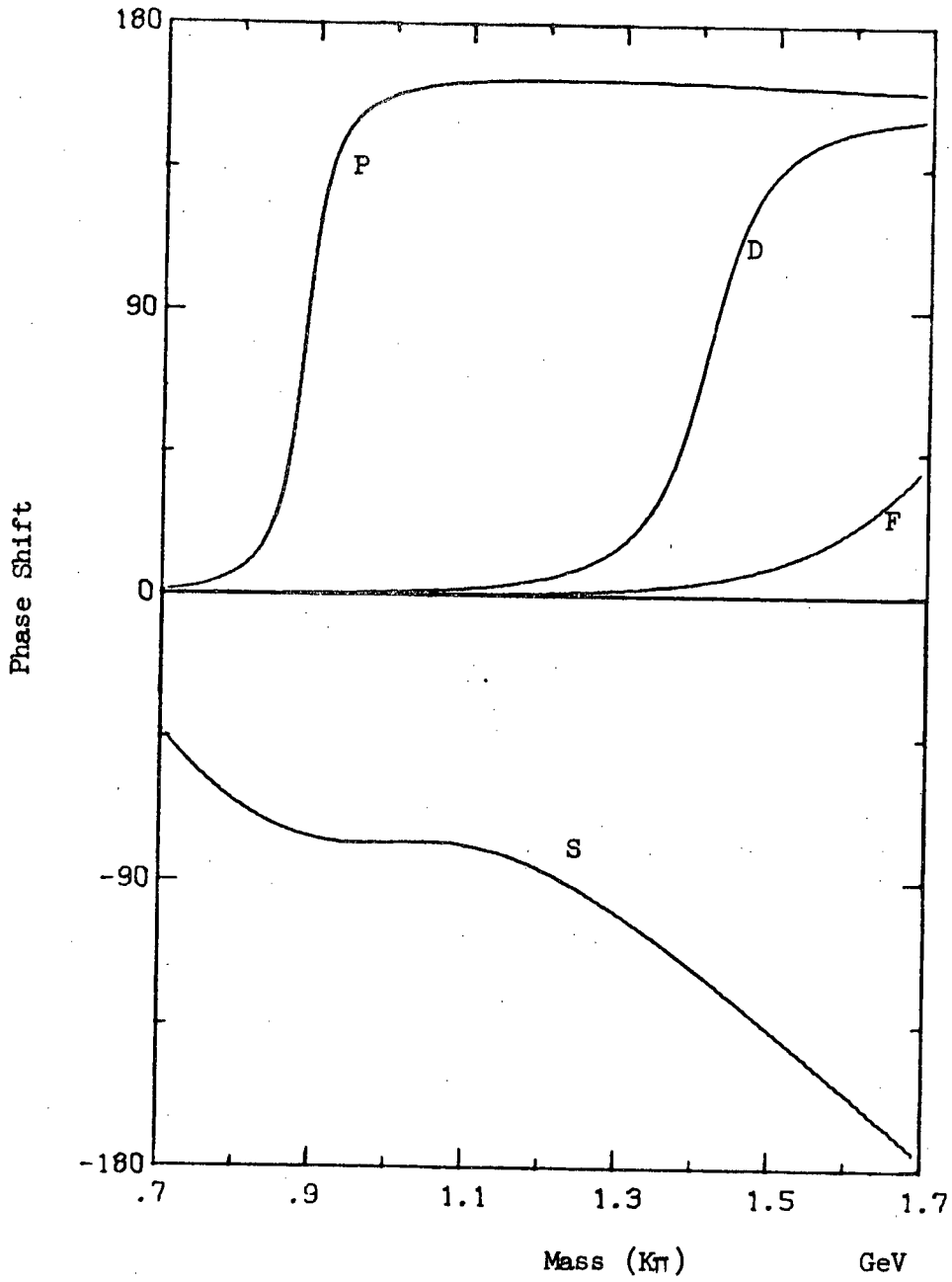

FIGURE IV-6. Figure IV-6 shows the mass dependence of the Kπ phase shift for the S, P, D and F-partial waves for the fit with square well potentials and a peripheralized phase space given by a pole approximation.

FIGURE IV-7. Figure IV-7 shows the mass dependence of the moments with respect to Y_{Lm} in the Jackson frame for the Kπ system. The curves are the result of a fit with square well potentials and a peripheralized phase space given by a pole approximation.

IV-7a

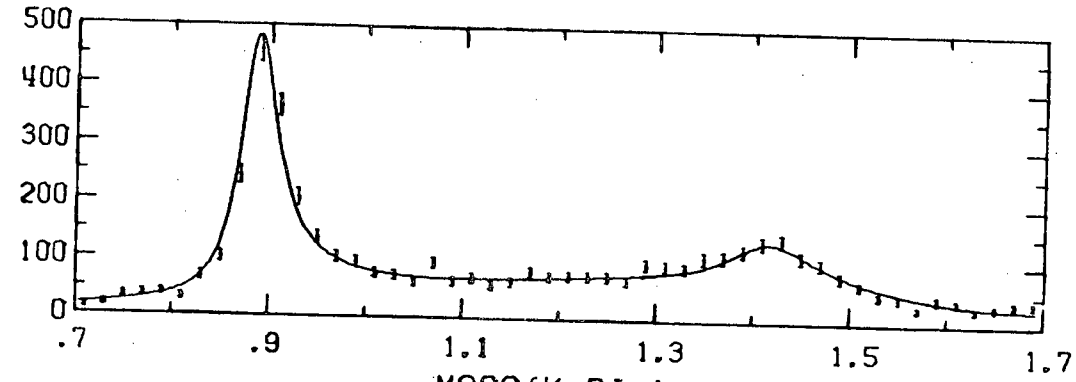

IV-7b

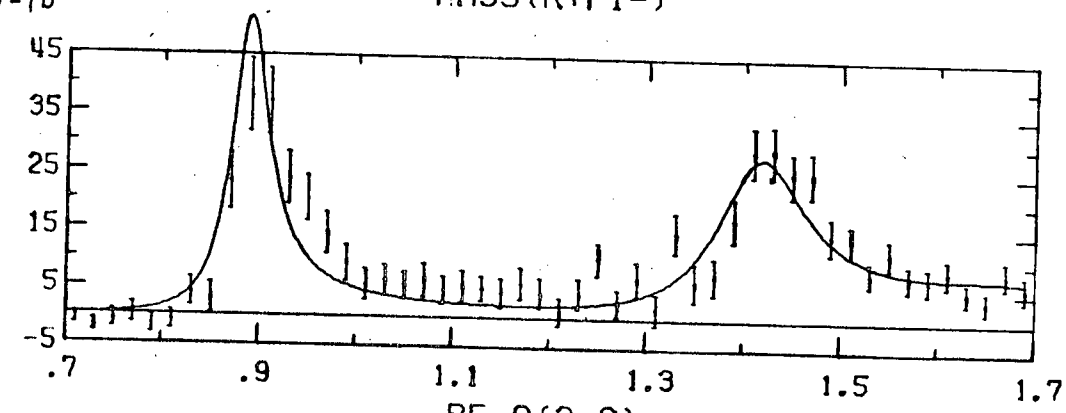

IV-7c

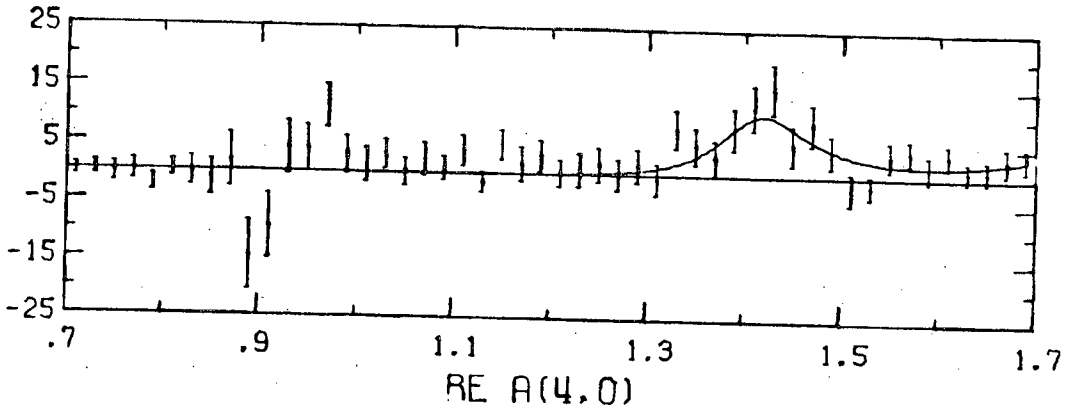

IV-7d

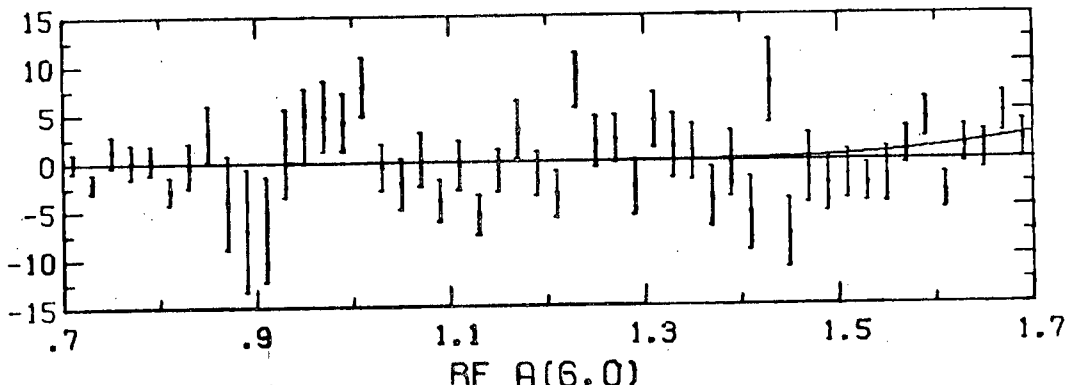

IV-7e

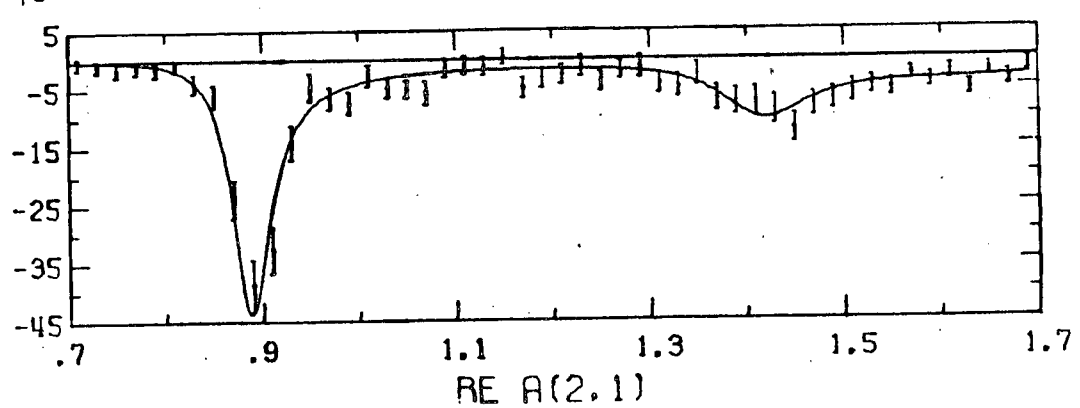

IV-7f

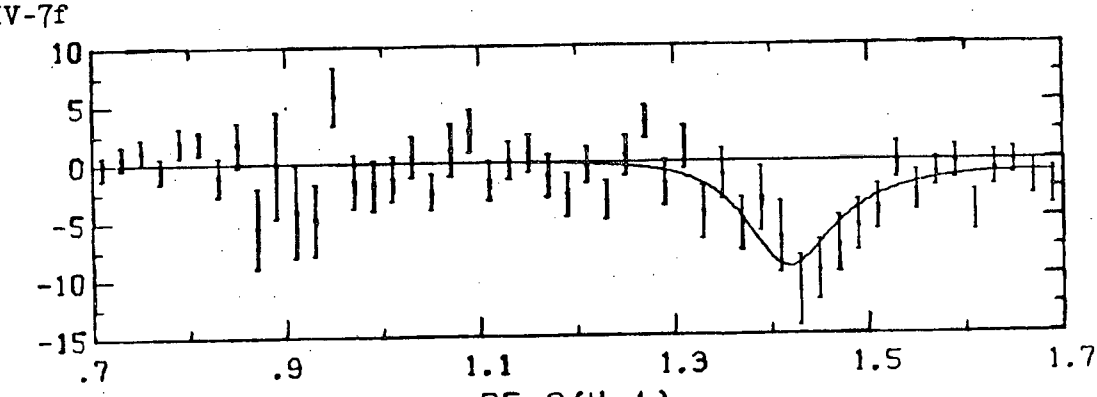

IV-7g

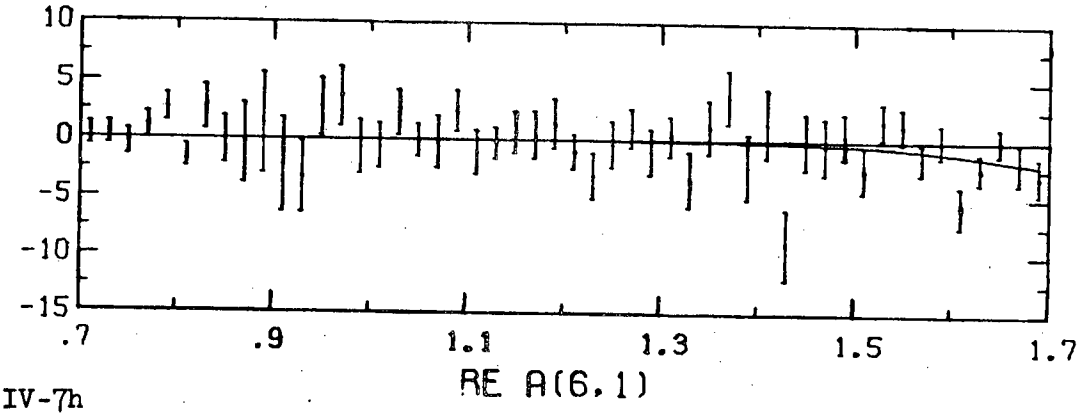

IV-7h

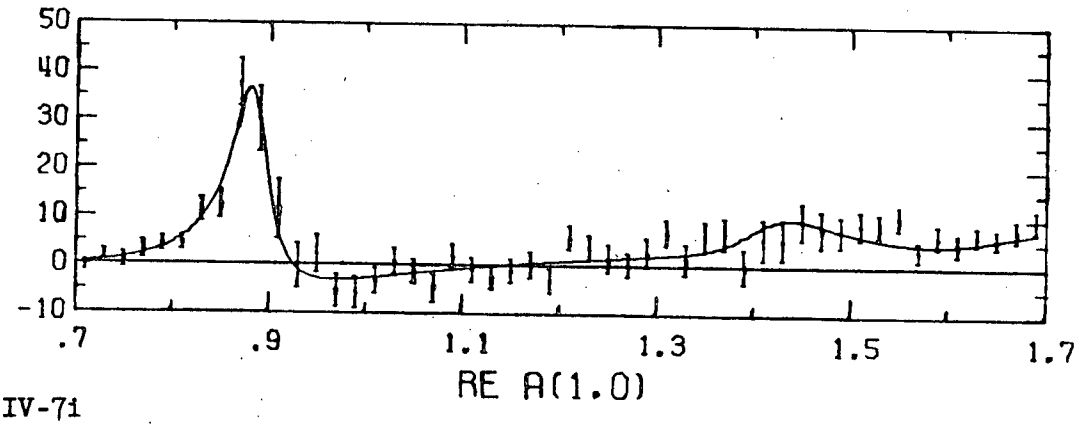

IV-7i

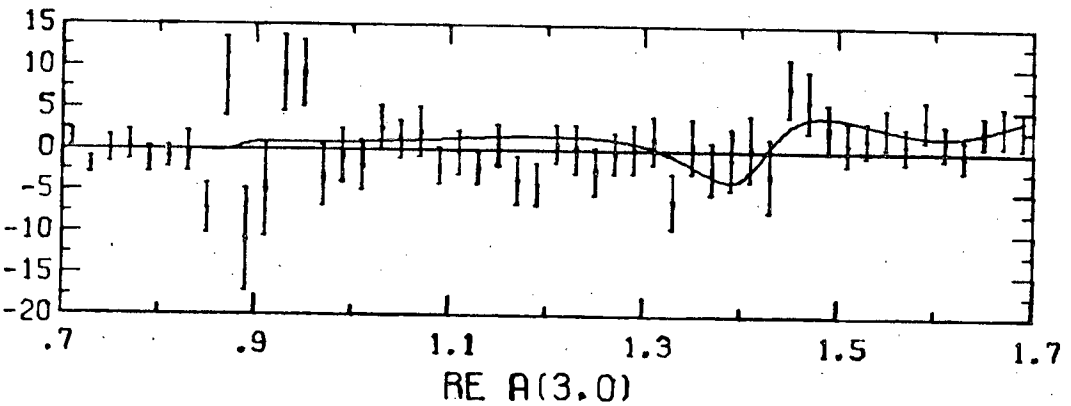

IV-7j

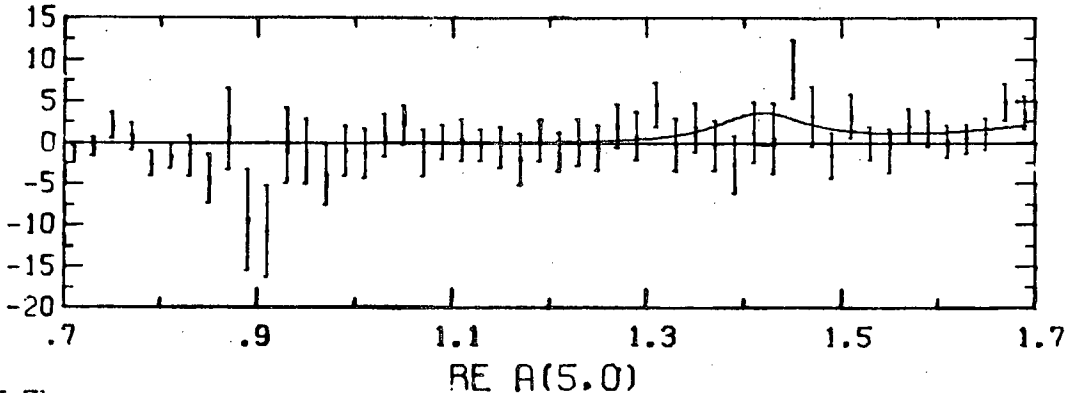

IV-7k

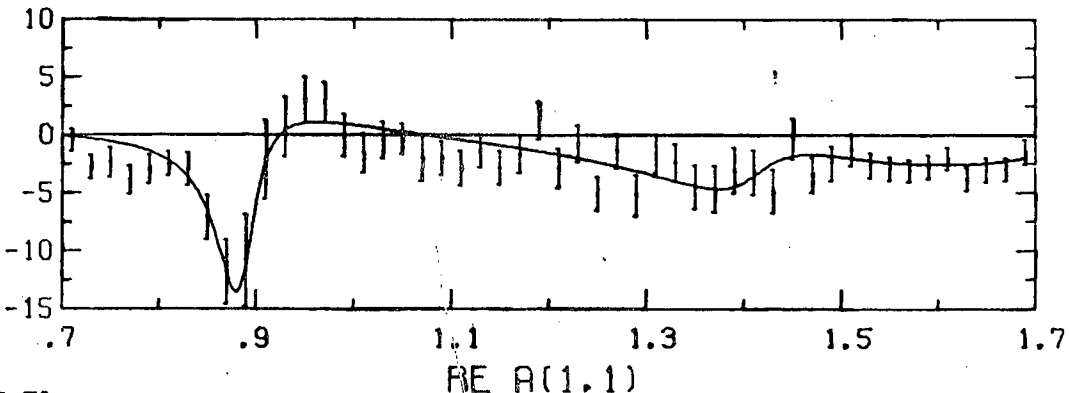

IV-7l

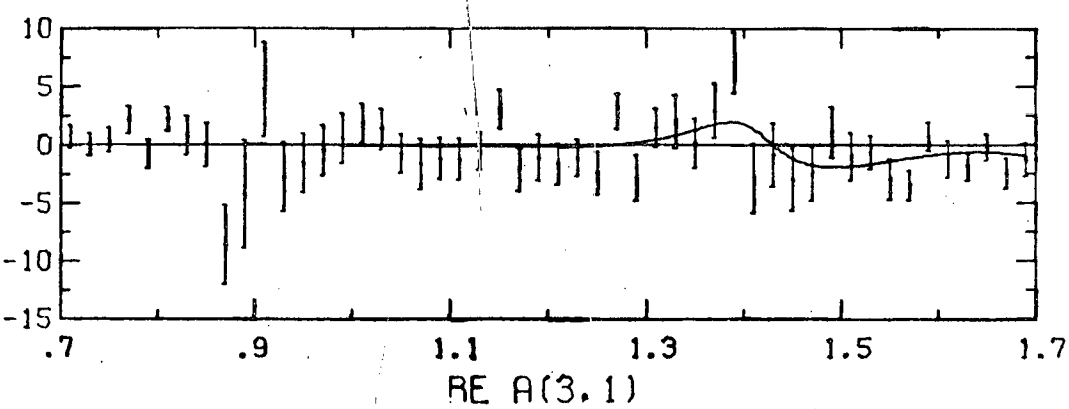

IV-7m

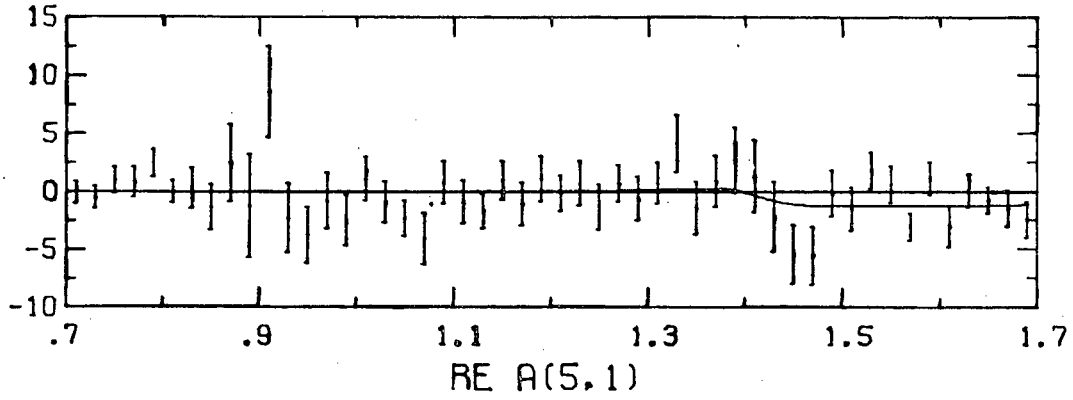

Density matrix elements contributing to Y_{00} (mass plot), Y_{20}, Y_{40} and Y_{60}.

R(JJ';mm')		I(JJ';mm')	
R(00;00)	4.7 ± 0.2		
R(11;00)	22.5 ± 0.9		
R(11;11)	6.3 ± 0.5		
R(22;00)	4.9 ± 0.5		
R(22;11)	0.8 ± 0.3		
R(33;00)	1.4 ± 0.2		
R(33;11)	0.2 ± 0.1		
R(20;00)	1.8 ± 0.4	I(20;00)	0.8 ± 0.3
R(31;00)	-2.8 ± 2.8	I(31;00)	-1.8 ± 1.8
R(31;11)	-6.2 ± 1.8	I(31;11)	1.5 ± 1.2

Density matrix elements contributing to the moments Y_{21}, Y_{41}, and Y_{61}.

R(11;10)	-4.0 ± 0.2		
R(22;10)	-0.9 ± 0.2		
R(33;10)	-0.3 ± 0.1		
R(20;10)	-0.3 ± 0.1	I(20;10)	-0.2 ± 0.1
R(31;10)	2.0 ± 0.9	I(31;10)	-0.4 ± 0.5
R(31;0-1)	3.1 ± 1.1	I(31;0-1)	0.0 ± 0.7

Density matrix elements contributing to the moments Y_{10}, Y_{30}, and Y_{50}.

R(10;00)	3.4 ± 0.7	I(10;00)	-6.6 ± 0.6
R(21;00)	-17.9 ± 3.3	I(21;00)	-17.4 ± 5.0
R(21;11)	- 8.6 ± 1.6	I(21;11)	-11.1 ± 1.5
R(32;00)	-12.4 ± 2.6	I(32;00)	- 2.1 ± 0.6
R(32;11)	- 9.9 ± 1.8	I(32;11)	0.1 ± 0.4
R(30;00)	- 4.5 ± 1.1	I(30;00)	- 2.0 ± 0.6

Density matrix elements contributing to the moments Y_{11}, Y_{31}, and Y_{51}.

R(10;10)	-0.6 ± 0.2	I(10;10)	1.3 ± 0.2
R(21;0-1)	9.0 ± 1.3	I(21;0-1)	6.3 ± 1.0
R(21;10)	7.5 ± 1.1	I(21;10)	5.0 ± 1.3
R(32;10)	5.1 ± 1.0	I(32;10)	0.2 ± 0.2
R(32;0-1)	4.9 ± 1.0	I(32;0-1)	0.0 ± 0.2
R(30;10)	0.5 ± 0.2	I(30;10)	0.5 ± 0.1

TABLE IV-9. Table IV-9 shows the raw numbers obtained for the generalized density matrix elements and their errors.

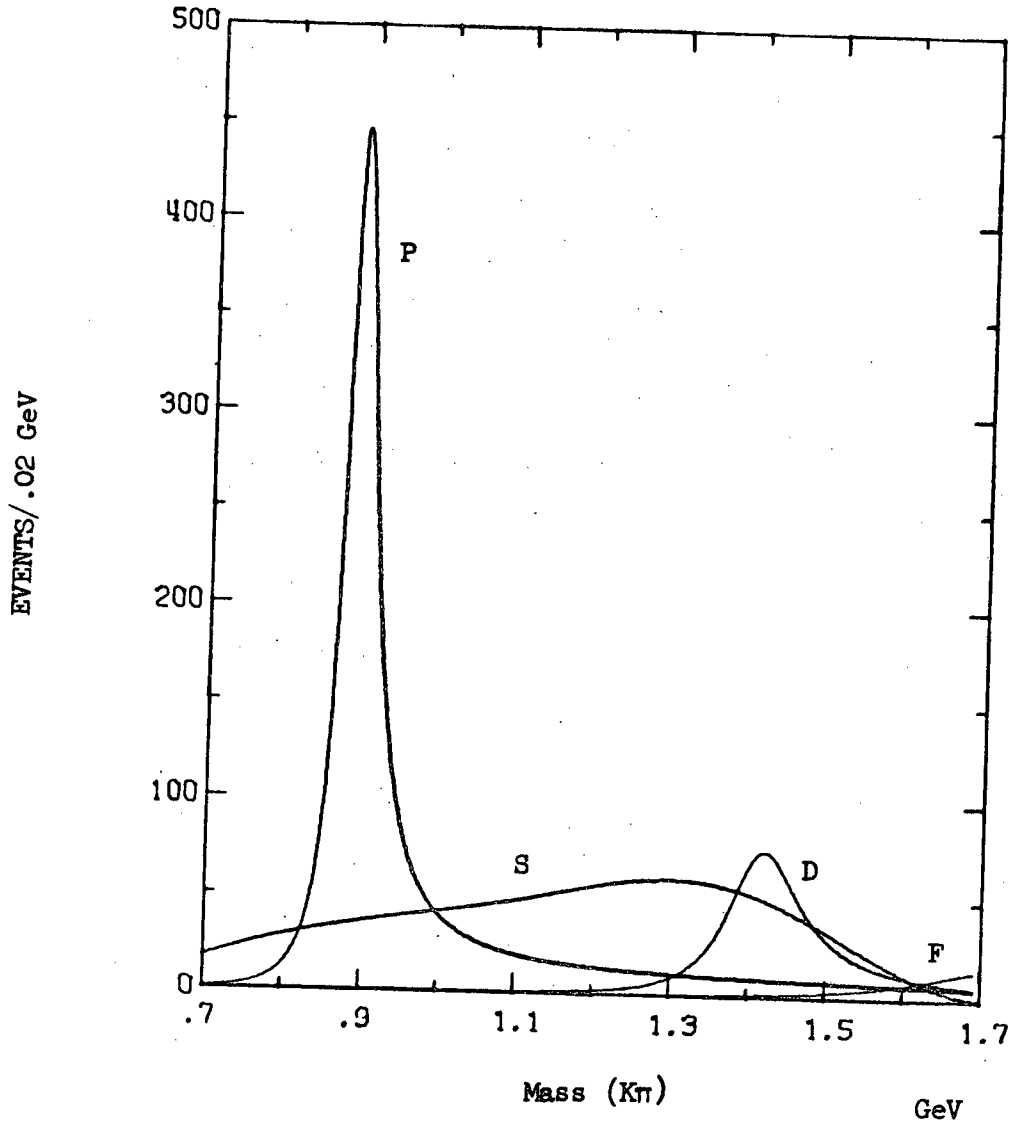

FIGURE IV-8. Figure IV-8 shows the contribution of each of the partial waves to the mass plot for the fit with square well potentials and a peripheralized phase space given by a pole approximation.

of events in the background under the K*(890) and K*(1420). Table IV-10 shows the results of these estimates.

D. Conclusions

In the last section three different fits for the decay angular distributions in the $K\pi$ Jackson frame were described. All three fits were able to account for the major structure observed in the moments. The first two fits had a chi square of 1.05 or less per degree of freedom, while the third fit had a chi square of 1.15 per degree of freedom.

The moments were fit by several hypotheses. The agreement between the fits in the K*(890) region was fairly good (see Tables IV-4, IV-7, and IV-10). The agreement in the K*(1420) region was not as good; however the fits do suggest that between 37% and 54% of the mass plot in the K*(1420) region is due to S-wave(see Tables IV-4, IV-7 and IV-10). Although it was not possible to find a unique mass behavior for either of the S or F-partial waves, fitting procedure was able to eliminate many mass dependences as being inconsistent with the behavior of the moments.

The main advantages of the model are that it is able to parameterize the mass dependence of the moments, and it is able to rule out some mass dependences for the various partial waves. On the other hand, the fitting program does not yield a unique solution for the behavior of the partial waves.

In addition, all of the fits have a few generalized density matrices which are unphysical. That is, equations like IV-14 and IV-15 are not always satisfied. This problem especially arises in regions

K*(890) region (.84-.94 GeV) has 1374.8 events in the fit.

partial wave	events	percent of total events in the fit
S	175.7 ± 6.9	(12.8 ± 0.5)%
P	1199.1 ± 47.8	(87.2 ± 3.5)%
D	0.0 ± 0.0	(0.0 ± 0.0)%
F	0.0 ± 0.0	(0.0 ± 0.0)%

K*(1420) region (1.34-1.54 GeV) has 1016.4 events in the fit.

S	453.0 ± 17.9	(44.6 ± 1.8)%
P	86.2 ± 3.4	(8.5 ± 0.3)%
D	457.5 ± 54.3	(45.0 ± 5.3)%
F	19.7 ± 3.3	(1.9 ± 0.2)%

TABLE IV-10. Table IV-10 shows the number of events and the percentage of the total events in the K*(890) and K*(1420) regions according to the fit using peripheralized phase space and phase shifts from square wells.

where many generalized density matrix elements contribute to a moment; then the fit adjusts the density matrix elements so as to minimize the chi square. As a result when a density matrix is relatively large over a fairly small mass region, the fit may make the contribution of that density matrix element so large that it badly violates the equations of constraint. This is especially true whenever the F-wave interferes with P, D or F-waves and for some of the interferences between P and D-partial waves.

This latter problem is a serious criticism of the model and one that is hard to fix up. One way of making the generalized density matrix elements physical would be to write them down in terms of the amplitudes S_{Jm} (see equation IV-11). This procedure would also have the advantage of allowing the amplitudes for the same partial wave to have slightly different mass dependences as is suggested by various exchange models.

V. THE EFFECT OF FIRESTONE ET AL.

A. Introduction

In a K^+D experiment at 12 GeV/c, Firestone et al. found evidence for an additional resonance in the region of the K*(1420) in the charge exchange reaction V-1.[4]

$$K^+N \rightarrow K^+\pi^-P \qquad \text{V-1}$$

They suggest that the enhancement is a resonance with a mass of about 1.370 GeV and a width of less than .150 GeV. They interpret the enhancement as having J^P equal to 0^+ and as being produced by pion exchange.

An examination of the $K^+\pi^-$ mass spectrum in the region of the K*(1420) for this experiment (Figure V-1a) reveals a shoulder on the low side of the K*(1420). Following the procedure of Firestone et al., the K*(1420) region was examined under equatorial (Figure V-1b) and polar (Figure V-1c) cuts on the Kπ Jackson cosine. Since it had been suggested that the low-mass enhancement was 0^+, the polar cut was given by equation V-2.

$$\cos \Theta_{K\pi} > .746 \qquad \text{V-2}$$

Such a cut maximizes the separation of S and D-waves when the D-wave is produced by pion exchange.

The Jackson cosine in the K*(1420) region exhibits considerable asymmetry. For this reason the forward and backwards polar regions were

V-1a

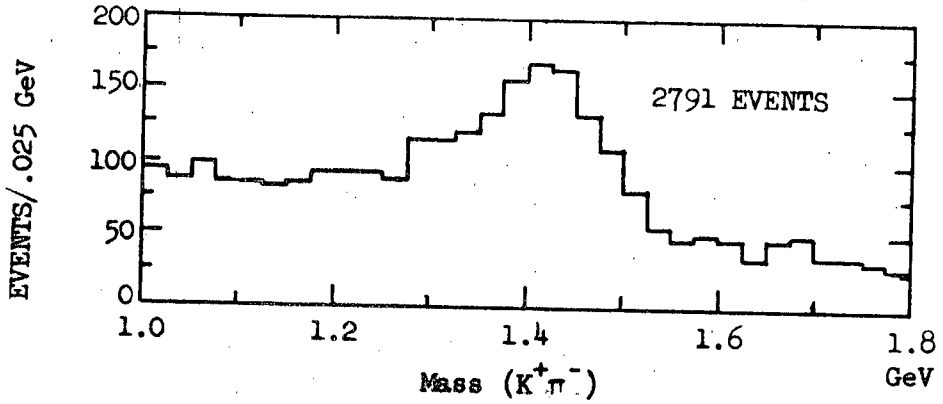

V-1b

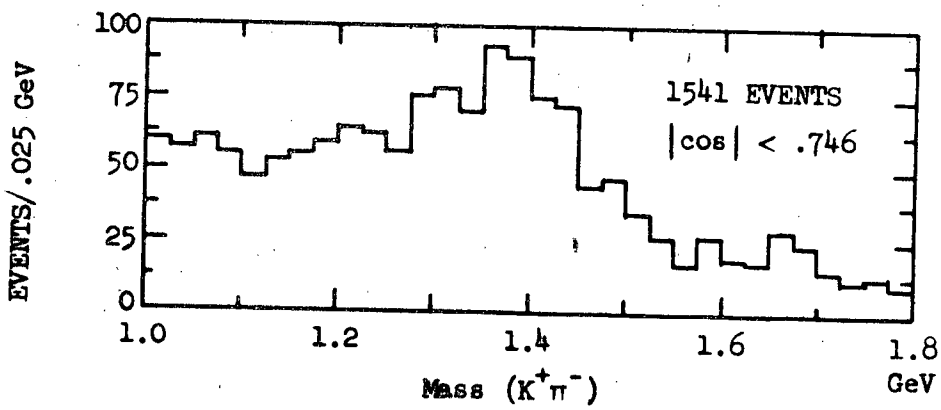

V-1c

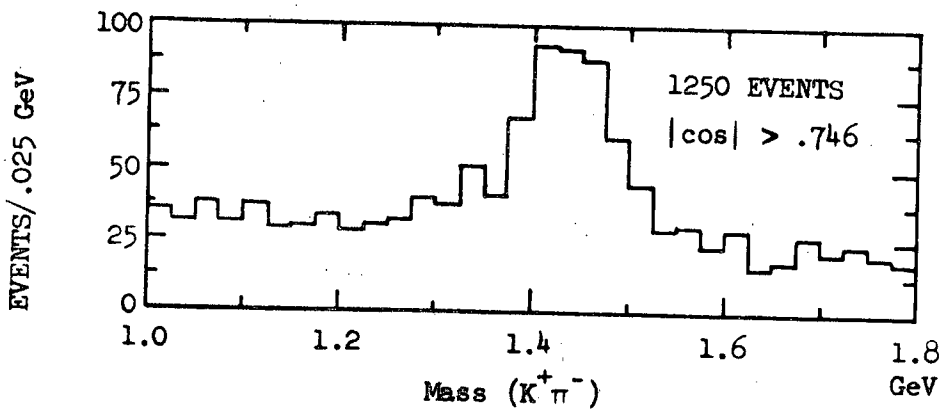

Figure V-1. Figure 1a shows the $K\pi$ mass spectrum for the reaction $K^+D \rightarrow K^+\pi^-PP_s$ at 3.8 GeV/c. Figure 1b shows the $K\pi$ mass spectrum when the absolute value of the Jackson cosine for the $K\pi$ system is required to be less than .746. Figure 1c shows the $K\pi$ mass spectrum when the absolute value of the Jackson cosine is greater than .746.

compared and the forwards and backwards equatorial regions were compared. However no statistically significant differences were seen in either case.

The mass plot was subjected to t' cuts as well as polar and equatorial cuts. Table V-1 shows the results of fitting the mass plots with one Breit-Wigner function in the K*(1420) region. Table V-2 shows the results of fitting the mass plots with S and D-Breit-Wigner functions in the K*(1420) region. Summarizing these fits, it is clear that the peaking in the equatorial region occurs at lower masses than the peaking in the polar region. Ignoring the high t' region, the peaking of the D-wave is the same in the polar cuts and in the mass fits using two Breit-Wigners; however the widths are different with the narrower widths appearing in the two Breit-Wigner fits. The fits in the equatorial region show considerable fluctuation; however the width also appears wide. The agreement between the equatorial fit and the S-wave part of the two BW fit is not as good as was the case for the D-wave. These fits suggest that if there is an S-wave resonance, its width is fairly wide. In such a case, changes in the shape of phase space due to cuts on t' could cause an apparent shift in the location of the central value of the S-wave resonance. In any event, enhancement seen at 3.8 GeV/c seems to be wider than the effect seen by Firestone et al. at 12.0 GeV/c.

If the enhancement is a 0^+ resonance produced by pion exchange, a similar enhancement is expected in the $K\pi$ system for reaction V-3 where pion exchange is dominant.

$$K^+P \rightarrow K^+\pi^-\Delta^{++} \qquad \text{V-3}$$

Over all mass plot

t' cut	m_D (GeV)	Γ_D (GeV)	χ^2/data point
all t'	1.422 ± .005	.16 ± .02	1.14
$t' < .08$	1.404 ± .013	>0.3	1.24
$.08 < t' < .3$	1.414 ± .007	.16 ± .03	0.80
$.3 < t'$	1.448 ± .009	.22 ± .04	0.98

Polar region $|\cos\theta| > .746$

all t'	1.448 ± .004	.15 ± .02	1.09
$t' < .08$	1.446 ± .006	.13 ± .03	0.99
$.08 < t' < .3$	1.436 ± .006	.14 ± .03	0.85
$.3 < t'$	>1.470	.16 ± .03	0.85

Equatorial region $|\cos\theta| \leq .746$

t' cut	m_S (GeV)	Γ_S (GeV)	χ^2/data point
all t'	1.38 ± .01	.17 ± .03	1.28
$t' < .08$	1.31 ± .02	>.3	0.86
$.08 < t' < .3$	1.36 ± .01	.14 ± .03	0.83
$.3 < t'$	1.41 ± .01	.20 ± 0.6	1.07

TABLE V-1. Table V-1 shows the results of fitting the mass plots with one Breit-Wigner function in the K*(1420) region.

t' cut	m_D (GeV)	Γ_D (GeV)	m_S (GeV)	Γ_S (GeV)	χ^2/data point
all t'	1.434 ± .005	.10 ± .02	1.34 ± .02	.178 ± .06	.96
t' < .08	1.431 ± .006	< .06	1.33 ± .02	> .03	.84
.08 < t' < .3	1.43 ± .01	.08 ± .03	1.39 ± .02	.18 ± .04	.70
.3 < t'	1.449 ± .009	.20 ± .04	< 1.25	.13 ± .14	.95

TABLE V-2. Table V-2 shows the result of fitting the mass plots with S and D Breit-Wigner functions in the K*(1420) region.

Figure V-2a shows the mass plot in the region of the K*(1420) for reaction V-3 when the data from experiments at 5.0, 5.5 and 7.3 GeV/c are combined.[32] Figures V-2b and c show the effect of polar and equatorial cuts upon the data of Figure V-2a. Table V-3 shows the result of fitting the K*(1420) region of these mass plots. When the fits of Table V-3 are compared with the fits in Tables V-1 and V-2, it is seen that the fits for the D-wave resonance parameters are roughly consistent for comparable fits. The central value of the S-wave resonance is also comparable; however the width of the S-wave for the K^+P reaction is much wider than the width for the K^+N reaction. In fact the S-wave resonance is so wide that it might best be described as an S-wave background.

There are several possible explanations for the differences between the 12.0 GeV/c K^+N data, the 3.8 GeV/c K^+N data and the combined K^+P data at 5.0, 5.5 and 7.3 GeV/c. Unfortunately these hypotheses explain some of the differences but not others. The 0^+ effect observed at 12.0 GeV may be produced at very small t values. In this case the kinematic boundary of K^+N at 3.8 GeV/c and the kinematic boundary for the combined K^+P data would prevent sufficiently small t values from being reached. If this is the case, then it is hard to understand the data for K^+N at 3.8 GeV/c.

A second explanation is that the effect in K^+N at 3.8 GeV/c and 12.0 GeV/c is the same, but the enhancement is not produced by pion exchange. In this case there would be no reason why the K^+P reaction should exhibit the effect since pion exchange is dominant. Table V-4 shows the results of fitting the $K\pi$ mass plot for K^+N at 3.8 GeV/c for different t' cuts. In these fits the S-wave central value was 1.385 GeV

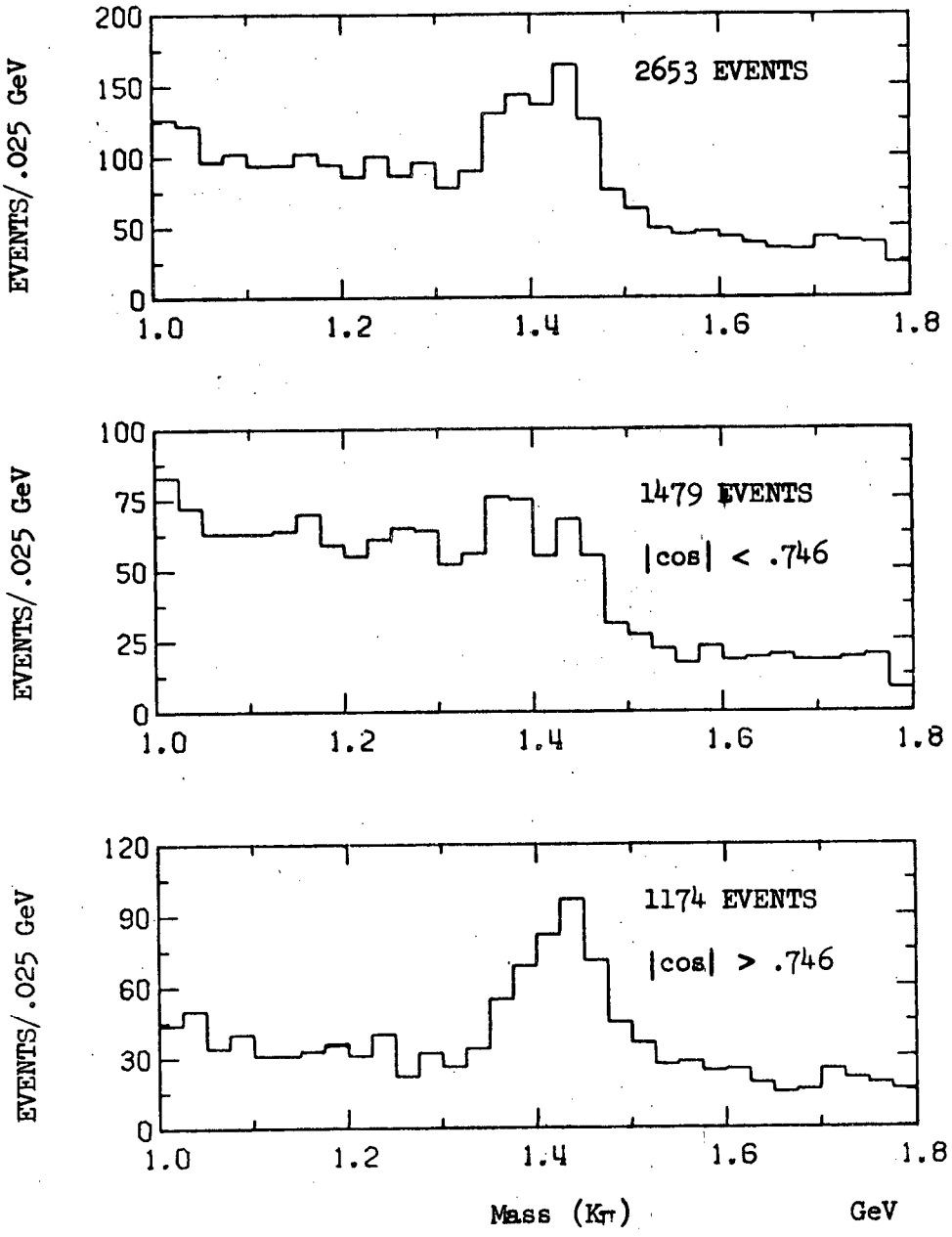

FIGURE V-2. Figure V-2 shows the Kπ mass spectrum for the reaction $K^+P \rightarrow K^+\pi^-\Delta^{++}$ when data from experiments at 5.0, 5.5 and 7.3 GeV/c are combined.[32] Figure V-2b shows the Kπ mass spectrum when the absolute value of the Jackson cosine for the Kπ system is required to be less than .746. Figure V-2c shows the Kπ mass spectrum when the absolute value of the Jackson cosine is greater than .746.

	m_D (GeV)	Γ_D (GeV)	m_S (GeV)	Γ_S (GeV)	χ^2/data point
all events	1.422 ± .005	.13 ± .02	---	---	1.52
all events	1.427 ± .005	.10 ± .01	1.35 ± .05	> .6	1.16
polar region cos θ > .746	1.438 ± .003	.12 ± .01	---	---	1.05
equatorial region cos θ < .746	---	---	1.36 ± .01	.3 ± .1	1.35

TABLE V-3. Table V-3 shows the result of fitting combined data from 5.0, 5.5 and 7.3 GeV/c for the reaction $K^+P \rightarrow K^+\pi^-\Delta^{++}$ in the K*(1420) region. The Δ^{++} region is defined by $m_{P\pi}$ between 1.12 and 1.32 GeV.

t' region	total events in fit	S-wave events	D-wave events	S-wave events / D-wave events
all t'	4715	550 ± 90	390 ± 80	1.4 ± 0.4
$t' < .08$	1589	280 ± 70	70 ± 40	4.0 ± 2.6
$.08 < t' < .3$	1502	290 ± 70	130 ± 40	2.0 ± 0.8
$3. < t'$	1428	110 ± 60	210 ± 40	0.5 ± 0.3

TABLE V-4. Table V-4 shows the results of fitting the $K\pi$ mass plot for K^+N at 3.8 GeV/c for different t' cuts. In these fits the S-wave resonance is at 1.385 GeV with a width of .150 GeV, while the D-wave resonance is at 1.448 GeV with a width of .115 GeV.

with a width of .150 GeV while the D-wave resonance was at 1.448 GeV with a width of .115 GeV. From Table V-4, it is seen that there are roughly equal numbers of S-wave events in two regions, t' less than .08 $(GeV/c)^2$ and t' between .08 and .3 $(GeV/c)^2$, even though the total number of events in the fits are comparable. If pion exchange produced the 0^+ enhancement, it is expected that the number of S-wave events decrease as t' increased. The opposite effect is seen. However the meaning of these fits becomes uncertain when it is noticed that the ratio of S-wave events to D-wave events decreases as t' increases (see Table V-4). This means that the S-wave enhancement is produced more peripherally than the D-wave enhancement. Yet the density matrix elements for the D-wave enhancement suggest that pion exchange dominates.

A third explanation is that the enhancement in the K^+N data is produced by a secondary scattering involving the spectator proton and decay products of the K*(1420).[33] This argument procedes as follows: The K*(1420) is produced by pion exchange, so it is produced mainly in the forward direction. In addition the decay distribution for a 2^+ object produced by pion exchange favors decay either parallel or anti-parallel to the beam direction. One of the decay mesons then scatters off the spectator proton. After the scattering, the $K\pi$ system will be found to be produced less peripherally and the decay angular distribution will be less peaked at cosine equal $\pm$ 1. In the experiment at 3.8 GeV/c, the K*(1420) is produced near the edge of phase space, so the mass of the $K\pi$ system can only shift to lower $K\pi$ masses. Although this argument seems to explain the data at 3.8 GeV/c, it cannot explain the effect at 12.0 GeV/c where the K*(1420) is far from the edge of phase space. In addition

at higher energies the momentum of the K*(1420) will be large so that the K*(1420) will travel further from the interaction region before decaying; hence the probability of the scattering will decrease.

A fourth explanation is that in the K^+N reactions the enhancement is either completely or at least in part due to an interference between the resonant D-wave and other partial waves in the $K\pi$ system and/or background from other channels. Berger commented that uniterized models suggest that other channels may be very important in understanding the background.[34] As a result there is no reason to expect that the K^+N reactions and the K^+P reactions should exhibit the same structure if interference effects are playing an important role.

B. Mass Dependence of the Moments in the K*(1420) Region

The mass dependence of the moments with respect to the Y_{Lm} for the decay of the $K\pi$ system in the Jackson frame in the K*(1420) region are important for two reasons. First, they are important in the determination of the J^P quantum numbers of the enhancement. Second, a detailed examination of their behavior offers information about the importance of interference effects.

Figures V-3a-i show the mass dependence of the moments Y_{Lm} in the K*(1420) region for L less than 5 and m less than 2. All other moments were consistent with being zero in the K*(1420) region. The mass plot, Figure V-3a, shows the presence of a low mass shoulder; however none of the other moments have a fluctuation in this region.

Although it is possible for either a P-wave or a D-wave resonance to give an enhancement only in the mass plot, it seems rather unlikely

FIGURE V-3. Figure V-3 shows the mass dependence of the moments with respect to Y_{Lm} in the Jackson frame for the $K\pi$ system.

V-3a

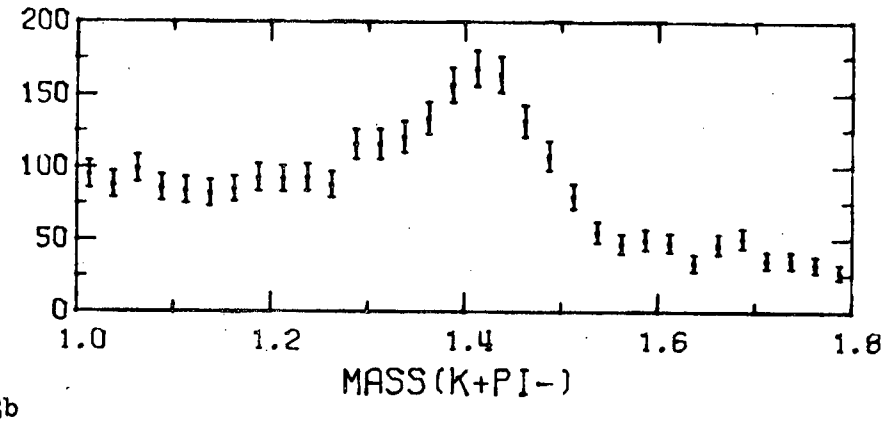
200
150
100
50
0
1.0
1.2
1.4
1.6
1.8
MASS(K+PI-)

V-3b

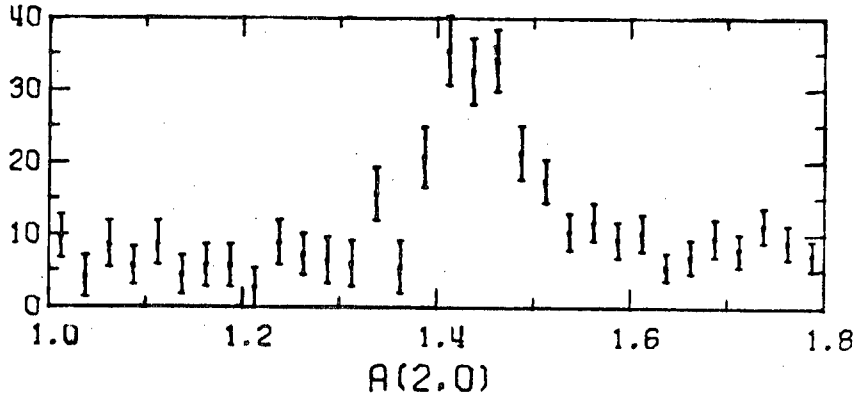
40
30
20
10
0
1.0
1.2
1.4
1.6
1.8
A(2,0)

V-3c

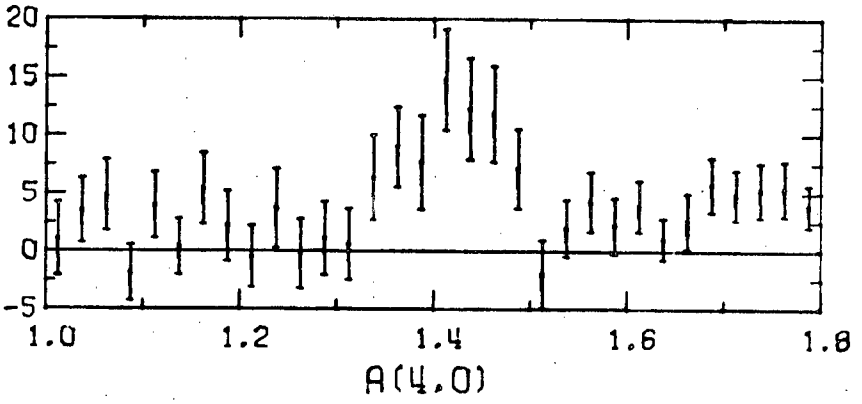
20
15
10
5
0
-5
1.0
1.2
1.4
1.6
1.8
A(4,0)

V-3d

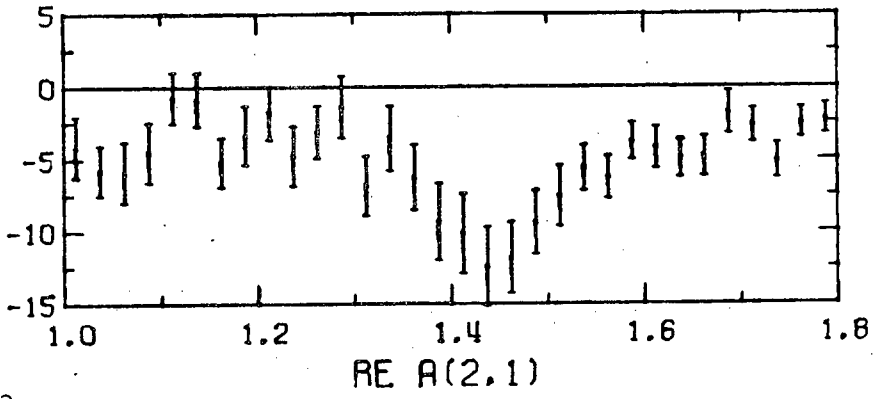
5
0
-5
-10
-15
1.0
1.2
1.4
1.6
1.8
RE A(2,1)

V-3e

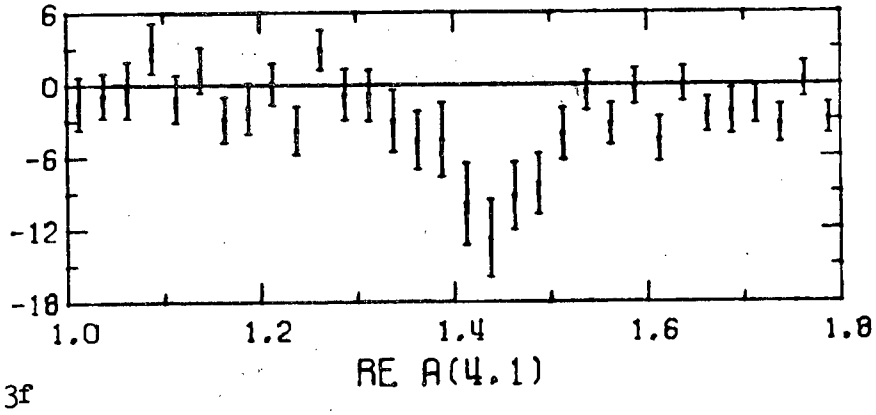
6
0
-6
-12
-18
1.0
1.2
1.4
1.6
1.8
RE A(4,1)

V-3f

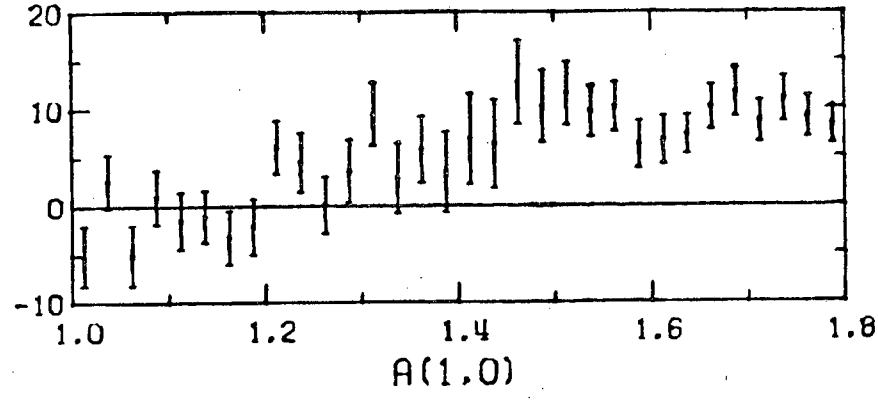
20
10
0
-10
1.0
1.2
1.4
1.6
1.8
A(1,0)

V-3g

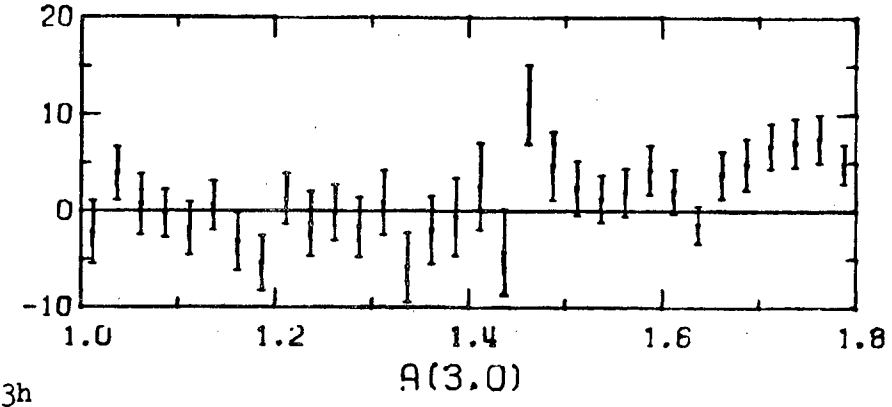
20
10
0
-10
1.0
1.2
1.4
1.6
1.8
A(3,0)

V-3h

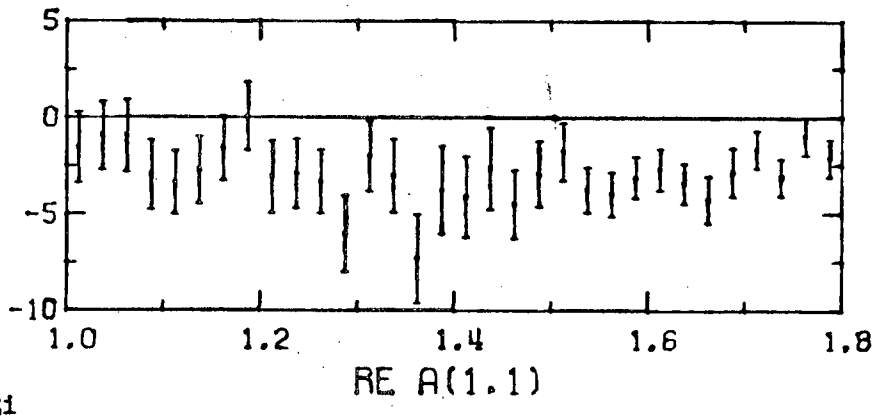
5
0
-5
-10
1.0
1.2
1.4
1.6
1.8
RE A(1,1)

V-3i

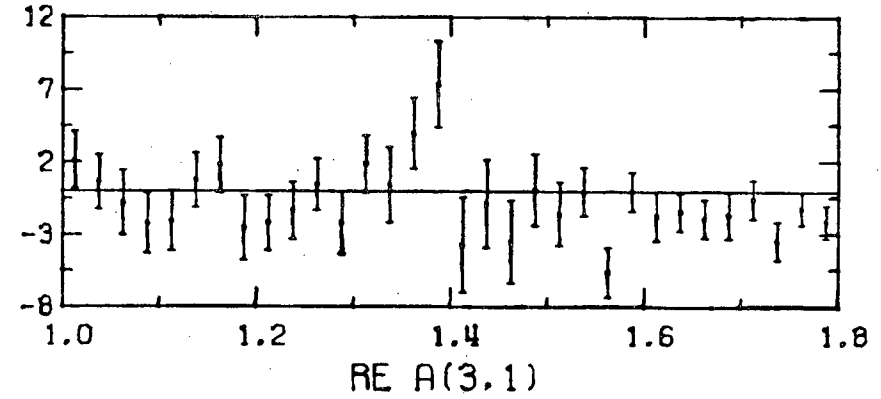
12
7
2
-3
-8
1.0
1.2
1.4
1.6
1.8
RE A(3,1)

since a special relationship among the density matrix elements would be required for that partial wave. For example assuming the shoulder is due to a P-wave resonance, this would require that equations V-4 be satisfied.

$$\rho_{00}^{PP} = \rho_{11}^{PP} \qquad \text{V-4a}$$

$$\text{Re } \rho_{10}^{PP} = 0 \qquad \text{V-4b}$$

By arguing that the K*(890) is produced by pion exchange and then looking at the t distribution, one concludes that pion exchange is probably important in the K*(1420) region. Since pion exchange only contributes to ρ_{00}^{PP}, this means a second exchange is responsible for the value of ρ_{11}^{PP}. However this second exchange must contribute in just such a way that equation V-4a is true. If only pion and vector exchange were present, Re ρ_{10}^{PP} would be zero. However absorption effects would generally produce non zero values for Re ρ_{10}^{PP}.

As a consequence of arguments of this type it appears as if the most likely J^P value for the enhancement is 0^+.

C. Results of Three Fits to the Moments

In Chapter IV a parameterization of the differential cross section in terms of the mass dependence of the moments was described and details of three fits were presented. In this section these fits will be used to predict the overall mass spectrum in the K*(1420) region as well as the effect of polar and equatorial cuts.

Before going into the detailed predictions of each of the fits to the moments, the following comments should be made.

1. When no cuts are made on the Jackson cosine, the mass plot is proportional to Y_{oo}; this is the only time the partial waves add incoherently.

2. When symmetric cuts are made on the Jackson cosine, the moment with respect to Y_{Lm} will contribute to the mass plot only if L is even and m is zero.

3. When symmetric cuts are made on the Jackson cosine, the only generalized density matrix elements, $R_{mm'}^{JJ'}$, contributing to the mass plot are those where m equals m' and the sum of J and J' is an even integer.

Figure V-4 compares the $K\pi$ data in the K*(1420) region with the results of the first fit of Chapter IV. From Table IV-2 it is seen that this fit has a .11 GeV wide S-wave resonance located at 1.37 GeV. The S-wave resonance sits on a large background, as can be seen from Figure IV-3. The fit agrees well with the overall mass plot, Figure V-4. The agreement of the fit with the mass plot in the equatorial region is not quite as good (see Figure V-4b). The agreement of the fit with the mass plot in the polar region is very good. Table IV-4 estimates that $(37.0 \pm 1.4)\%$ of the mass plot is due to the S-wave.

Figure V-5 compares the $K\pi$ data in the K*(1420) region with the results of the second fit of Chapter IV. From Table IV-5 it is seen that this fit has a .25 GeV wide S-wave resonance located at 1.45 GeV. From Figure IV-5 it is seen that the S-wave resonance interferes with a large S-wave background. The agreement of the fit with the overall mass plot, Figure V-5a, and the mass plot in the polar region, Figure V-5c, is very good. The agreement of the fit with the mass plot in the

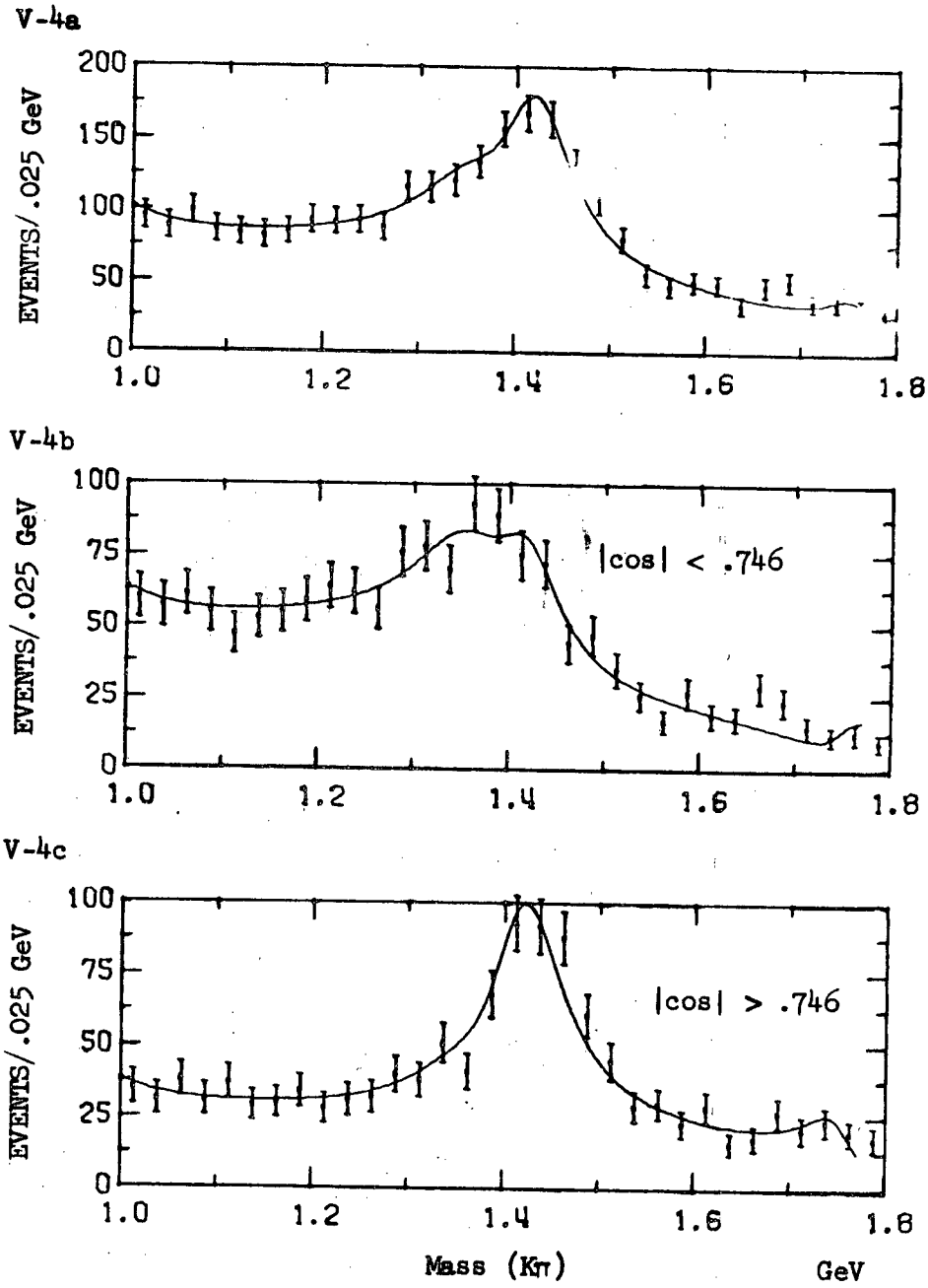

FIGURE V-4. Figure V-4a compares the results of the fit of Section IV-C1 with the Kπ mass spectrum in the K^+N reaction at 3.8 GeV/c. Figures V-4b and V-4c compare the equatorial and polar regions with the results of this fit.

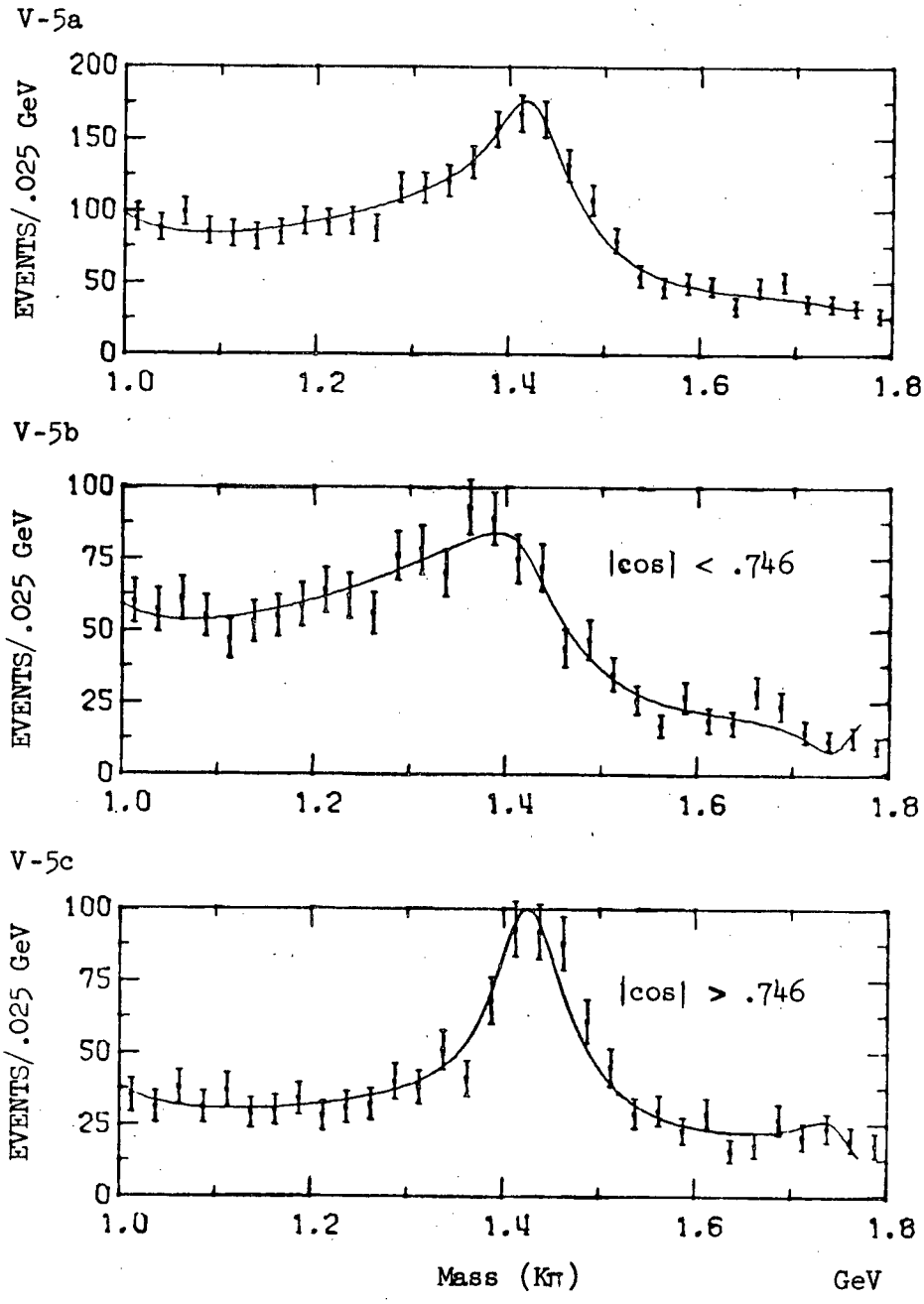

FIGURE V-5. Figure V-5a compares the results of the fit of Section IV-C2 with the Kπ mass spectrum in the K^+N reaction at 3.8 GeV/c. Figures V-5b and V-5c compare the equatorial and polar regions with the results of this fit.

equatorial region is fair. Table IV-7 estimates that (54.4 ± 2.2)% of the mass plot is due to the S-wave.

The peripheralized phase space used for the second fit may be easily modified for use in reaction V-3. This modification amounts to replacing the integral of $t/(\mu^2-t^2)^2$ in equation IV-18 with the integral of $1/(\mu^2-t^2)^2$ and changing the mass of m_d from a nucleon mass to the mass of the $\Delta(1238)$. Figure V-6 compares the combined $K\pi$ data in the K*(1420) region for reaction V-3 at 5.0, 5.5 and 7.3 GeV/c with the predictions of the second fit after changing phase space. The prediction agrees fairly well with the overall mass plot, Figure V-6a, and the mass plot in the polar region, Figure V-6c. The fit reproduces the abrupt fall off of the mass plot in the equatorial region. The agreement between the fit for reaction V-1 and the data for reaction V-3 suggest that reactions V-1 and V-3 are very closely related inspite of differences in absorption and differences in the contributions from non pion exchanges.

Figure V-7 compares the $K\pi$ data in the K*(1420) region of reaction V-1 with the results of the third fit of Chapter IV. From Figure IV-7 it is seen that the S-wave has a broad enhancement centered at 1.28 GeV. In Figure V-7a, it is seen that the fit reproduces the overall mass dependence of the mass plot, although it is somewhat low in the region of the shoulder on the low mass side of the K*(1420). The fit in the equatorial region reproduces the general features of the data. The interference between the S and D-waves is partly responsible for filling in the region between 1.28 GeV where the S-wave peaks and 1.42 GeV where the D-wave peaks. The agreement between the fit and the data in the

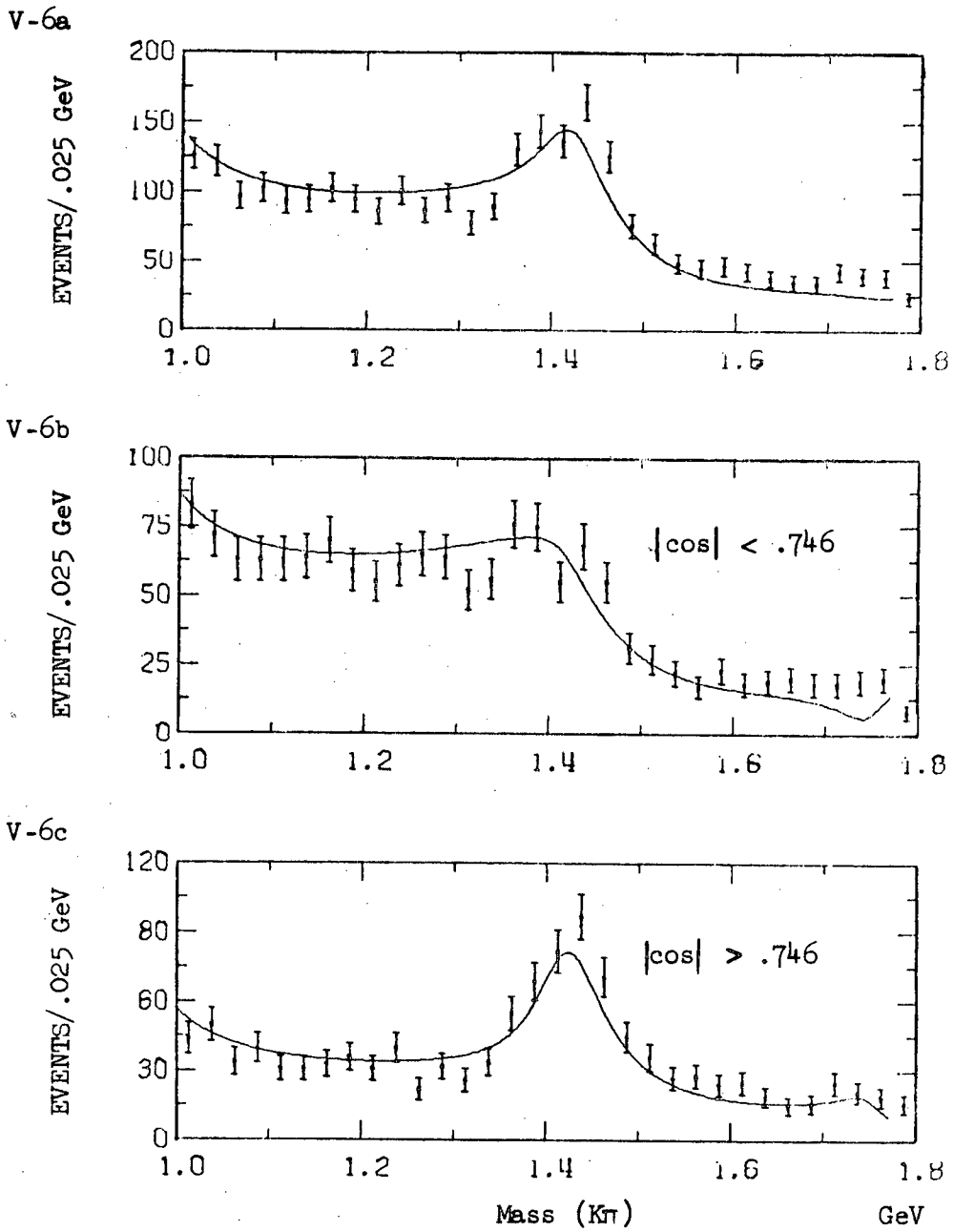

FIGURE V-6. Figure V-6a compares the prediction of the fit of Section IV-C2 after modifying phase space with the combined Kπ mass spectrum for the K^+P reactions at 5.0, 5.5 and 7.3 GeV/c. Figures V-6a and V-6c compare the equatorial and polar regions with the predictions of the fit.

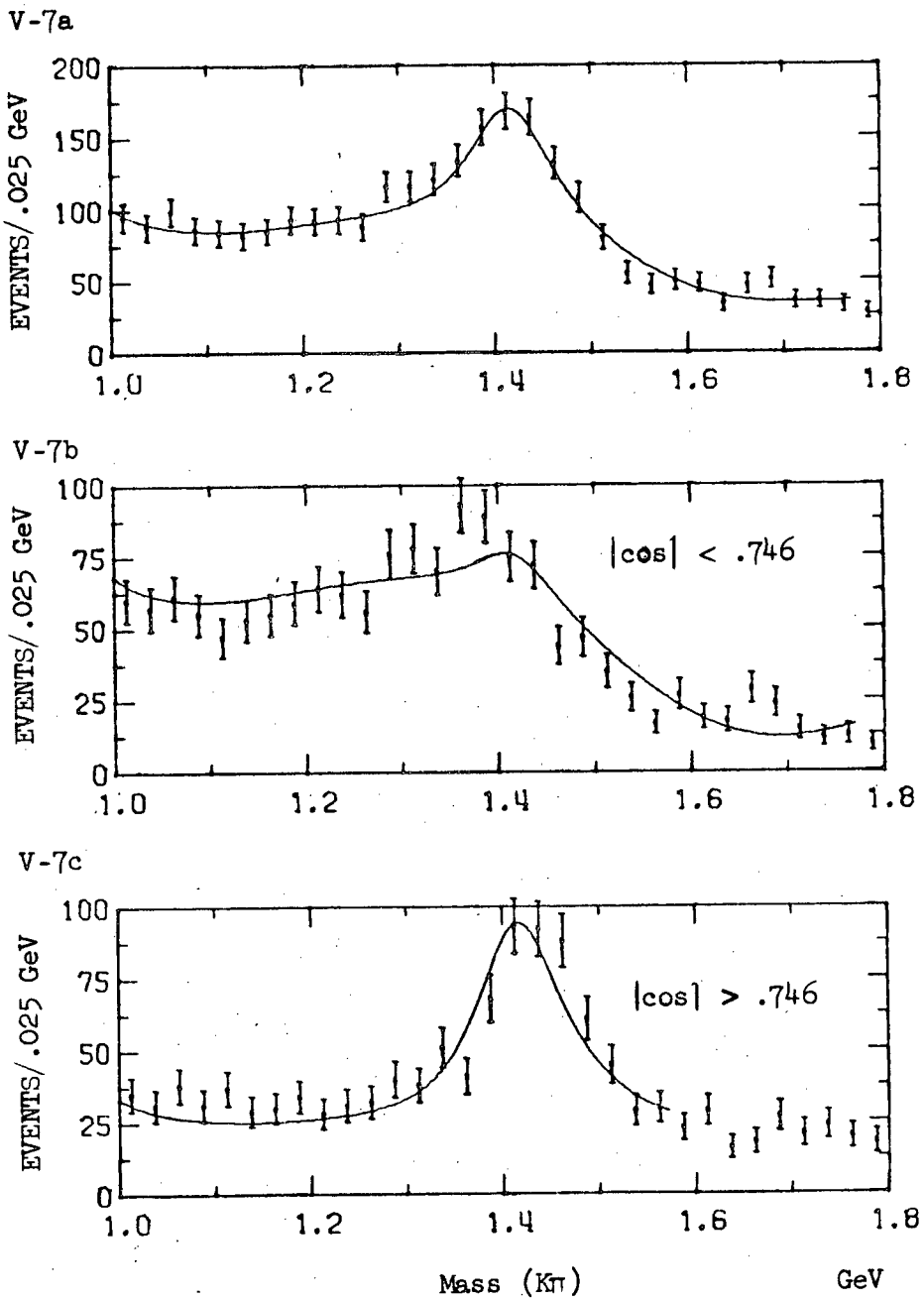

FIGURE V-7. Figure V-7a compares the results of the fit of Section IV-C3 with the Kπ mass spectrum in the K^+N reaction at 3.8 GeV/c. Figures V-7b and V-7c compare the equatorial and polar regions with the results of this fit.

polar region is good. Table IV-10 estimates that (44.6 ± 1.8)% of the mass plot is due to the S-wave.

Figure V-8 compares the combined $K\pi$ data in the K*(1420) region of reaction V-3 at 5.0, 5.5 and 7.3 GeV/c with the predictions of the third fit after changing phase space. The agreement with the data is similar to the agreement found between the data and the second fit.

D. Summary and Conclusions

The $K\pi$ system in the region of the K*(1420) was examined for the effect reported by Firestone et al. in reaction V-1 at 12.0 GeV/c.[4] The effect was seen in the data for reaction V-1 at 3.8 GeV/c. The interpretation of the effect at 3.8 GeV/c is clouded by a possible interpretation involving a secondary scattering between the spectator proton and the decay products of the K*(1420).

An examination of the moments suggests that the effect may be due to either an enhancement in the S-wave or an interference between the S and D-waves. Fits to the moments indicate that between 35% and 55% of the mass plot in the region 1.34 to 1.54 GeV is due to the S-wave. The fits also indicate the primary difference between reactions V-1 and V-3 may be attributed to a large extent to differences in peripheralized phase space.

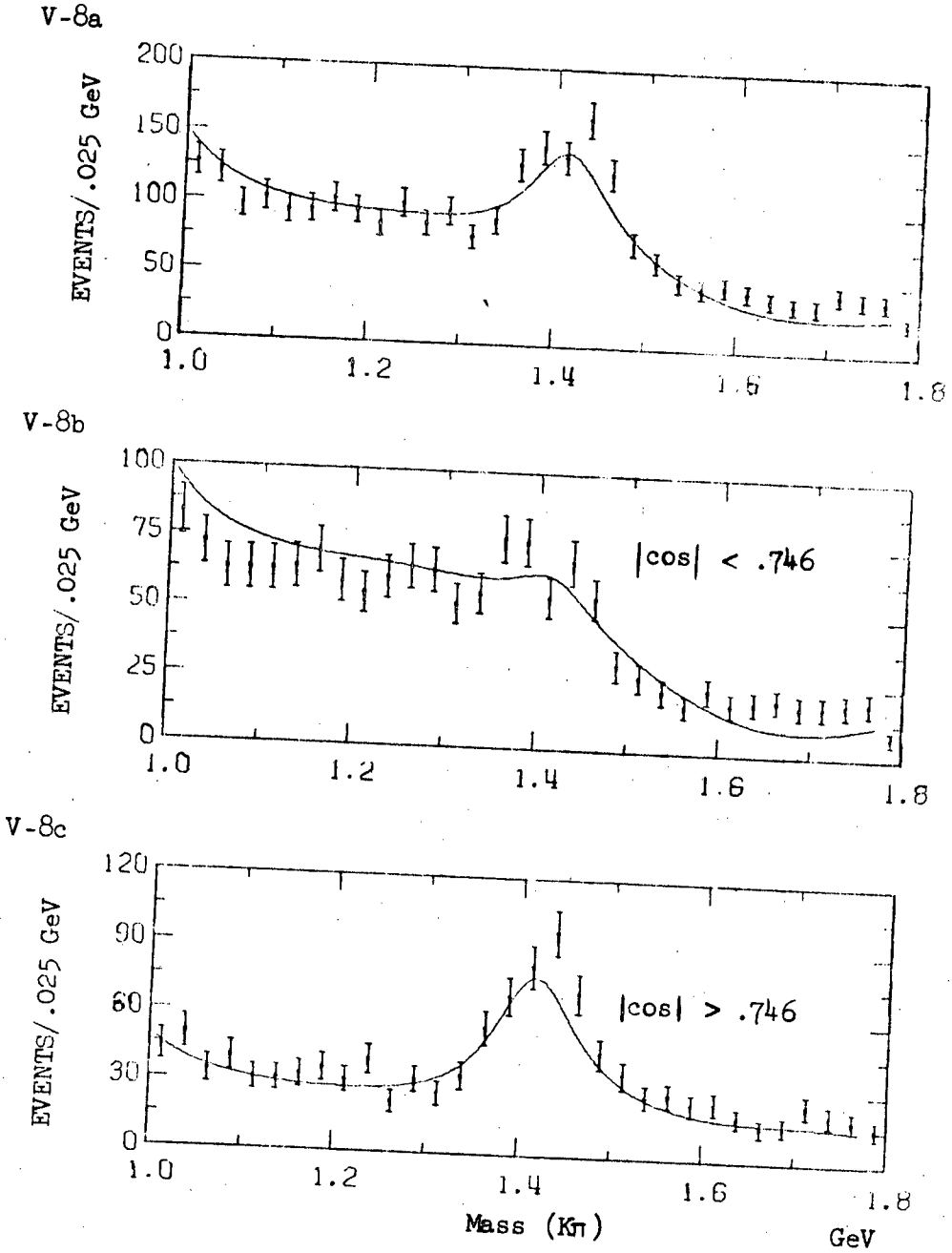

FIGURE V-8. Figure V-8a compares the predictions of the fit of Section IV-C3 after modifying phase space with the combined $K\pi$ mass spectrum for the K^+P reactions at 5.0, 5.5 and 7.3 GeV/c. Figures V-8b and V-8c compare the equatorial and polar regions with the predictions of the fit.

VI. K*(890) REGION

A. Introduction

Production of the K*(890) is the dominant feature of reaction VI-1.

$$K^+N \rightarrow K^+\pi^-P \qquad \text{VI-1}$$

Table VI-1 shows the mass and width of the K*(890) for the two fits described in Sections IV-C1 (Table IV-2) and C2 (Table IV-5) along with the mass and width listed by the Particle Data Group.[35] The mass of the K*(890) is somewhat higher than the mass given by the Particle Data Group while the width is somewhat narrower. These differences are attributed to the exact details of the fitting procedure. Some of the major differences are listed below:

1. The fits use all of the moments rather than just the mass plot.
2. The Breit-Wigner was allowed to interfere coherently with a background.
3. The Breit-Wigner was multiplied by a peripheralized phase space.
4. The Breit-Wigner used an energy dependent width as formulated by Jackson.[22]
5. The fits used a rather coarse mass binning of .02 GeV.
6. The mass resolution of the experiment was not folded into the mass dependence of the moments.

Table VI-2 compares the results of the three fits of Section IV-C in the K*(890) region which is defined to be .84 to .94 GeV. Table VI-2 shows the fraction of the events due to S-wave and P-wave from Tables IV-4, IV-7 and IV-10, the density matrix elements ρ_{00}^{SS}, ρ_{00}^{PP}, ρ_{11}^{PP}, and

	fit of section IV-C1.	fit of section IV-C2	nominal values from Particle Data Group[35]
M_o (GeV)	.8959 ± .0009	.8962 ± .0008	.89255 ± .00045
Γ (GeV)	.046 ± .002	.049 ± .002	.053 ± .0011

TABLE VI-1. Table VI-1 shows the mass and width of the K*(890) for two fits described in section IV-C1 and IV-C2 along with the mass and width from the Particle Data Group.[35] Differences between the fits and the mass and width from the Particle Data Group are attributed to the exact details of the fitting procedure (see text).

Re ρ_{10}^{PP}, and cross section times the density matrix elements. As explained in Section IV-C, the moment Y_{22} and hence the density matrix element ρ_{1-1}^{PP} was not fit because no significant structure was seen in the region of the K*(890) for this moment. The interference density matrix elements Re ρ_{00}^{PS} and Re ρ_{10}^{PS} were also fit. The mass dependence of these matrix elements, however, is of such a nature that their value is very dependent upon the low mass end point (see Figure IV-2h, k or IV-4h, k or IV-7h, k); for this reason the value of these density matrix elements was not included in Table VI-2.

Before leaving the topic of these interference density matrix elements, it is interesting to point out that the interference density matrix element as well as the product of the mass dependences are complex functions (see equation IV-13); hence the imaginary part of the interference

VI-2a

fit	ρ_{00}^{SS}	fraction of events in P-wave	ρ_{00}^{PP}	ρ_{11}^{PP}	Re ρ_{10}^{PP}
C1	.127±.005	.87±.04	.51±.02	.183±.014	-.183±.013
C2	.104±.004	.90±.04	.52±.03	.186±.015	-.191±.013
C3	.128±.005	.87±.04	.56±.02	.157±.013	-.197±.012

VI-2b

The cross section seen in the K*(890) region (.84-.94 GeV) is (450±30)μb.

fit	$\sigma\rho_{00}^{SS}$ (μb)	cross section for P-wave	$\sigma\rho_{00}^{PP}$ (μb)	$\sigma\rho_{11}^{PP}$ (μb)	σReρ_{10}^{PP} (μb)
C1	57±5	400±30	230±20	83±9	-83±6
C2	47±4	410±30	240±20	84±9	-87±6
C3	58±4	400±30	250±20	71±8	-89±5

TABLE VI-2. Table VI-2a shows the density matrix elements ρ_{00}^{SS}, ρ_{00}^{PP}, ρ_{11}^{PP} and Re ρ_{10}^{PP} in the Jackson frame and the fraction of the total events in the P-wave according to the fits of sections IV-C1, IV-C2 and IV-C3 in the K*(890) region. Table VI-2b shows the density matrix elements times the cross section, $\sigma\rho_{00}^{SS}$, $\sigma\rho_{00}^{PP}$, $\sigma\rho_{11}^{PP}$, σRe ρ_{10}^{PP}, in the Jackson frame and the cross section for the P-wave according to the fits C1, C2, and C3 of Chapter IV in the K*(890) region. The K*(890) region is defined to be between .84 and .94 GeV.

density matrix element will contribute to the real part of the moment. If it is known that the imaginary part of the interference density matrix element is zero, then it is possible to use the known phase dependence of the P-wave to predict the phase of the S-wave at the point where an interference moment passes through zero. Note however that if the interference density matrix element is imaginary and if it were assumed to be real, then the resulting S-wave phase as estimated from the zero of the moment would be off by 90°.

From Table VI-2, it is seen that about (88 ± 4)% of the events in the K*(890) region are due to the resonant P-wave; the S-wave accounts for the rest of the events. The fits of Section IV-C indicate that the contribution of the D and F-waves in the K*(890) region is negligible. The fits indicate that ρ_{00}^{PP} is about (.53 ± .02). This means that (60 ± 3)% of the P-wave cross section comes from $\sigma\rho_{00}^{PP}$ and indicates that pion exchange is the dominant production mechanism for the P-wave. In addition pion exchange is the dominant production mechanism for the S-wave since vector exchange without absorption does not contribute to 0^+ production. Hence pion exchange is responsible for about (72 ± 4)% of the cross section in the K*(890) region. The non zero value of ρ_{11}^{PP} indicates the presence of either other exchange mechanisms or absorption effects. The non zero value of Re ρ_{10}^{PP} indicates the presence of either axial vector exchange or absorption effects since pion exchange and vector exchange together without absorption do not contribute to Re ρ_{10}^{PP}.

Figure VI-1 shows the differential cross section, $d\sigma/dt$, for the K*(890) region. The dip in the forward direction is primarily due to the shape of the kinematic boundary of the t versus $m_{K\pi}$ plot. In addition

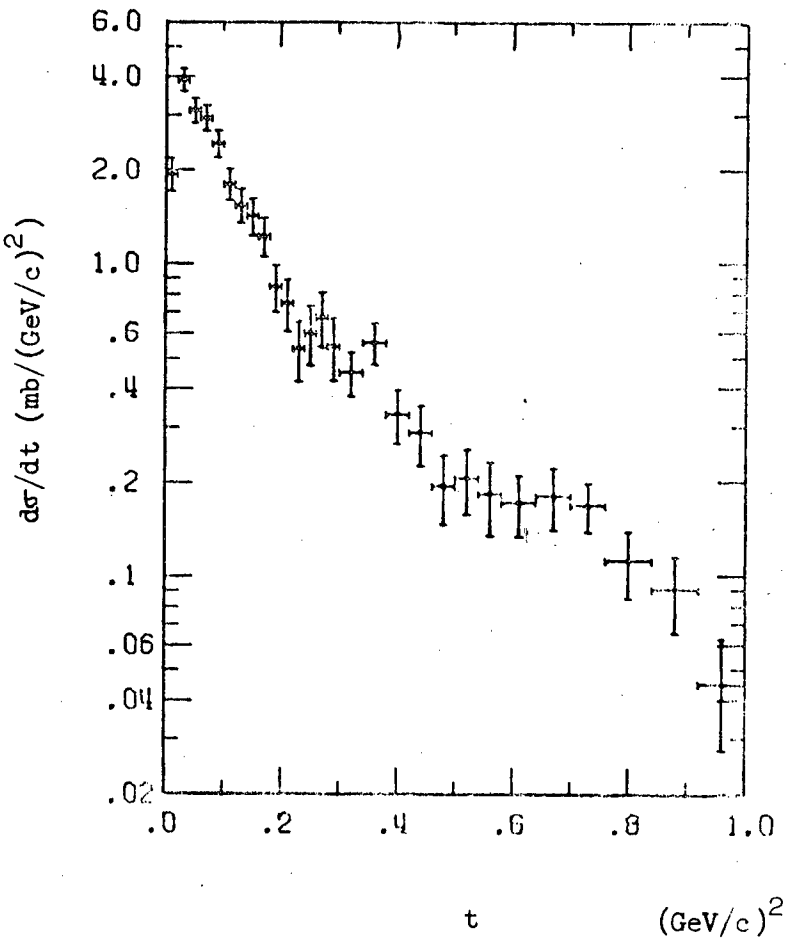

FIGURE VI-1. Figure VI-1 shows the differential cross section for all events in the $K^{*0}(890)$ region (.84 - .94 GeV). The differential cross section has been corrected for unseen neutral decay modes.

no corrections have been made for the effect of the Pauli Exclusion Principle (see Section II-I).

The slope of the reaction for t between .02 and .20 $(GeV/c)^2$ was fit and found to be $(8.9 \pm .8)/(GeV/c)^2$ in the K*(890) region (see Table III-1). The differential cross section appears to have a change in slope for t about .2 $(GeV/c)^2$. Lissauer sees a similar break in the slope for reaction VI-1 at 12.0 GeV/c.[36] However the slope is $(20 \pm 2)/(GeV/c)^2$ and the break occurs for t about .1 $(GeV/c)^2$. A similar behavior for $d\sigma/dt$ in $K^{*0}\Delta^{++}$ production in K^+P data along with a study of the density matrix elements as a function of t in the K^+P data has led O'Halloran to suggest that the change in slope and the t value at which the break occurs may be evidence for shrinkage of the pion trajectory.[37]

B. t Distribution for K*(890) Production

The method described in Section IV-C1 was used to study the t dependence of the density matrix elements ρ_{00}^{SS}, ρ_{00}^{PP}, Re ρ_{10}^{PP} and ρ_{1-1}^{PP} in the Jackson frame. Table VI-3 gives the numeric values of the density matrix elements and Figure VI-2 displays the t dependence of the density matrix elements. Table VI-4 gives the numeric values of the density matrix element times the differential cross section $d\sigma/dt$. Figure VI-3 displays the t dependence of $\rho_{00}^{SS}\frac{d\sigma}{dt}$, $\rho_{00}^{PP}\frac{d\sigma}{dt}$, $\rho_{11}^{PP}\frac{d\sigma}{dt}$ and $-(\text{Re }\rho_{10}^{PP})\frac{d\sigma}{dt}$ on a log plot.

The fitting procedure is as follows: The $K\pi$ mass spectrum was subjected to a number of t cuts which were selected so that when the mass dependence of the data was plotted in 0.1 GeV bins starting at .74 GeV, there would be at least 20 events in each of the first four bins. This

t region $(GeV/c)^2$	ρ_{00}^{SS}	ρ_{00}^{PP}	ρ_{11}^{PP}	Re ρ_{10}^{PP}	ρ_{1-1}^{PP}
.00-.02	.14±.04	.72±.12	.07±.07	-.08±.06	.02±.06
.02-.04	.20±.03	.54±.07	.13±.04	-.16±.04	.02±.04
.04-.06	.14±.02	.66±.08	.10±.05	-.23±.04	-.08±.04
.06-.08	.14±.03	.63±.08	.12±.05	-.19±.04	.06±.04
.08-.10	.05±.02	.69±.09	.13±.05	-.25±.04	-.06±.05
.10-.14	.10±.02	.66±.09	.12±.05	-.24±.04	-.03±.04
.14-.18	.15±.03	.55±.08	.15±.05	-.28±.05	-.14±.05
.18-.24	.16±.03	.51±.09	.16±.06	-.20±.05	-.04±.06
.24-.32	.12±.03	.47±.09	.20±.06	-.19±.05	-.05±.06
.32-.44	.10±.02	.30±.08	.30±.05	-.17±.04	.08±.06

TABLE VI-3. Table VI-3 shows the results of the fits to the S and P-wave density matrix elements for the Jackson frame in the K*(890) region (.84-.94 GeV) as a function of t.

FIGURE VI-2. Figure VI-2 shows the results of the fits to the S and P-wave density matrix elements for the Jackson frame in the K*(890) region (.84 - .94 GeV) as a function of t.

VI-2a

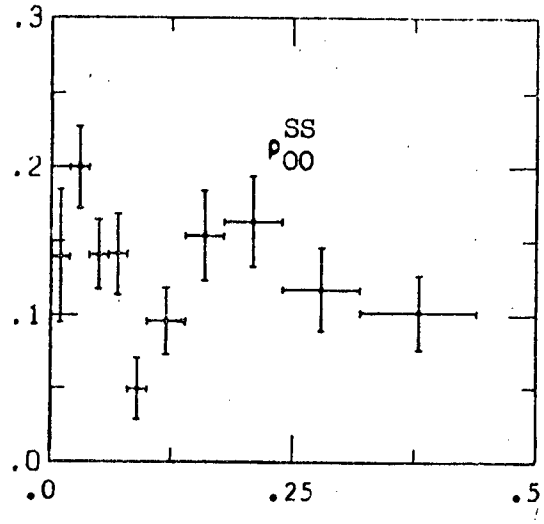

VI-2b

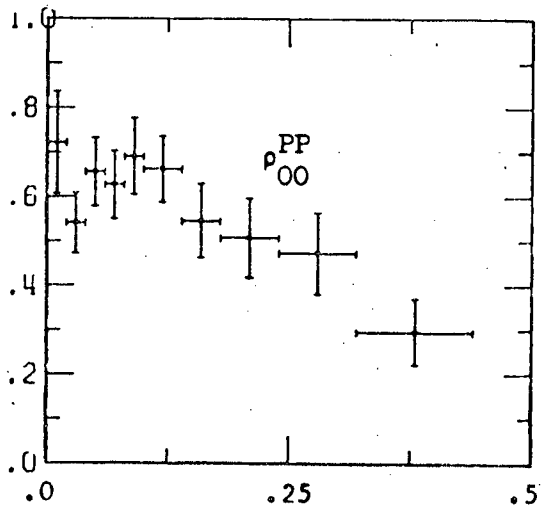

VI-2c

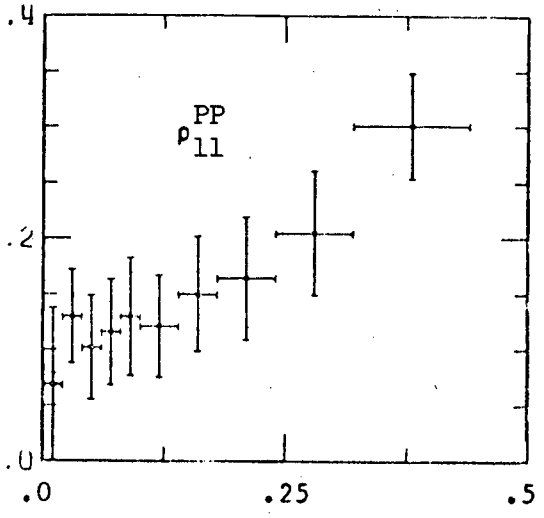

VI-2d

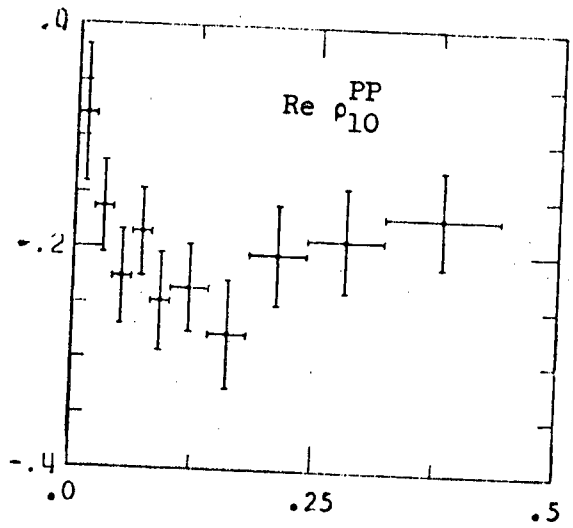

VI-2e

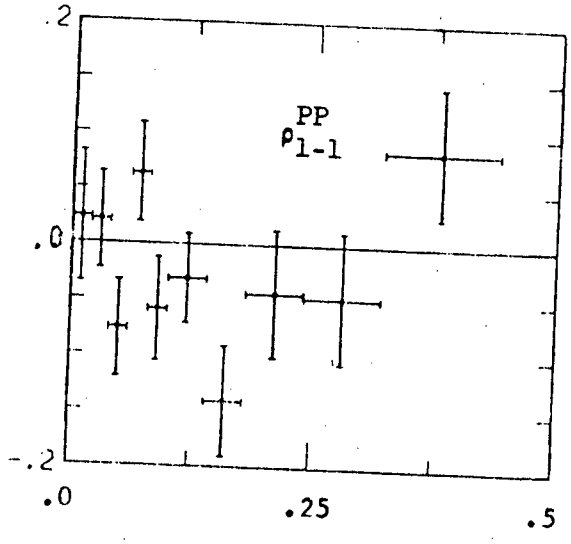

t region $(GeV/c)^2$	SS $\rho_{00}\frac{d\sigma}{dt}$ (mb)	PP $\rho_{00}\frac{d\sigma}{dt}$ (mb)	PP $\rho_{11}\frac{d\sigma}{dt}$ (mb)	PP $Re\rho_{10}\frac{d\sigma}{dt}$ (mb)	PP $\rho_{1-1}\frac{d\sigma}{dt}$ (mb)
.00-.02	.18±.06	0.93±.15	.09±.09	-.10±.08	0.03±.08
.02-.04	.52±.07	1.40±.18	.34±.11	-.42±.11	0.05±.11
.04-.06	.29±.05	1.36±.16	.21±.10	-.47±.09	-.16±.09
.06-.08	.28±.05	1.23±.15	.23±.09	-.36±.08	0.13±.09
.08-.10	.08±.03	1.12±.14	.21±.08	-.40±.07	-.10±.08
.10-.14	.11±.02	0.74±.08	.14±.05	-.26±.04	-.03±.04
.14-.18	.14±.03	0.48±.07	.13±.05	-.24±.04	-.12±.04
.18-.24	.08±.01	0.24±.04	.08±.03	-.10±.02	-.02±.03
.24-.32	.04±.01	0.18±.04	.08±.02	-.07±.02	-.02±.02
.32-.44	.03±.01	0.08±.02	.08±.01	-.05±.01	0.02±.02

TABLE VI-4. Table VI-4 shows the results of the fits to the S and P-wave density matrix elements in the Jackson frame times the differential cross section in the K*(890) region (.84-.94 GeV).

FIGURE VI-3. Figure VI-3 shows the results of the fits to the S and P-wave density matrix elements in the Jackson frame times the differential cross section in the K*(890) region (.84 - .94 GeV).

VI-3a

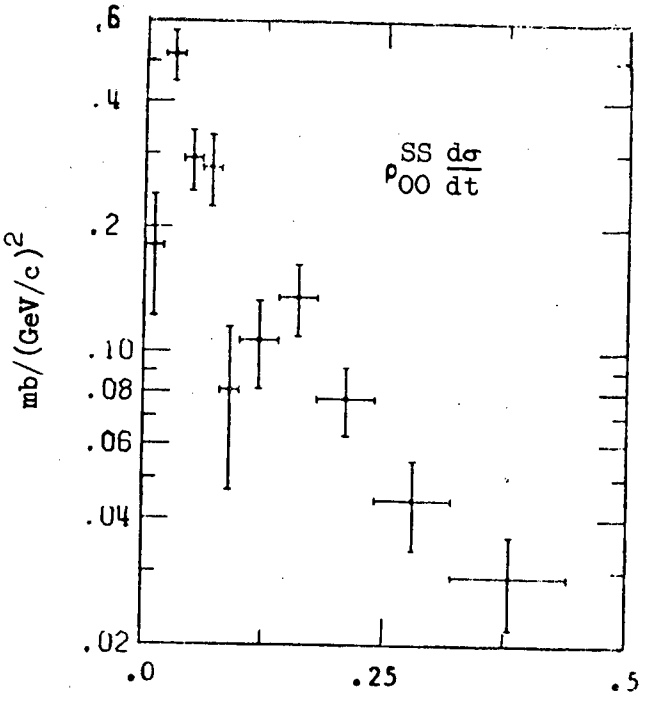
.6
.4
.2
.10
.08
.06
.04
.02
.0
.25
.5
$\rho_{00}^{SS} \frac{d\sigma}{dt}$
mb/(GeV/c)^2

VI-3b

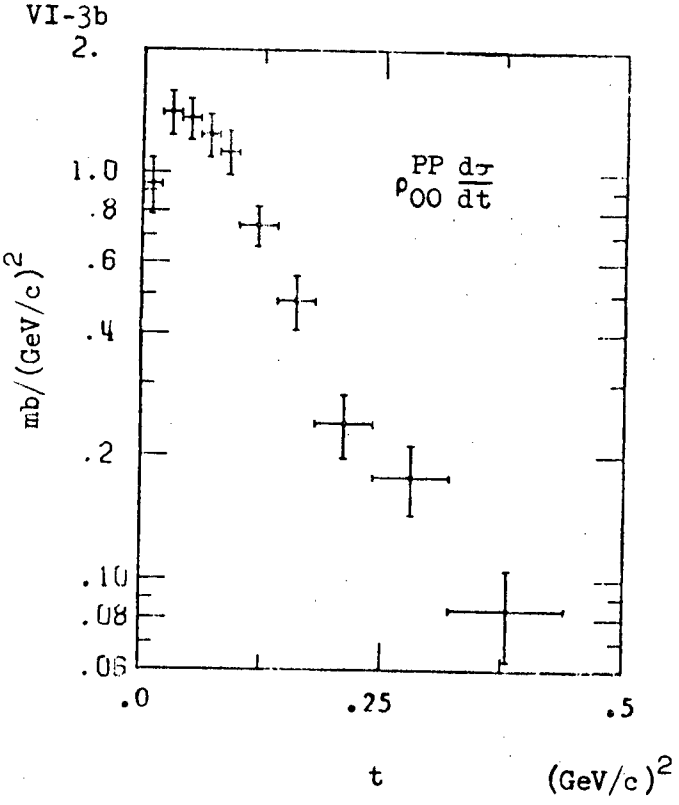
2.
1.0
.8
.6
.4
.2
.10
.08
.06
.0
.25
.5
$\rho_{00}^{PP} \frac{d\sigma}{dt}$
mb/(GeV/c)^2
t
(GeV/c)^2

VI-3c

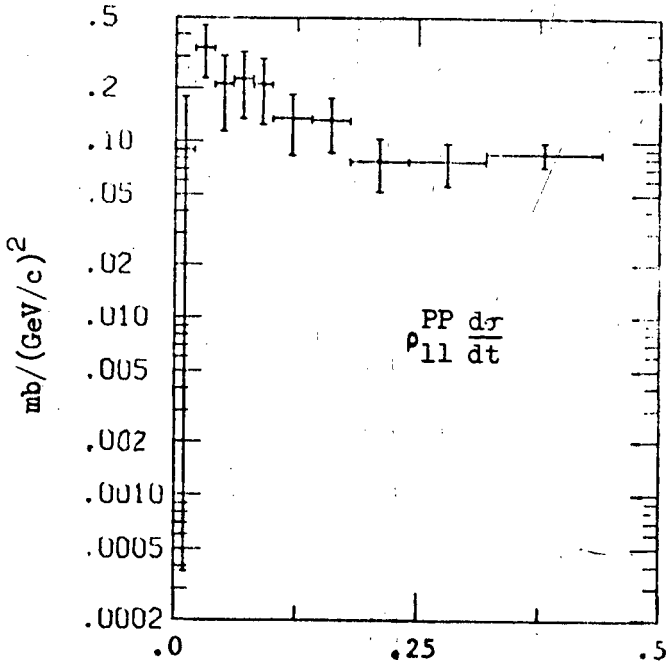
.5
.2
.10
.05
.02
.010
.005
.002
.0010
.0005
.0002
mb/(GeV/c)^2
$\rho_{11}^{PP} \frac{d\sigma}{dt}$
.0
.25
.5

VI-3d

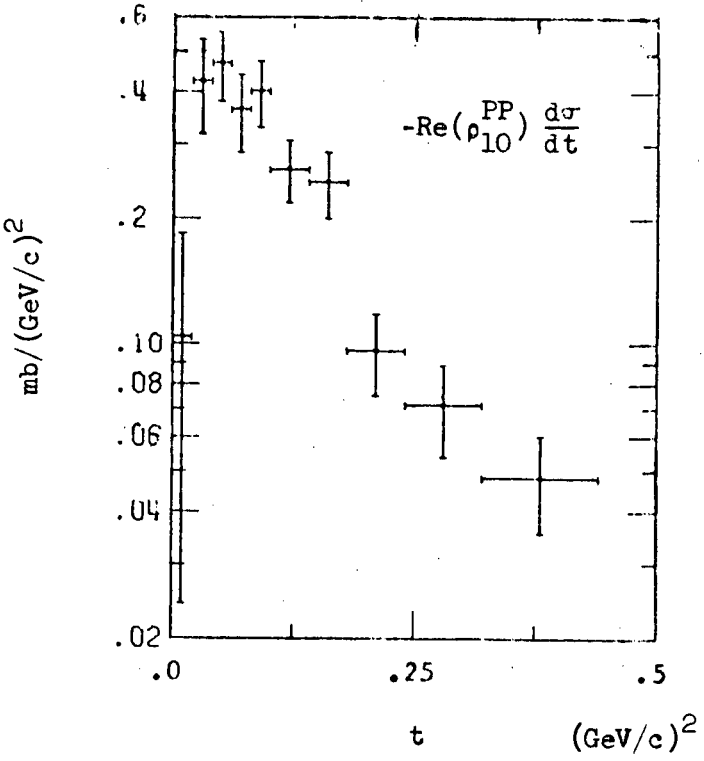
.6
.4
.2
.10
.08
.06
.04
.02
mb/(GeV/c)^2
$-\mathrm{Re}(\rho_{10}^{PP}) \frac{d\sigma}{dt}$
.0
.25
.5
t
(GeV/c)^2

condition was met for all t cuts except for the first for t between .00 and .02; in this case only the first three bins had at least 20 events owing to the shape of the kinematic boundary of the t versus $m_{K\pi}$ plot for reaction VI-1 at 3.8 GeV/c. The requirement that there be at least 20 events in a bin was necessary to hold down the statistical fluctuations in the moments with respect to Y_{Lm} in the Jackson frame for L equal 0 and 2, and m equal 0, 1, and 2. Phase space was obtained by fitting a polynomial, $P_n(m-m_c)$ from equation IV-17; β_J was set to zero in the equation and the sum ranged over all Breit-Wigner functions which could reasonably contribute in the mass region allowed by the t cut. In the fitting of the polynomials, the mass plot was binned in .05 GeV bins starting at .64 GeV. Each of the moments was fit using 4 mass bins between .74 and 1.14 GeV and inserting a background term in each moment. In the fit to Y_{00}, the mass plot, the background was R(00;00), the density matrix element for S-wave. In the moments Y_{2m}, the background term was I(20;m0); this density matrix element was chosen since the fits in section IV-C indicated that these matrix elements were large and smoothly varying in the K*(890) region. Actually any other density matrix element with a smoothly varying mass dependence would have worked just as well in the background subtraction. The density matrix elements, Re $\rho_{mm'}^{JJ'}$, were obtained from equation VI-2 which gives the relation between the density matrix element in the mass region M_1 to M_2 and the parameters of the fit.

$$\mathrm{Re}\rho^{JJ'}_{mm'} = C\left\{R(JJ';mm')\int_{M_1}^{M_2}\mathrm{Re}[B_J B^*_{J'}]dM + I(JJ';mm')\int_{M_1}^{M_2}\mathrm{Im}[B_J B^*_{J'}]dM\right\}(2-\delta_{\mu o})$$

$$\frac{1}{C} = \sum_{J,m} R(JJ;mm)\,(2-\delta_{mo})\int_{M_1}^{M_2}|B_J(M)|^2\,dM \qquad \text{VI-2}$$

$\delta_{mo} = 1$ if $m = 0$
$= 0$ if $m \neq 0$
$\mu = m - m'$

The constant C is defined so that the trace condition will be satisfied. The errors on Re $\rho^{JJ'}_{mm'}$ are directly related to the errors on $R(JJ';mm')$ and $I(JJ';mm')$, and the errors on R and I are known from the least squares fitting program. The density matrix elements times the differential cross section was obtained by normalizing to the cross section seen for the t cut in the mass region .84 to .94 GeV. The overall error on the total cross section has not been folded into the error on Re $\rho^{JJ'}_{mm'}\frac{d\sigma}{dt}$ since it is small in comparison with other errors.

The method described is equivalent to a background subtraction in each moment. In the mass plot the background is assumed to be entirely due to S-wave. This assumption is probably very good because the fits of Section IV-C indicate that the contribution of D and F-waves to the mass plot is very small.

From Figure VI-2a, ρ^{SS}_{00} is seen to dip around 0.1 $(\mathrm{GeV/c})^2$. This dip appears to be a real feature of the data and not a peculiarity of the fitting procedure.

If the dip in ρ^{SS}_{00} is real, then Re ρ^{PS}_{00} and Re ρ^{PS}_{10} should also show structure in the same t region. Unfortunately these density matrix elements were not well determined by the fitting procedure. In particular

the mass bins were chosen so that the K*(890) signal would peak in the center of the second bin. The real and imaginary parts of the product of the mass dependences, $B_P B_S^*$, peak at the edges of the bin. As a result the fit values for the generalized density matrix elements R_{00}^{PS}, I_{00}^{PS}, R_{10}^{PS} and I_{10}^{PS} were poorly determined and often badly violated the equations of constraint (see equation IV-14).

In Chapter 7 the t dependence of the interference density matrix elements is studied further using the method of moments. From Figure VII-3d it can be seen that Re ρ_{00}^{PS} for t between .08 and .10 $(GeV/c)^2$ is .31 ± .05 while Re_{00}^{PS} in neighboring t regions averages to .15 ± .06. However Re ρ_{10}^{PS} shows no real structure (see Figure VII-3e).

In summary it appears as if the dip in ρ_{00}^{SS} is a real feature of the data and that there may be structure in Re ρ_{00}^{PS} for the same t region. There is no real structure in Re ρ_{10}^{PS}.

C. One Pion Exchange Model With Absorption (OPEA)

The one pion exchange model with absorption (OPEA)[5] has been shown to give fairly good agreement for the shape and energy dependence of the differential cross section for reaction VI-3 at 3.0 and 9.0 GeV/c.[23]

$$K^+N \rightarrow K^{*o}(890)\ P \qquad \text{VI-3}$$

It has also been shown to give good agreement with the differential cross section and density matrix elements for reaction VI-4 at 3.9 and 4.6 GeV/c for t between t_{min} and .25 $(GeV/c)^2$.[7]

$$K^- P \rightarrow \overline{K^{*o}}(890)\, N \qquad \text{VI-3}$$

Equations VI-5 give the relations between the parameters of the OPEA model and quantities known from other data.[5]

$$C_5 = \frac{g^2_{K^{*o}K^+\pi^-}}{4\pi} \; \frac{g^2_{NP\pi}}{4\pi}$$

$$\frac{g^2}{4\pi} = K^{*o}K^+\pi^- \text{ coupling constant}$$

$$= \frac{2}{3} \frac{\Gamma(K^{*o} \rightarrow K^+\pi^-)}{P^3_{K,K^*}}$$

$$= 1.0\ (\text{GeV})^{-2} \qquad \text{VI-5}$$

$$\frac{g^2_{NP\pi}}{4\pi} = NP\pi \text{ coupling constant}$$

$$= 29.2\ (\text{GeV})^{-2}$$

$$C_1 = \frac{\sigma_{T1}}{4\pi A_1}$$

$$\gamma_1 = 1/(2q_1^2 A_1)$$

σ_{T_1} = total cross section for K^+N at a cm energy of 2.88 GeV.

A_1 = slope of the forward elastic scattering diffraction peak for K^+N K^+N at a cm energy of 2.88 GeV.

q_1 = incident cm momentum for $K^+N \rightarrow K^+N$ at cm energy of 2.88 GeV.

$$C_2 = \frac{\sigma_{T2}}{4\pi A_2}$$

$$\gamma_2 = 1/(2q_2^2 A_2)$$

σ_{T2} = total cross section for $K^{*o}P$ at a cm energy of 2.88 GeV.

A_2 = slope of forward elastic scattering diffraction peak for $K^{*o}P \rightarrow K^{*o}P$ at a cm energy of 2.88 GeV.

q_2 = incident cm momentum for $K^{*o}P \rightarrow K^{*o}P$ at a cm energy of 2.88 GeV.

Since no data on K^+N elastic scattering is available, the absorption parameters C_1 and γ_1 were calculated using the K^+N total cross section and approximating the K^+N elastic cross section as being equal to the K^+P elastic cross section at the same energy.[38] For the final state no information is available to calculate C_2 and γ_2. For this reason γ_2 is usually set equal to $.75\gamma_1$ and C_2 is set equal to 1.[5] Equations VI-6 show the calculated values for the OPEA parameters.

$$G_5 = 29.2\ (\text{GeV})^{-4}$$

$$A_1 = 3.8\ (\text{GeV/c})^2$$

$$\sigma_{T1} = 17.5\ \text{mb}$$

$$q_1 = 1.24\ \text{GeV/c} \qquad \text{VI-6}$$

$$C_1 = .94$$

$$\gamma_1 = .086$$

$$C_2 = 1.$$

$$\gamma_2 = .064$$

The predictions of the OPEA model for the K^+N data at 3.8 GeV/c were calculated from the code "OPEA."[39] The code was modified in order to incorporate the impulse approximation. Using the values of the OPEA parameters given by equation VI-6, it was found that the model predicted the general t dependence of $\rho_{00}^{PP}\frac{d\sigma}{dt}$, $\rho_{11}^{PP}\frac{d\sigma}{dt}$ and $Re(\rho_{10}^{PP})\frac{d\sigma}{dt}$, however the predictions were consistently too large. In addition the model gave the wrong sign for $\rho_{1-1}^{PP}\frac{d\sigma}{dt}$.

The five parameters of the OPEA model were then adjusted in three different chi squared fits. In the first, the parameters were adjusted to obtain a chi squared best fit to $\rho_{00}^{PP}\frac{d\sigma}{dt}$, $\rho_{11}^{PP}\frac{d\sigma}{dt}$, and $Re(\rho_{10}^{PP})\frac{d\sigma}{dt}$ for t between .04 and .44 $(GeV/c)^2$ (see Table VI-4). In the second, the t dependence of $\rho_{00}^{PP}\frac{d\sigma}{dt}$ and $\rho_{11}^{PP}\frac{d\sigma}{dt}$ was fit over the same t region. In the third, the t dependence of $\rho_{00}^{PP}\frac{d\sigma}{dt}$ was fit in the same t region. Table VI-5 shows the results of these three fits, the chi square per degree of freedom, initial best guesses to the values of the OPEA parameters and average of OPEA parameters and the error on the averages from the three fits. A number of additional fits were made starting at different initial values of the OPEA parameters and using different t ranges. These fits indicate that the chi square surface for the OPEA parameters does not have a sharp minimum. For this reason the average of the OPEA parameters listed in Table VI-5 is probably more meaningful than the results from any one fit. Also the error on the average OPEA parameter is probably a better estimate of the true error on the parameter.

Figure VI-4 shows the data from Figure VI-3 with the prediction of the chi square fit to $\rho_{00}^{PP}\frac{d\sigma}{dt}$ and $\rho_{11}^{PP}\frac{d\sigma}{dt}$ for t between .04 and .44 $(GeV/c)^2$. The agreement between the other two fits and the data is very

	G_5	γ_1	γ_2	C_1	C_2	χ^2/(degree of freedom)
initial value from equation VI-6	29.2	.086	.064	.94	1.	
$\rho_{00}^{PP}\frac{d\sigma}{dt}$, $\rho_{11}^{PP}\frac{d\sigma}{dt}$, $Re(\rho_{10}^{PP})\frac{d\sigma}{dt}$	33.±1.	.016±.005	.14 ±.06	.89±.04	1.00±.002	2.67
$\rho_{00}^{PP}\frac{d\sigma}{dt}$, $\rho_{11}^{PP}\frac{d\sigma}{dt}$	39.±2.	.014±.002	.040±.004	.77±.03	1.00±.002	1.70
$\rho_{00}^{PP}\frac{d\sigma}{dt}$	37.±5.	.030±.003	.037±.004	1.00±.04	1.00±.050	2.25
average of parameters from fits and error on the average OPEA parameter	36.±2.	.020±.006	.07 ±.03	.89±.06	1.0 ±.02	

TABLE VI-5. Table VI-5 shows the OPEA parameters from three fits to the data from Table VI-4 in the t region .04 to .44 GeV/c. Also shown are initial value for the OPEA parameters as well as the average of the OPEA parameters from the three fits and the error on the average.

FIGURE VI-4. Figure VI-4 shows the predictions of the OPEA model for all the P-wave density matrix elements times the differential cross section when $\rho_{00}^{PP} \frac{d\sigma}{dt}$ and $\rho_{11}^{PP} \frac{d\sigma}{dt}$ were fit by a least squares fit for t between .04 and .44 $(GeV/c)^2$.

VI-4a

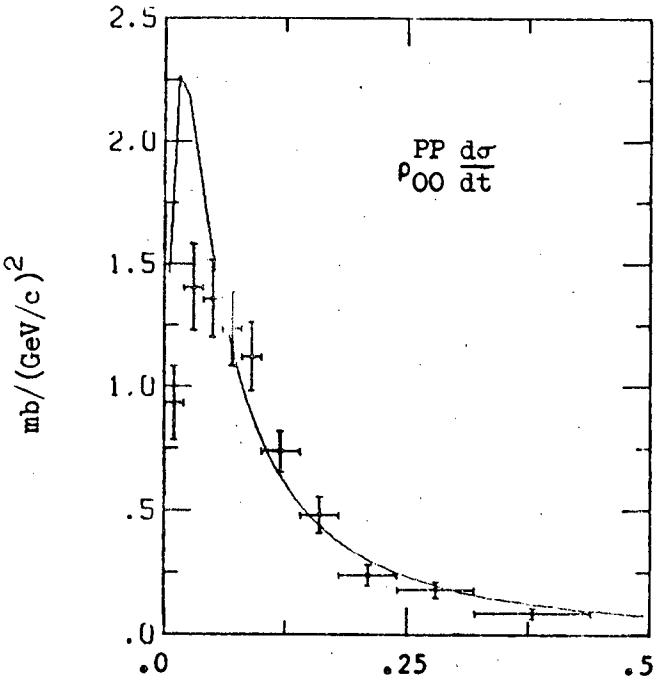
2.5
2.0
1.5
1.0
.5
.0
.0
.25
.5
mb/(GeV/c)^2
$\rho_{00}^{PP} \frac{d\sigma}{dt}$

VI-4b

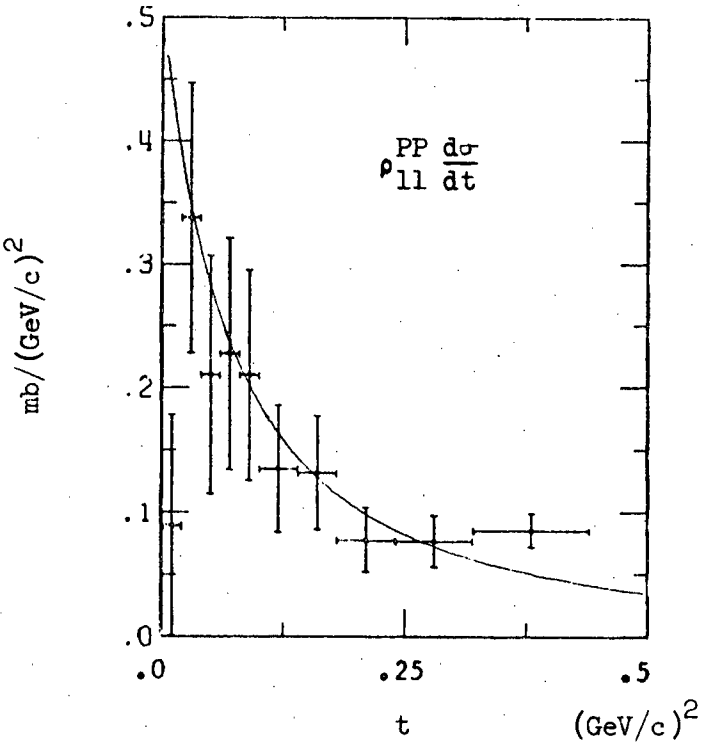
.5
.4
.3
.2
.1
.0
.0
.25
.5
mb/(GeV/c)^2
$\rho_{11}^{PP} \frac{d\sigma}{dt}$
t
(GeV/c)^2

VI-4c

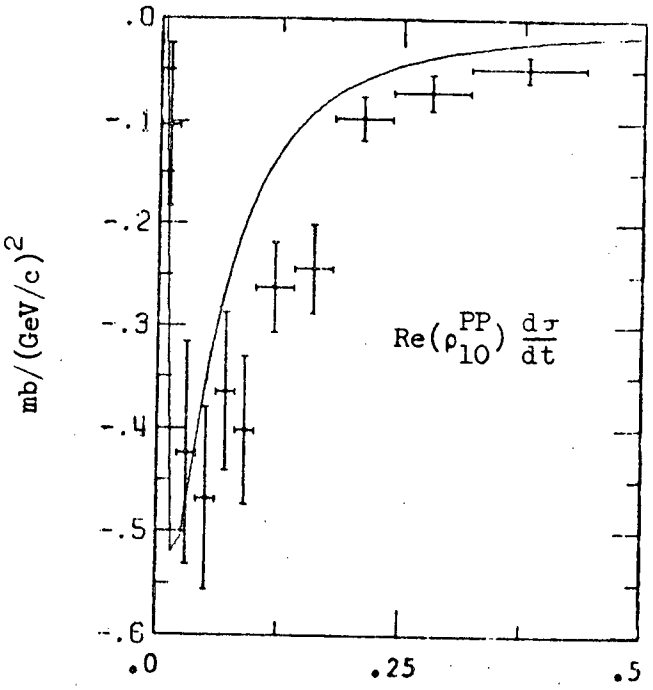
.0
-.1
-.2
-.3
-.4
-.5
-.6
.0
.25
.5
mb/(GeV/c)^2
$\mathrm{Re}(\rho_{10}^{PP})\ \frac{d\sigma}{dt}$

VI-4d

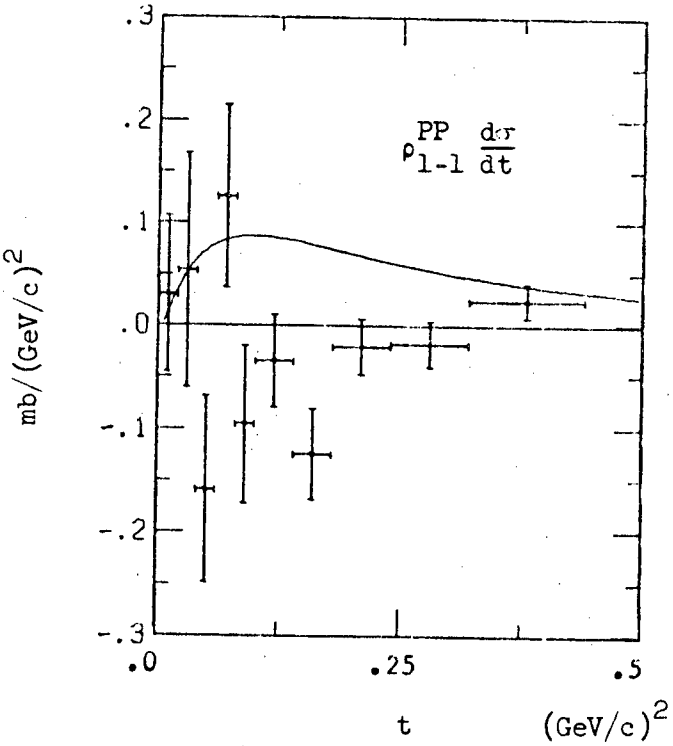
.3
.2
.1
.0
-.1
-.2
-.3
.0
.25
.5
mb/(GeV/c)^2
$\rho_{1-1}^{PP}\ \frac{d\sigma}{dt}$
t
(GeV/c)^2

similar even though the OPEA parameters are somewhat different. An examination of the fit shows that $\rho^{PP}_{1-1}\frac{d\sigma}{dt}$ has the wrong sign. The fit reproduces the general t dependence of $Re(\rho^{PP}_{10})\frac{d\sigma}{dt}$, although the predictions of the fit are somewhat low. The agreement between $\rho^{PP}_{00}\frac{d\sigma}{dt}$ and $\rho^{PP}_{11}\frac{d\sigma}{dt}$ is very good except in the first three bins where the data is consistently lower than the fit. To a large extent the disagreement in the first bin is a reflection of the curvature of the kinematic boundary of the t versus $m_{K\pi}$ plot at 3.8 GeV/c. The model has included the impulse approximation corrections for the suppression of the cross section in the forward direction, but this suppression was insufficient to account for the disagreement in the second and third bins. It has been noted in reaction VI-4 at 3.9 and 4.6 GeV/c that the OPEA model predictions are approximately 20% too high to t less than .1 $(GeV/c)^2$.[40] In this latter case the impulse approximation corrections do not have to be made since there is only one nucleon in the final state.

In summary, it was found that after adjusting the parameters of the model, the OPEA model agreed well with $\rho^{PP}_{00}\frac{d\sigma}{dt}$, $\rho^{PP}_{11}\frac{d\sigma}{dt}$ and $Re(\rho^{PP}_{10})\frac{d\sigma}{dt}$ in the t region between .04 and .44 $(GeV/c)^2$. The model predicts that $\rho^{PP}_{1-1}\frac{d\sigma}{dt}$ is small; however it disagrees in sign with this density matrix element.

D. The Reggeized One Pion Exchange Model of Abrams and Maor

Abrams and Maor have proposed a model for $V^o\Delta^{++}$ production which uses an evasive Reggeized one pion exchange to calculate $\rho_{00}\frac{d\sigma}{dt}$.[6] The model reduces to the Born term at the pion pole. Specifically the model consists of replacing the pion propagator in the Born term with the Regeized expression VI-6.

$$\frac{1}{t-m_\pi^2} = \pi\,\alpha'(0)\,\frac{1+e^{-i\pi\alpha}}{2\sin\pi\alpha}\,\frac{(1+2\alpha)\,(1+2\alpha/3)\,\Gamma(\alpha+.5)}{\Gamma(.5)\,\Gamma(\alpha+1)}\,\left(\frac{s-u}{2s_o}\right)^{\alpha} \qquad \text{VI-6}$$

$$\alpha = \alpha'(0)(t-m^2_\pi)$$

For reaction VI-7, Abrams and Maor determined $\alpha'(0)$ to be (1.16 ± 0.03) $(\text{GeV/c})^{-2}$ and $2s_o$ to be (1.08 ± 0.11) GeV^2.

$$\pi^+ P \rightarrow \rho^o \Delta^{++} \qquad \text{VI-7}$$

Lissauer has applied the model to reaction VI-8 at 12 GeV/c and found that it fits the data fairly well.[36]

$$K^+ N \rightarrow K^{*o}(890)\, P \qquad \text{VI-8}$$

In order to compare the model with reaction VI-8 at 3.8 GeV/c the substitution of equation VI-6 was made in the Born term equation VI-9.[41]

$$\frac{d\sigma}{dt} = \frac{\pi}{sq^2}\; G^2\, a_c^2\, [(m_N-m_P)^2-t]\, \frac{1}{(t-m^2)^2} \qquad \text{VI-9}$$

$$a_c^2 = .25\,[t-(m_K-m_{K^*})^2][t-(m_K+m_{K^*})^2]/m^2_{K^*}$$

$$q^2 = .25\,[s-(m_K-m_N)^2][s-(m_K+m_N)^2]/s$$

s = square of cm energy of the reaction

t = square of invariant momentum transfer; it is negative.

$$G^2 = \frac{g^2_{K^*K^+\pi^-}}{4\pi} \quad \frac{g^2_{N\pi P}}{4\pi}$$

In addition the impulse approximation was incorporated into the model by assuming that the Born term is completely due to the spin-flip amplitude.

Starting from the values for $\alpha'(0)$ and $2s_o$ given by Abrams and Maor and with the nominal value of G^2 of 29.2 $(GeV)^{-4}$ (see equation VI-5), a least squares fit was made to $\rho^{PP}_{00} \frac{d\sigma}{dt}$ between .04 and .44 $(GeV/c)^2$. In addition a second fit was made assuming that the π and B trajectories are degenerate. In this case the term $(1+e^{-i\pi\alpha})/(2\sin\pi\alpha)$ in equation VI-6 was replaced by $1/(\sin\pi\alpha)$. Table VI-6 shows the results of these two fits, the chi square per degree of freedom and the initial values of $\alpha'(0)$, $2s_o$ and G^2. From the chi square per degree of freedom, it is seen that the two fits are roughly the same in their agreement with the data. Both fits have a value of G^2 which is about 25% less that the nominal value of 29.2 $(GeV)^{-4}$. Abrams and Maor also observed that the coupling constant for reaction VI-7 was less than the nominal value; in this case it was about 50% too low.

Figure VI-5 shows the data for $\rho^{PP}_{00} \frac{d\sigma}{dt}$ and the predictions of the fit having degenerate π-B exchange. The agreement between the data and the fit for π exchange is very similar, and hence not displayed. The fit is seen to agree very well with the data except in the first 3 bins where the data is lower than the predictions of the fit. The first bin is low primarily because of the effect of the kinematic boundary of the t versus $m_{K\pi}$ plot. The model has included the impulse approximation corrections

	$\alpha'(0)$ $(GeV/c)^{-2}$	$2s_o (GeV)^2$	G^2 $(GeV)^{-4}$	χ^2 per degree of freedom
initial value	1.16 ± 0.03	1.08 ± 0.11	29.2	--
fit of π exchange	1.03 ± 0.04	1.07 ± 0.16	20.6 ± 1.0	1.03
fit for π-B exchange degeneracy	1.19 ± 0.04	1.00 ± 0.13	22.9 ± 1.1	0.95

TABLE VI-6. Table VI-6 shows the initial values for the Regge model of Abrams and Maor, the results of fits to $\rho_{00}^{PP} \frac{d\sigma}{dt}$ for π exchange and for π-B degenerate exchange and the chi square per degree of freedom. The t region fit was .04 to .44 $(GeV/c)^2$

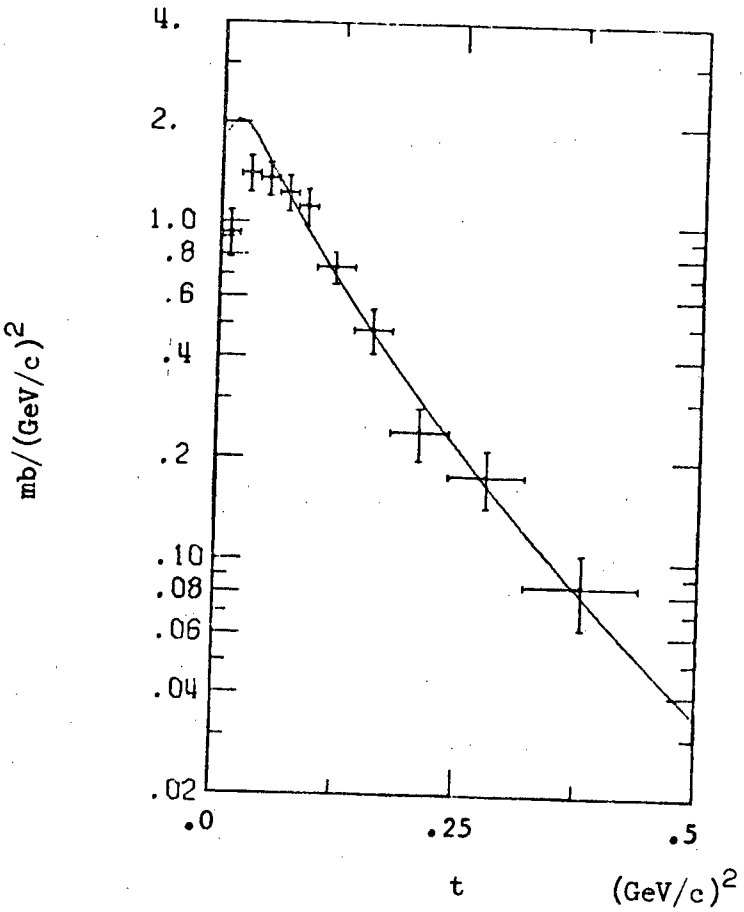

FIGURE VI-5. Figure VI-5 shows the prediction of the Reggeized one pion exchange model of Abrams and Maor for $\rho_{00}^{PP} \frac{d\sigma}{dt}$ when the π-B trajectories are assumed to be degenerate.

for the suppression of the cross section in the forward direction, but this suppression was insufficient to account for the disagreement in the second and third bins.

In summary, it was found that the Regge model of Abrams and Maor fit the t dependence of $\rho_{00}^{PP} \frac{d\sigma}{dt}$ very well for either π exchange only or degenerate π-B exchange. The fit values of $\alpha'(0)$ and $2s_o$ were similar to those found by Abrams and Maor. The fit value for the product of the coupling constants, G^2, was lower than the nominal value, but this appears to be a general feature of the model.

VII. COMPARISON OF NEUTRAL $K\pi$ SYSTEMS PRODUCED IN NUCLEON CHARGE EXCHANGE REACTIONS

A. Introduction

Reactions VII-1 and VII-2 are related since the same t channel changes contribute to both reactions.

$$K^+N \rightarrow (K\pi)^oP \qquad \text{VII-1}$$

$$K^-P \rightarrow \overline{(K\pi)}^oN \qquad \text{VII-2}$$

In going from one t-channel reaction to the other, the signs of some of the amplitudes change. Equations VII-3 show the most common t-channel exchanges and the sign changes in going from a K^+N reaction to a K^-P reaction.

$$A_{K^+N} = A_\pi + A_B + A_{A_2} + A_\rho$$

$$A_{K^-P} = A_\pi - A_B + A_{A_2} - A_\rho \qquad \text{VII-3}$$

For both reactions, pion exchange is the dominant t-channel exchange mechanism. Absorption effects arise from S-channel interactions between the initial particles and/or interactions between the final particles. Since the total cross section for the K^-P is larger than the total cross section for K^+N, absorption effects for reactions VII-1 and VII-2 are different.

A study of the similarities and differences between the differential cross sections and density matrix elements for reactions VII-1 and VII-2 in the regions of the $K^{*o}(890)$ and $K^{*o}(1420)$ may be able to give additional information about the amplitudes.

This chapter compares $K^*(890)$ and $K^*(1420)$ production in a K^+N reaction at 3.8 GeV/c and a K^-P reaction at 3.9 and 4.6 GeV/c.[7] The $K^*(890)$ will be considered first and in greatest detail. The $K^*(1420)$ will be compared next; however the analysis will be less detailed because there is less data and also more confusion about the various partial waves and their importance.

B. Properties of the $K^{*o}(890)$

1. Cross Section

The cross section for $K^{*o}(890)$ production for the K^+N reaction at 3.8 GeV/c was obtained my making a least squares fit to the mass plot using equation VII-4.[22]

$$Y = (1 + C\ BW_J)\ P_n(m-m_c)$$

$$BW_J = \frac{m}{q}\ \frac{\Gamma_J}{(m^2-m_o^2)^2 + m_o^2\Gamma_J^2} \qquad \text{VII-4}$$

$$\Gamma_J = \Gamma_o \left(\frac{q}{q_o}\right)^{2J+1}$$

In equation VII-4, P_n is a polynomial expanded about m_c. In fitting the mass plot over the region .80 to 1.00 GeV, m_c was set to .9 GeV. The fit

adjusted the constant C, the resonant mass, m_o, the width, Γ_o, and the coefficients of the polynomial. Using a mass binning of .002 GeV in a mass plot with 1820 events and a linear polynomial, a fit with a chi square per degree of freedom of 1.20 was obtained. A quadratic mass dependence for P_n resulted in an increase in the chi square per degree of freedom to 1.21.

Table VII-1 shows the mass and width of the $K^{*o}(890)$ from the fit to the 3.8 GeV/c K^+N data, and the mass and width of the $\overline{K^{*o}(890)}$ from the K^-P data at 3.9 GeV/c [7] and from the Particle Data Group.[35] In the K^+N data, the statistical error on the mass of the $K^*(890)$ is 1.1 MeV and the error on the width is 2.7 MeV. The errors given for the K^+N data in Table VII-1 include estimates of errors due to the choice of the parameterization.

The widths found for the $K^*(890)$ for both the K^+N reaction and the K^-P reaction are consistent with the width given by the Particle Data Group.[35] On the other hand the mass values found for both reactions are higher than the mass listed by the Particle Data Group. The reason for the apparent discrepancy depends upon the details of the fitting procedure. In the fits there is a factor of m/q (see equation VII-4) which causes the resonant mass to be larger than would be found by fits which do not contain this factor. This illustrates just one reason why care must be used in comparing resonant masses and widths given by different experiments. In general different functional forms for the resonance parameterization will yield slightly different resonant masses and widths.

Figure VII-1 shows the fit to the $K\pi$ mass plot for the region .80 to 1.00 GeV for the K^+N reaction at 3.8 GeV/c.

	M_o (MeV)	Γ_o (MeV)
$K^+N \rightarrow K^*(890)P$ at 3.8 GeV/c	896. ± 2.	50. ± 4.
$K^+P \rightarrow \overline{K^*(890)}N$ at 3.9 GeV/c [7]	897.8 ± 0.8	55.3 ± 2.6
nominal values from Particle Data Group[35]	892.55 ± 0.45	53.0 ± 1.1

TABLE VII-1. Table VII-1 shows the mass and width of the K*(890) from the fit to the 3.8 GeV/c K^+N data and the mass and width of the K*(890) from the K^-P data at 3.9 GeV/c [7] and from the Particle Data Group.[35]

From the fit to the mass plot in the region .80 to 1.00 GeV, the cross section for $K^{*o}(890)$ production in the K^+N reaction at 3.8 GeV/c was found to be (.80 ± .07) mb. The cross section includes a correction for unseen decay modes. For the K^-P reaction at 3.8 GeV/c, Aguilar-Benitez et al. using the same mass region and fitting procedure found the cross section for $\overline{K^{*o}(890)}$ production to be (.755 ± .030) mb.

Figure VII-2 shows the dependence of the cross section for K*(890) production for K^+N and K^-P reactions as a function of the momentum of the kaon in the laboratory.[23,40,42-49] This Figure is based upon a Figure by Cords et al.[23] The momentum dependence of the cross section is roughly the same for both reactions. The line is a fit to P_{lab}^{-n} where n was found to be 2.24 ± 0.15 in a fit by Cords et al.[23]

The total cross section predicted by the OPEA model (see Section VI-C) agrees well with the data for both reactions; however there is a slight tendency for the cross sections to fall more slowly than the

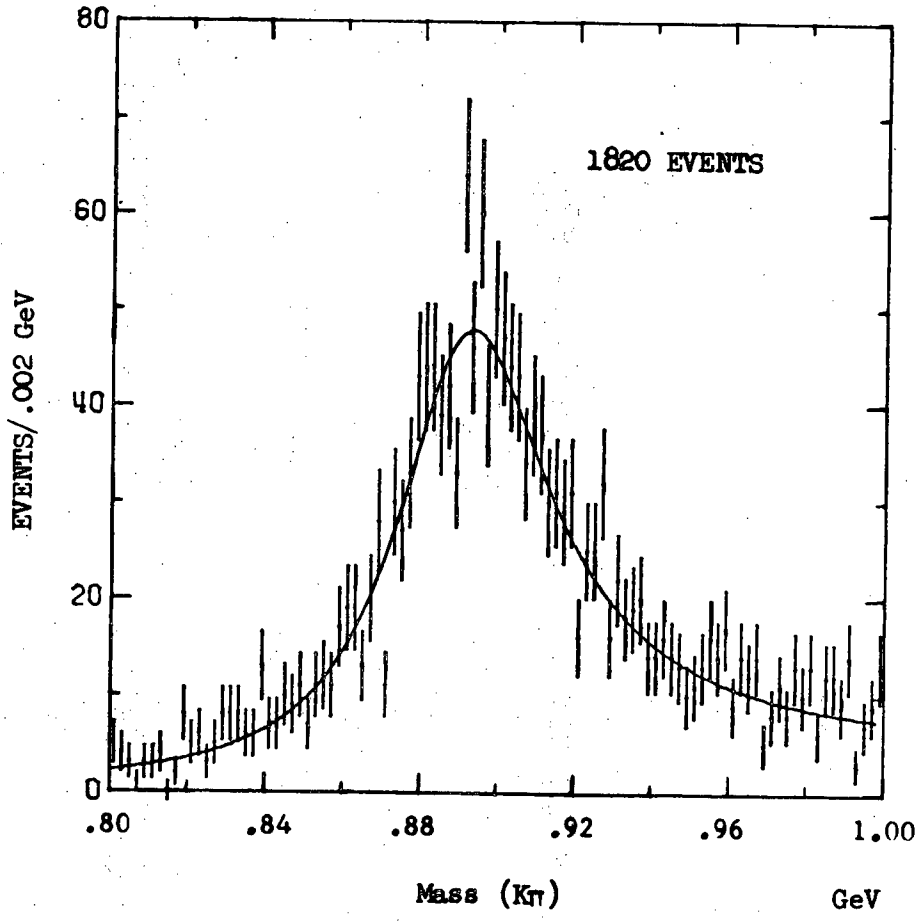

FIGURE VII-1. Figure VII-1 shows the fit to the $K\pi$ mass plot for the reaction $K^+N \rightarrow K^+\pi^-P$ at 3.8 GeV/c.

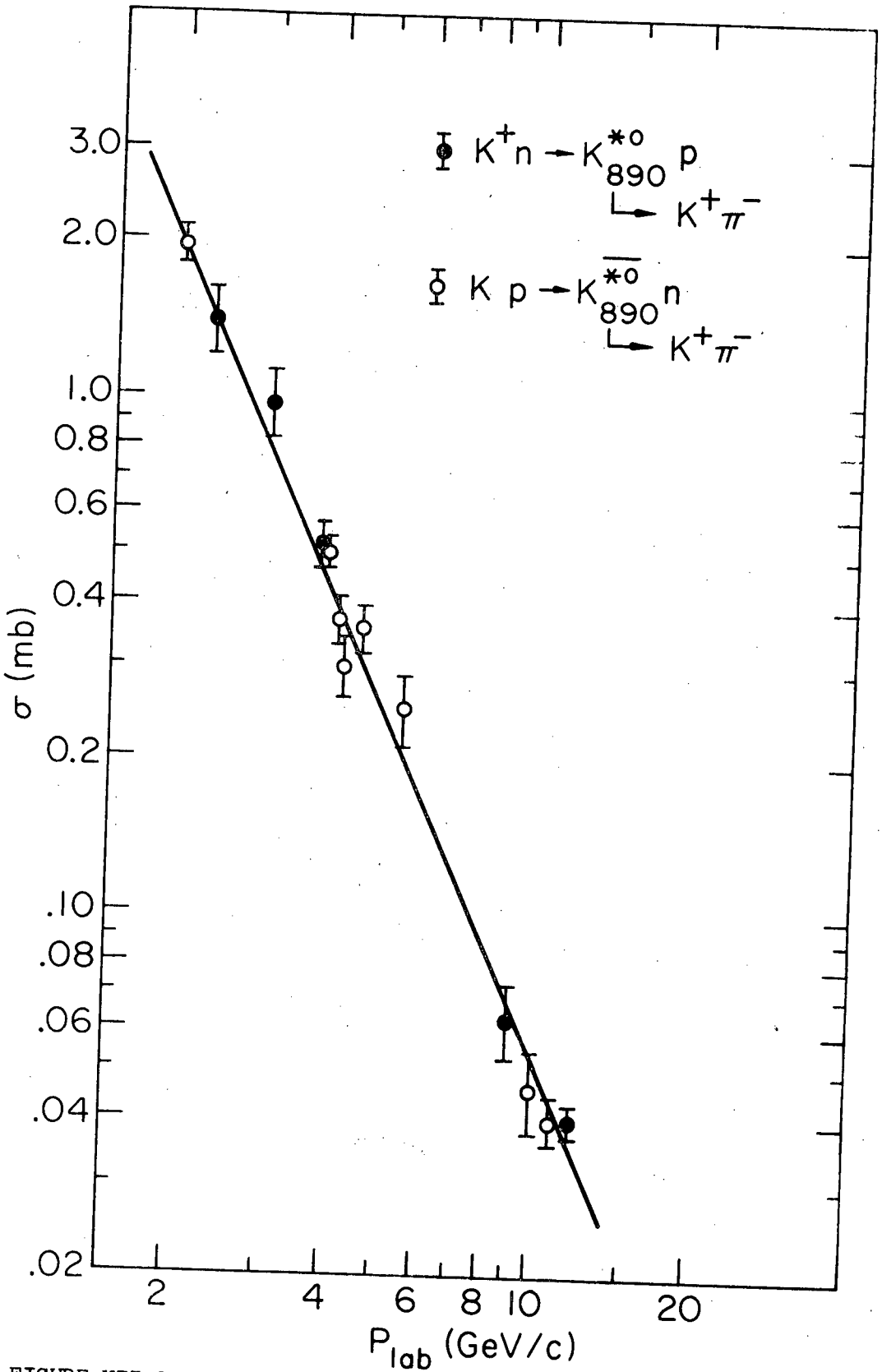

FIGURE VII-2. Figure VII-2 shows the dependence of the cross section for $K^{*o}(890)$ production for K^+N and K^-P reactions as a function of the momentum of the kaon in the laboratory. The line is a fit to P_{lab}^{-n} where n was found to be 2.24±15 in a fit by Cords et al.[23]

predictions of the OPEA model.[23] The OPEA model also predicts that the cross section for $\overline{K^{*o}(890)}$ is slightly smaller than the cross section for $K^{*o}(890)$ production. The figure offers some support to this prediction

2. Differential Cross Section

The differential cross section, $d\sigma/dt$ for $K^{*o}(890)$ production in the K^+N reaction at 3.8 GeV/c was obtained by making t cuts on the $K\pi$ mass spectrum and then making a background subtraction in the mass region .80 to 1.00 GeV. Specifically the mass region was fit using a chi square fit to equation VII-5.

$$Y = [C_1 + C_2(m-m_c) + C_3 B_J] \Phi (m,t_1,t_2) \qquad \text{VII-5}$$

Here C_1, C_2 and C_3 are constants which are adjusted by a linear least square fitting program. The constant m_c was set to .9 GeV. B_J is given by equation IV-21 and Φ is the peripheralized phase space of equation IV-18 which has been integrated over all $\cos\Theta$ and ϕ and over t from t_1 to t_2. The parameters in the function B_J were set to the values given for the P-wave in Table IV-5. The use of Φ is especially advantageous in the small t regions where t_{min} may be less than t_1; in this case there is a discontinuity in phase space which is probably approximated fairly well by Φ.

Table VII-2 shows the t cuts, the number of events for the mass region .80 to 1.00 GeV and the differential cross section for the $K^{*o}(890)$ which has been corrected for unseen neutral decays. Figure VII-3 is a plot of the differential cross section. The differential cross section

t region	total no. events	$\frac{d\sigma}{dt}$ (mb)
.01 - .02	81	3.31 ± .69
.02 - .04	208	3.90 ± .52
.04 - .06	174	3.30 ± .46
.06 - .08	163	3.16 ± .43
.08 - .10	122	2.86 ± .39
.10 - .12	93	2.17 ± .35
.12 - .14	80	1.79 ± .31
.14 - .16	81	1.16 ± .31
.16 - .18	67	1.36 ± .28
.18 - .20	45	.93 ± .24
.20 - .24	75	.51 ± .14
.24 - .28	61	.70 ± .13
.28 - .32	55	.48 ± .13
.32 - .36	65	.55 ± .14
.36 - .40	36	.36 ± .11
.40 - .52	84	.302± .052
.52 - .64	57	.220± .044
.64 - .76	48	.179± .049
.76 -1.00	46	.057± .019

TABLE VII-2. Table VII-2 shows the t cuts, the total number of events in the t cut for the mass region .80 to 1.00 GeV and the differential cross section for the $K^{*o}(890)$ which has been corrected for unseen neutral decays.

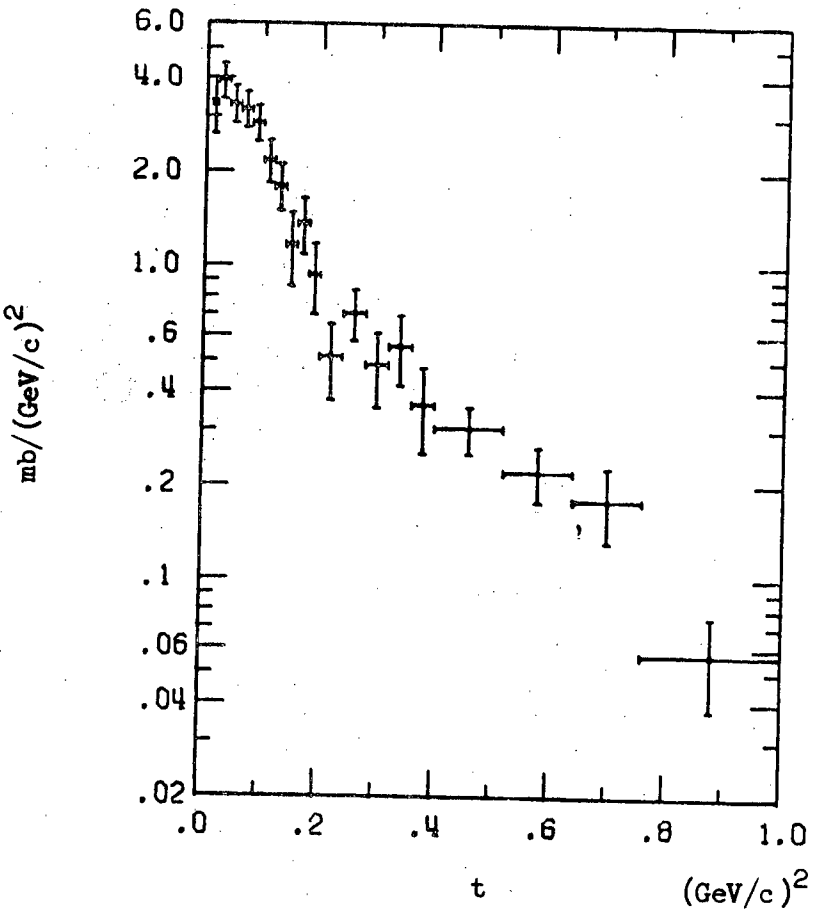

FIGURE VII-3. Figure VII-3 shows the differential cross section for $K^{*o}(890)$ after correcting for unseen neutral decays in the $K^{+}N$ reaction at 3.8 GeV/c.

in the forward direction has not been corrected for the effect of the Pauli Exclusion Principle (see Section II-1).

The differential cross section calculated by this method is nearly identical to the differential cross section found by considering all events in the mass region .84 to .94 GeV (see Figure VI-1).

Figure VII-4 is a plot of the differential cross section, $d\sigma/dt$, for $\overline{K^{*o}(890)}$ production in the K^-P reaction at 3.9 GeV/c.[7] This differential cross section was obtained by making t cuts on the $K\pi$ mass spectrum and then making a background subtraction in the mass region .80 to 1.00 GeV. Although the details of the background subtraction are slightly different, the differential cross sections for the K^+N reaction (see Figure VII-3) and the K^-P reaction (see Figure VII-4) were calculated by the same method, and hence can be compared directly.

The forward slope for the K^+N reaction for the t region 0.02 to .20 $(GeV/c)^2$ was found to be $(8.9 \pm .8)/(GeV/c)^2$ (see Table III-1). The K^-P reaction for the t region 0.02 to 1.00 $(GeV/c)^2$ was fit and found to have a slope of $(4.2 \pm 0.2)/(GeV/c)^2$.[7] A comparison of Figures VII-3 and VII-4 shows that the differential cross sections are very similar. The K^+N data shows a rather pronounced break in slope at about .2 $(GeV/c)^2$. The slope for the K^+N reaction was fit only over the region of the forward peak. On the other hand the slope of the K^-P data appears to be rather smooth. There is, however, a suggestion of a change in slope at about 0.1 $(GeV/c)^2$; unfortunately statistical fluctuations in the third and fourth bins make this suggestion very tenuous.

A comparison of the two differential cross sections over the entire t region from 0.0 to 1.0 $(GeV/c)^2$ suggests that the K^+N reaction has

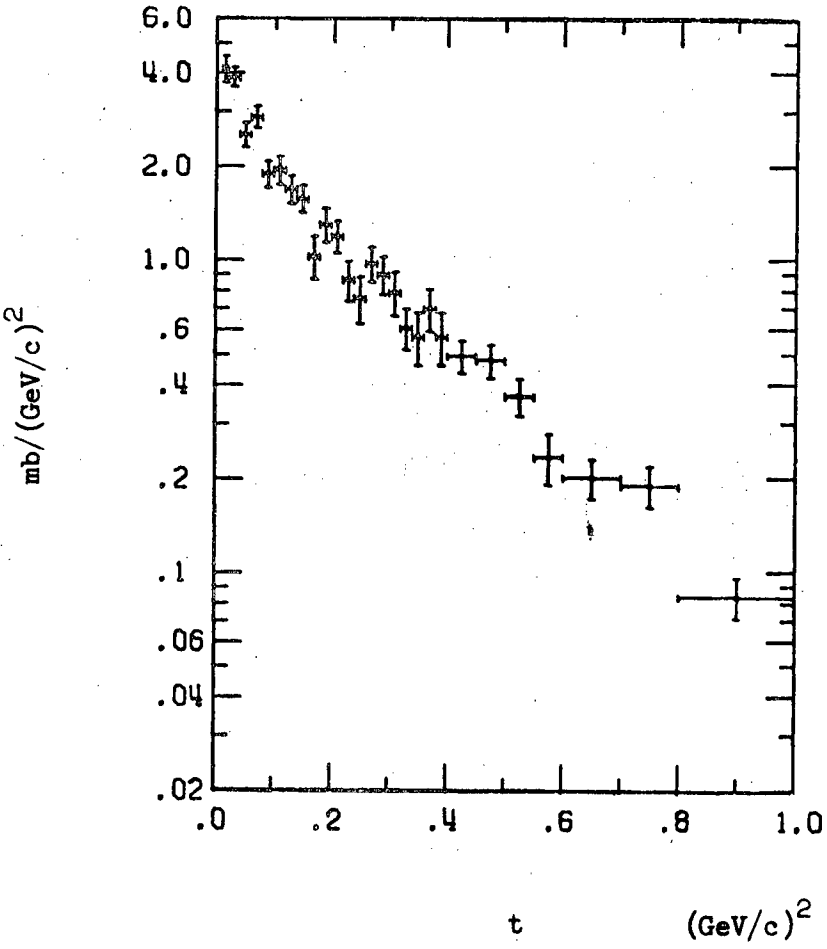

FIGURE VII-4. Figure VII-4 shows the differential cross section for $\overline{K^{*0}(890)}$ for the K^-P reaction at 3.9 GeV/c.[7]

destructive interference between two amplitudes while the K^-P reaction has constructive interference. The forward peak could be due to π or π-B exchange while ρ-A_2 exchange could perhaps explain the large t behavior.

3. Density Matrix Elements

Previous fits to the Y_{Lm} moments in the K*(890) region (see Chapters IV and VI) indicate that only S and P-waves are important in this region. Equation VII-6 parameterizes the resulting angular distribution in terms of P-wave density matrix elements and S-P interference density matrix elements.

$$W(\cos\theta,\phi) = \frac{1}{4\pi} + \frac{3}{4\pi}\left[(\rho_{00}^{PP}-\rho_{11}^{PP})(\cos^2\theta - \frac{1}{2}) - \sqrt{2}\,\mathrm{Re}(\rho_{10}^{PP})\,\sin 2\theta\,\cos\phi\right.$$

$$\left. - \rho_{1-1}^{PP}\,\sin^2\theta\,\cos 2\phi\right] \qquad \text{VII-6}$$

$$\frac{\sqrt{3}}{4\pi}\left[-2\sqrt{2}\,\mathrm{Re}(\rho_{10}^{PS})\,\sin\theta\,\cos\phi + 2\,\mathrm{Re}(\rho_{00}^{PS})\,\cos\theta\right]$$

Here $\rho_{mm'}^{JJ'}$ is the generalized density matrix element for the interference of spins J and J' with z-components m and m'. The trace condition has been used to replace the sum of ρ_{00}^{SS}, ρ_{00}^{PP} and $2\rho_{11}^{PP}$ by 1.

Using equation VII-6, the generalized density matrix elements were calculated by the method of moments in the K^{*o}(890) region (.84 to .94 GeV). In this method, the density matrix elements are obtained by averaging the appropriate projection operator over the allowed mass and

t regions. Equation VII-7 gives the projection operators corresponding to the case when only S and P-waves are present.

$$\rho_{00}^{PP} - \rho_{11}^{PP} = \langle \frac{5}{4} \cos^2\theta - \frac{1}{4} \rangle$$

$$Re(\rho_{10}^{PP}) = - \frac{5}{4\sqrt{2}} \langle \sin 2\theta \cos\phi \rangle$$

$$\rho_{1-1}^{PP} = - \frac{5}{4} \langle \sin^2\theta \cos 2\phi \rangle \qquad \text{VII-7}$$

$$Re(\rho_{10}^{PS}) = \sqrt{\frac{3}{2}} \langle \sin\theta \cos\phi \rangle$$

$$Re(\rho_{00}^{PS}) = \sqrt{\frac{3}{4}} \langle \cos\theta \rangle$$

Table VII-3 gives the density matrix elements in the Jackson frame for various t regions in the $K^{*o}(890)$ mass region (.84 to .94 GeV) at 3.8 GeV/c. The errors are statistical. Figure VII-5a-e shows the t dependence of these density matrix elements.

The t dependence of the density matrix elements as calculated by the method of moments agrees well with the values found in Section VI-B. In that section the denstiy matrix elements were obtained by making a background subtraction in the moments with respect to Y_{Lm}. For the moments Y_{21} and Y_{22} the background subtraction is small and hence the value of the density matrix element is roughly the same with and without the background subtraction.

t region	events	$\rho_{00}^{PP}-\rho_{11}^{PP}$	Re ρ_{10}^{PP}	ρ_{1-1}^{PP}	Re ρ_{10}^{PS}	Re ρ_{00}^{PS}
.00-.02	71	.71±.13	-.09±.05	.03±.06	-.03±.07	.16±.07
.02-.04	150	.39±.09	-.18±.04	.01±.05	-.15±.05	.18±.04
.04-.06	125	.65±.10	-.21±.04	-.06±.05	-.09±.06	.14±.05
.06-.08	120	.43±.10	-.17±.04	.08±.05	-.06±.05	.16±.05
.08-.10	102	.60±.12	-.24±.04	-.06±.05	-.12±.06	.31±.05
.10-.12	77	.49±.13	-.23±.05	-.01±.06	-.06±.07	.13±.06
.12-.14	64	.58±.14	-.24±.05	-.04±.06	-.12±.08	.13±.07
.14-.16	55	.43±.15	-.34±.06	-.18±.07	-.16±.09	.05±.08
.16-.18	51	.41±.16	-.22±.06	-.15±.07	-.25±.09	.17±.08
.18-.20	36	.34±.18	-.11±.07	.06±.10	-.08±.10	.02±.09
.20-.24	52	.28±.17	-.31±.04	-.11±.08	.08±.10	-.03±.08
.24-.28	48	.34±.18	-.19±.06	.06±.08	-.18±.09	.08±.08
.28-.32	42	.40±.19	-.23±.07	-.15±.09	-.05±.11	.14±.09
.32-.36	48	.01±.17	-.28±.06	-.02±.10	-.09±.10	.09±.07
.36-.42	46	-.02±.14	-.10±.06	.12±.08	-.11±.10	.08±.07
.42-.52	48	-.01±.16	-.21±.06	.08±.09	-.06±.10	.00±.07
.52-.64	46	.27±.16	-.18±.06	.10±.09	-.04±.09	.12±.08
.64-.76	41	.08±.17	-.13±.06	.16±.10	-.06±.10	-.06±.08
.76-1.00	39	-.09±.16	-.11±.08	-.06±.10	.19±.12	.04±.08

TABLE VII-3. Table VII-3 shows the values of the density matrix elements for the Jackson frame as a function of t for the K*(890) region (.84 to .94 GeV) for the K^+N reaction at 3.8 GeV/c

FIGURE VII-5. Figure VII-5 shows the t dependence of the density matrix elements in the Jackson frame for the reaction $K^+N \rightarrow K^+\pi^-P$ at 3.8 GeV/c for the mass of the $K\pi$ system between .84 and .94 GeV.

VII-5a

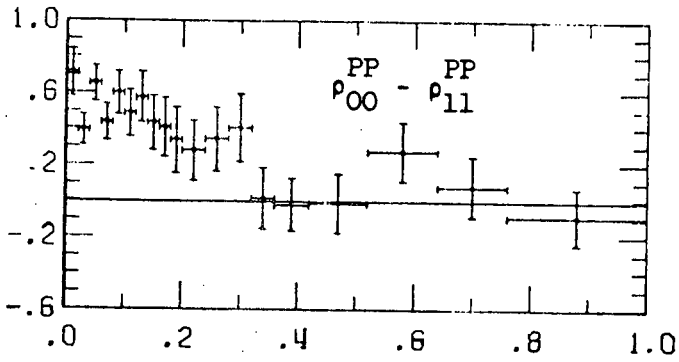

VII-5b

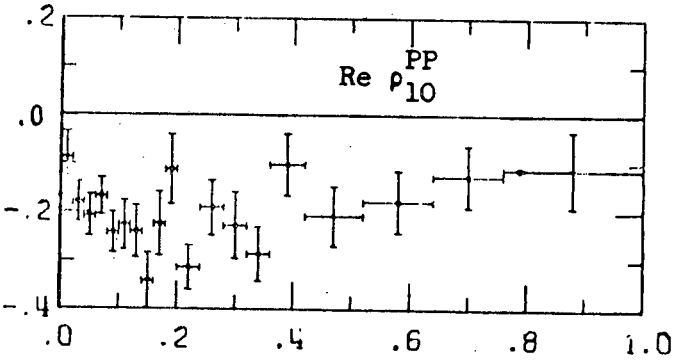

VII-5c

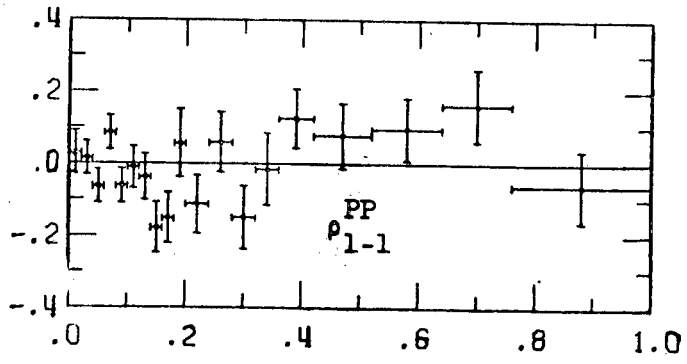

t $(GeV/c)^2$

VII-5d

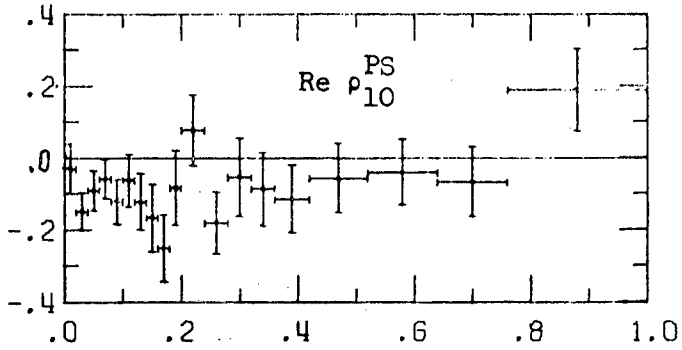

VII-5e

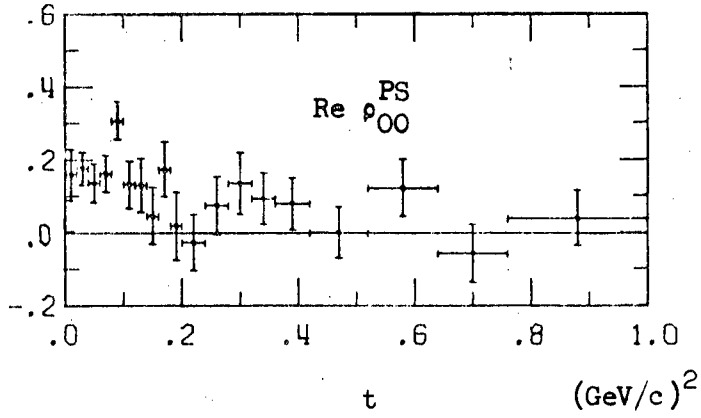

a. Density Matrices in the Jackson Frame

Figure VII-6a-e shows the t dependence of the density matrix elements in the Jackson frame in the $\overline{K^{*0}(890)}$ mass region (.84 to .94 GeV) for the combined data for K^-P reactions at 3.9 and 4.6 GeV/c.[7] The density matrix elements shown in the figure were calculated by the maximum likelihood method assuming that equation VII-6 is an adequate parameterization of the angular decay distribution. The values of the density matrix elements obtained by the maximum likelihood method usually agree well with the values obtained by the method of moments. Hence the density matrix elements found for the K^+N reaction can be compared directly with the values given for the K^-P data.

For t less than .5 $(GeV/c)^2$ the t dependences of $\rho_{00}^{PP} - \rho_{11}^{PP}$ and Re ρ_{00}^{PS} for the two reactions are nearly identical (see Figure VII-5a and VII-6a; Figure VII-5e and VII-6e). This is not surprising since pion exchange dominates in both reactions in the low t region and since pion exchange without absorption only populates the density matrix elements ρ_{00}^{PP}, ρ_{00}^{SS} and Re ρ_{00}^{PS}.

There is good agreement for Re ρ_{10}^{PS} for the two reactions (see Figures VII-5d and VII-6d). For t less than .5 $(GeV/c)^2$ there is some evidence that Re ρ_{10}^{PS} for the K^+N reaction is somewhat larger than for the K^-P reaction.

For low t, Re ρ_{10}^{PP} appears to have roughly the same t dependence for both reactions (see Figures VII-5b and VII-6b); however Re ρ_{10}^{PP} for the K^+N reaction is roughly twice as large as the density matrix element for the K^-P data. Also there is a tendency for Re ρ_{10}^{PP} in the K^-P data to go to zero faster for larger t values. From the fits to the OPEA model for

FIGURE VII-6. Figure VII-6 shows the t dependence of the density matrix elements in the Jackson frame for the reaction $K^-P \rightarrow K^-\pi^+N$ for the combined data at 3.9 and 4.6 GeV/c for the mass of the $K\pi$ system between .84 and .94 GeV.[7]

VII-6a

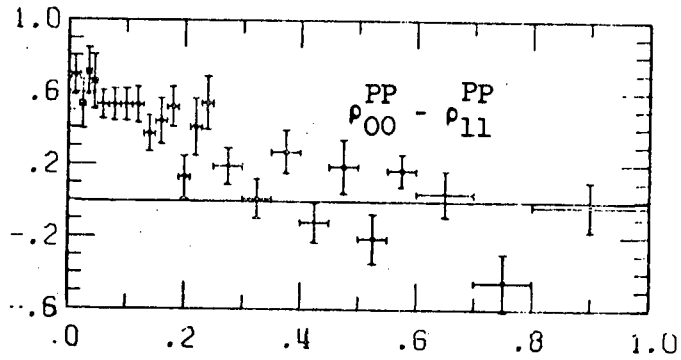

VII-6b

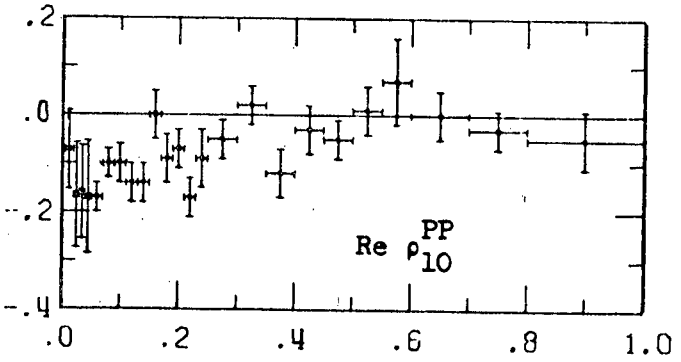

VII-6c

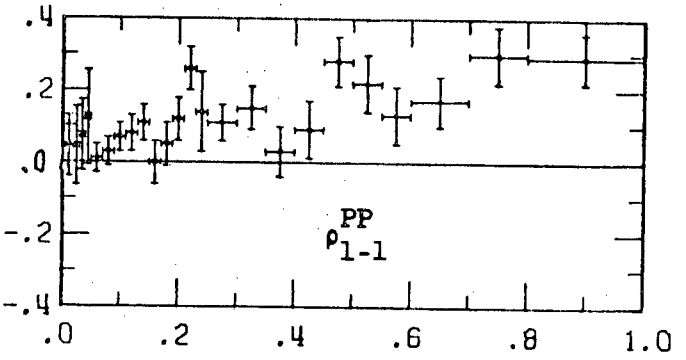

t $(GeV/c)^2$

VII-6d

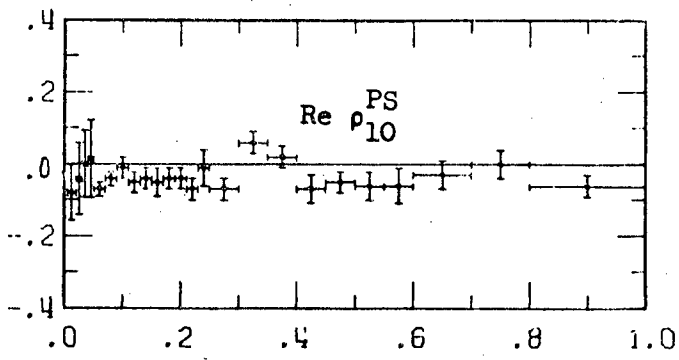

VII-6e

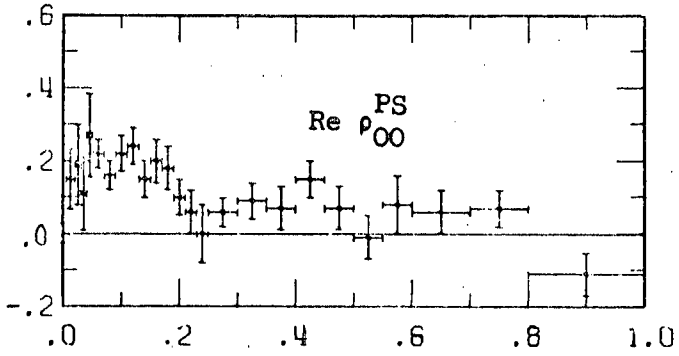

t $(GeV/c)^2$

the K^-P reaction,[7] it can be seen that above .2 $(GeV/c)^2$, Re ρ_{10}^{PP} becomes somewhat smaller than the value predicted by the model, while for the K^+N reaction Re ρ_{10}^{PP} becomes somewhat larger than the value predicted by the model.

To first order, ρ_{1-1}^{PP} for the K^+N data appears to be consistent with zero (see Figure VII-5c). However a careful examination of the t dependence of ρ_{1-1}^{PP} shows that it may be slightly negative for t less than .36 GeV/c and positive for t between .36 and .76 $(GeV/c)^2$. On the other hand ρ_{1-1}^{PP} is always positive for the K^-P data (see Figure VII-6c). It starts out small and increases more or less steadily with increasing t. The OPEA model gives a good description of the t dependence of ρ_{1-1}^{PP} for the K^-P data. In the K^+N data, however, the OPEA model also gives a t dependence similar to that given for the K^-P reaction.

There is some indication that the density matrix elements $\rho_{00}^{PP}-\rho_{11}^{PP}$, ρ_{1-1}^{PP}. Re ρ_{10}^{PS} and Re ρ_{00}^{PS} for the K^+N reaction become equal to the corresponding density matrix element in the K^-P reaction for t around .5 $(GeV/c)^2$.

In summary the agreement between the K^+N and K^-P data in the low t region for $\rho_{00}^{PP}-\rho_{11}^{PP}$, Re ρ_{10}^{PP}, Re ρ_{00}^{PS} and Re ρ_{10}^{PS} in the Jackson frame can be explained in terms of the OPEA model. In this model, to first order without any absorption, only ρ_{00}^{PP}, ρ_{00}^{SS} and Re ρ_{00}^{PS} are non zero. When interactions between the initial particles and between the final particles are taken into account, the absorption for the two reactions will be different and hence the values of Re ρ_{10}^{PP} and Re ρ_{10}^{PS} will be different. Aguilar-Benitez et al.[7] have shown that ρ_{1-1}^{PP} for the K^-P data is also

well described by the OPEA model in the forward direction. The OPEA model gives the wrong sign and t dependence for ρ^{PP}_{1-1} for the K^+N data.

b. Density Matrices in the Helicity Frame

Table VII-4 gives the density matrix elements in the helicity frame for various t regions in the K*(890) mass region (.84 to .94 GeV) for the K^+N reaction at 3.8 GeV/c. The errors are statistical. Figure VII-7a-e shows the t dependence of these density matrix elements. Figure VII-8a-e shows the t dependence of the corresponding helicity density matrix elements for the $\overline{K^{*o}(890)}$ from the combined K^-P data at 3.9 and 4.6 GeV/c.[7]

For both reactions $\rho^{PP}_{00}-\rho^{PP}_{11}$ remains large and then abruptly drops off and becomes negative at large t values. In the K^-P data this drop off is at 0.07 $(GeV/c)^2$ (see Figure VII-8a) while for the K^+N data the drop off occurs at .18 $(GeV/c)^2$ (see Figure VII-7a). For t larger than about .5 $(GeV/c)^2$ the values of $\rho^{PP}_{00}-\rho^{PP}_{11}$ for the two reactions become about equal.

The t dependences of Re ρ^{PS}_{00} for the two reactions is similar (see Figures VII-7e and VII-8e). For both reactions Re ρ^{PS}_{10} is small and the values are roughly consistent (see Figures VII-7d and VII-8d).

The agreement between Re ρ^{PP}_{10} and ρ^{PP}_{1-1} for the two reactions is not very good. Re ρ^{PP}_{10} for both rise at about the same rate until t is about .06 $(GeV/c)^2$. However then Re ρ^{PP}_{10} for the K^-P reaction levels off and falls back to zero (see Figure VII-8b) while Re ρ^{PP}_{10} for the K^+N reaction continues rising until it levels off around .44 for t equal to about .2 $(GeV/c)^2$ (see Figure VII-7b). For the K^-P data ρ^{PP}_{1-1} starts out slightly

t region	events	$\rho_{00}^{PP}-\rho_{11}^{PP}$	Re ρ_{10}^{PP}	ρ_{1-1}^{PP}	Re ρ_{10}^{PS}	Re ρ_{00}^{PS}
.00-.02	71	.71±.13	-.10±.06	.05±.06	.00±.07	.16±.07
.02-.04	150	.57±.09	-.20±.04	.09±.04	-.09±.05	.20±.05
.04-.06	125	.77±.10	-.22±.04	.09±.04	-.04±.05	.15±.06
.06-.08	120	.43±.10	-.27±.03	.23±.05	-.02±.05	.15±.05
.08-.10	102	.66±.11	-.29±.04	.16±.05	-.01±.05	.27±.06
.10-.12	77	.51±.14	-.30±.04	.21±.05	.00±.06	.11±.07
.12-.14	64	.47±.15	-.33±.04	.24±.06	-.06±.06	.14±.07
.14-.16	55	.78±.14	-.50±.04	.06±.07	-.11±.07	.13±.08
.16-.18	51	.47±.15	-.46±.04	.04±.08	-.16±.08	.23±.08
.18-.20	36	.02±.19	-.33±.05	.28±.10	-.05±.09	.06±.08
.20-.24	52	.48±.16	-.43±.04	.21±.07	.02±.07	-.06±.08
.24-.28	48	-.03±.15	-.39±.05	.24±.08	-.18±.08	.14±.07
.28-.32	42	.22±.18	-.48±.04	.06±.10	-.04±.10	.06±.08
.32-.36	48	.18±.17	-.43±.04	.18±.09	-.01±.08	.07±.08
.36-.42	46	-.18±.13	-.44±.04	.26±.09	-.15±.09	.08±.07
.42-.52	48	-.13±.14	-.44±.04	.16±.09	-.11±.09	.04±.07
.52-.64	46	-.36±.13	-.39±.04	.27±.10	-.03±.09	.01±.06
.64-.76	41	-.39±.16	-.32±.05	.32±.10	.03±.10	.06±.06
.76-1.00	39	-.03±.18	-.42±.04	.06±.10	.08±.11	-.14±.08

TABLE VII-4. Table VII-4 shows the values of the density matrix elements for the helicity frame as a function of t for the K*(890) region (.84 to .94 GeV) for the K^+N reaction at 3.8 GeV/c.

FIGURE VII-7. Figure VII-7 shows the t dependence of the density matrix elements in the helicity frame for the reaction $K^+N \rightarrow K^+\pi^-P$ at 3.8 GeV/c for the mass of the $K\pi$ system between .84 and .94 GeV.

VII-7a

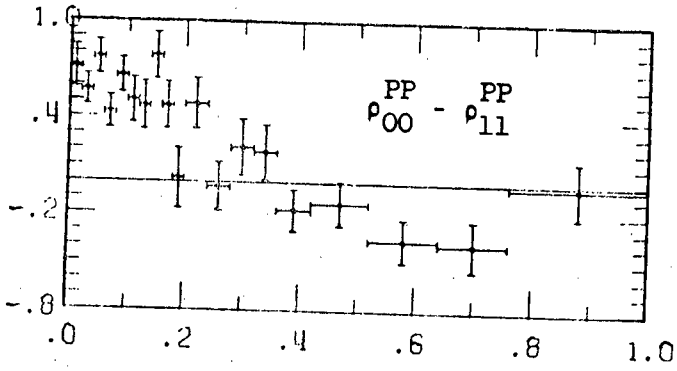

VII-7b

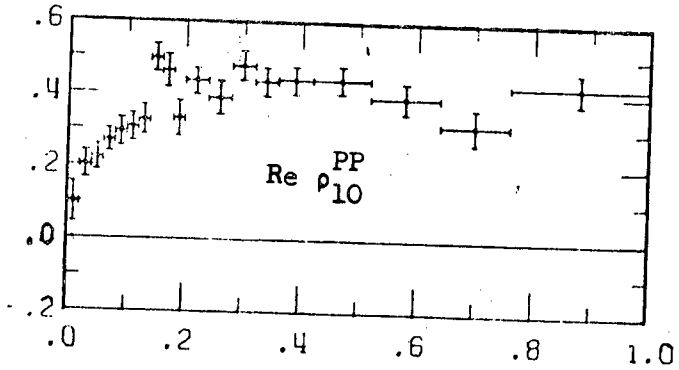

VII-7c

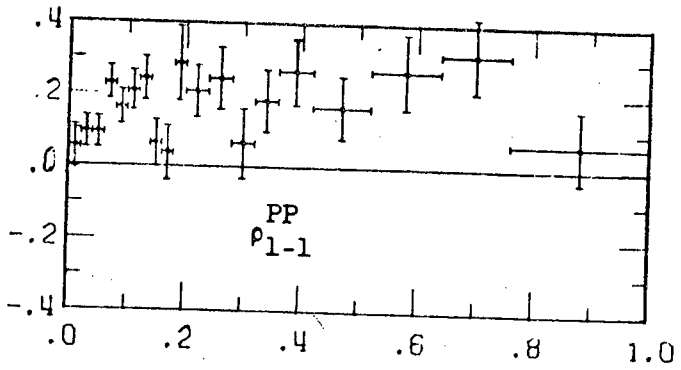

t $(GeV/c)^2$

VII-7d

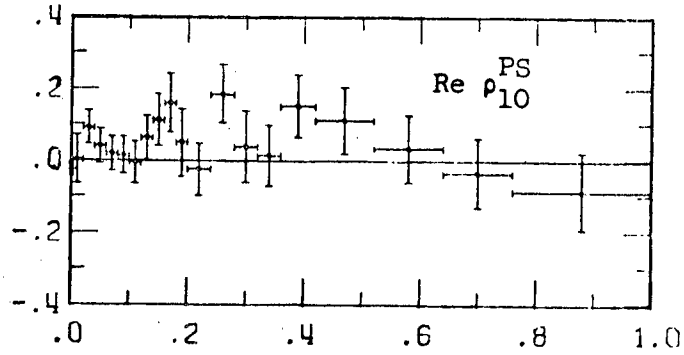

VII-7e

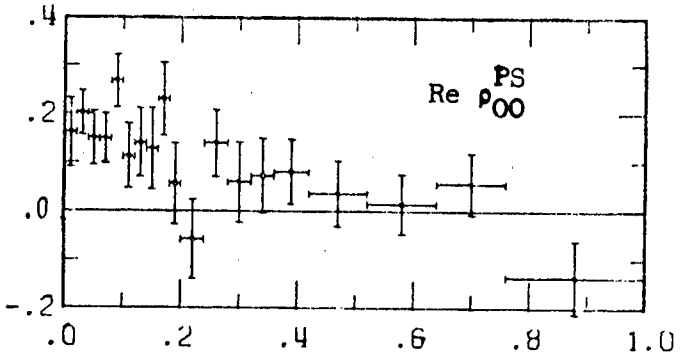

t $(GeV/c)^2$

FIGURE VII-8. Figure VII-8 shows the t dependence of the density matrix elements in the helicity frame for the reaction $K^-P \rightarrow K^-\pi^+N$ for the combined data at 3.9 and 4.6 GeV/c for the mass of the $K\pi$ system between .84 and .94 GeV.[7]

VII-8a

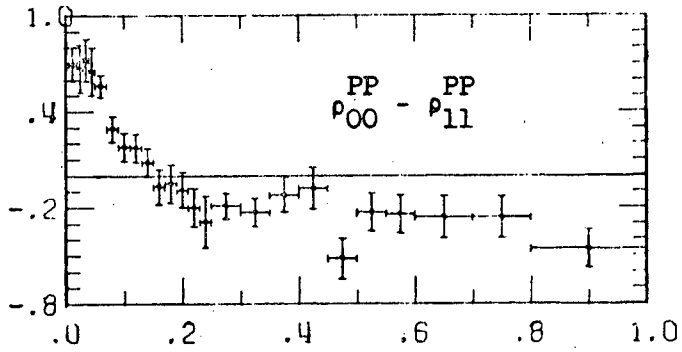

VII-8b

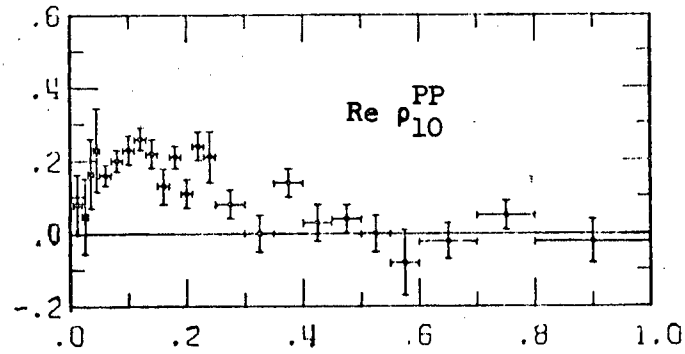

VII-8c

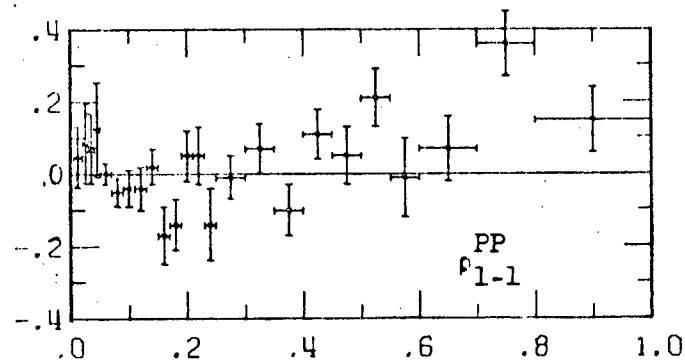

VII-8d

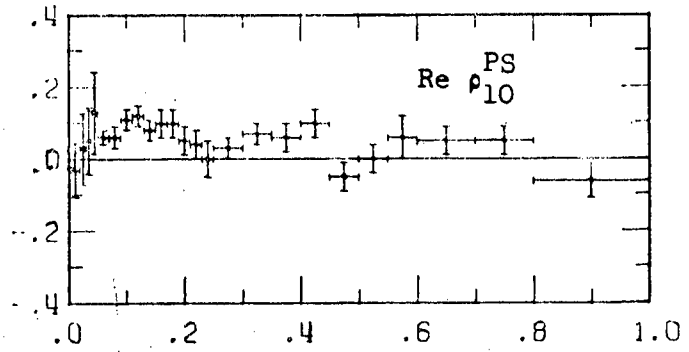

VII-8e

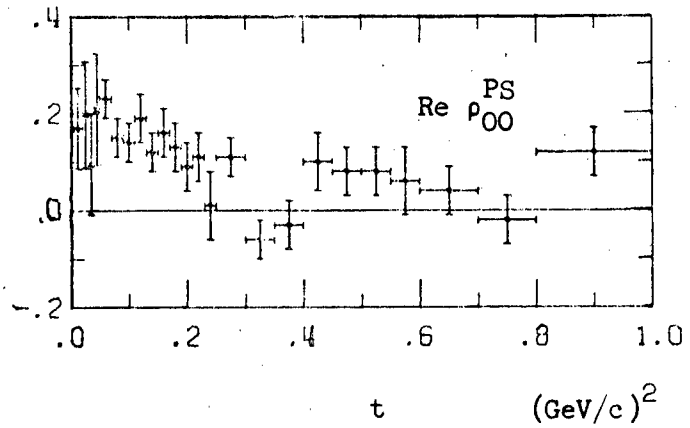

positive, goes slightly negative for t between .06 and .40 $(GeV/c)^2$ and finally ends up positive (see Figure VII-8c). On the other hand ρ^{PP}_{1-1} rises rather abruptly to about .18 at t equal about .07 (GeV/c), and remains roughly constant at this value for larger t values (see Figure VII-7c).

The differences between the t dependences for the helicity density matrix elements for the K^+N and K-P reactions are not easily seen. This is simply a reflection of the fact that for both reactions t channel exchanges dominate and absorptive effects are small. In such cases the t dependence of the density matrix elements in the Jackson frame will be the simplest.

C. Properties of the K*(1420)

In Chapter V the mass dependence of the partial waves contributing to the mass plot was examined. It was concluded that there may be an enhancement in the S-wave. However whether this enhancement is due to an S-wave resonance or a kinematic effect is unclear. In any case the existence of a large S-wave background as well as a smaller amount of P-wave background suggests that the $K^{*o}(1420)$ cross sections, differential cross sections and density matrix elements will depend somewhat upon the method of analysis.

Table V-1 shows the results of fitting the $K^{*o}(1420)$ region for various cuts on the Jackson cosine and t'. None of these fits agree well with the nominal mass of 1422.7 ± 3.8 MeV and width of 101.2 ± 8.4 MeV given by the Particle Data Group for the $K^{*o}(1420)$.[35] Fits by Aguilar-Benitez et al.[7] to the $\overline{K^{*o}(1420)}$ region for K^-P reactions at 3.9 and 4.6

GeV/c yield a mass of 1419.1 ± 3.7 MeV and a width of 116.6 ± 15.5 MeV. The agreement of their fits with the nominal K*(1420) mass and width suggests that the K^-P data does not have the same background problems that are found in the K^+N data.

A shoulder is seen on the low side of the $\overline{K^{*o}(1420)}$ for the 3.9 GeV/c data (see Figures 45 and 47 of Aguilar-Benitez et al.[7]). However this shoulder is much smaller than that seen in the K^+N data at 3.8 GeV/c (see Figure V-1). This suggests that part of the enhancement seen in the K^+N data could be due to a secondary scattering of the decay products of the K*(1420) with the spectator proton.

Table VII-5 gives the masses and widths of the fits described in Section IV-C1 and C2 along with the nominal values and the values from the K^-P reaction at 3.9 and 4.6 GeV/c. The fits of Chapter IV are in reasonable agreement with the nominal mass and width of the K*(1420). The central mass value is somewhat high while the width is somewhat narrow. The comments of Section VI-A apply equally well here when the fits of Chapter IV are compared with the nominal $K^{*o}(1420)$ mass and width. An examination of Figure V-1c shows, however, that in the polar region the $K^{*o}(1420)$ is centered at about 1430 MeV.

The cross section for the $K^{*o}(1420)$ was estimated in several ways for the 1790 events in the mass region 1.2 to 1.64 GeV. The total cross section seen in this region is 600 ± 40 μb. In the first method the mass region was fit using a least squares fit to equation VII-4 where the mass of the K*(1420) was held fixed at 1.43 GeV and the width at .1 GeV. This fit indicates that (35 ± 4)% of the events in the mass region are in the resonance; the corresponding cross section is (310 ± 40) μb for the $(K\pi)^o$

	M (MeV)	Γ (MeV)
fit of IV-C1	1431 ± 3	97 ± 8
fit of IV-C2	1435 ± 3	93 ± 9
K^-P $K^{*o}(1420)$ at 3.9 and 4.6 GeV/c [7]	1419.1 ± 3.7	116.6 ± 15.5
Nominal values from Particle Data Group [35]	1422.7 ± 3.8	101.2 ± 8.4

TABLE VII-5. Table VII-5 shows the mass and width of the $K^{*o}(1420)$ from the fits of Sections IV-C1 and IV-C2 for fits to the 3.8 GeV/c K^+N data as well as the mass and width of the $K^{*o}(1420)$ from the K^-P data at 3.9 and 4.6 GeV/c [7] and from the Particle Data Group.[35]

decay mode after correcting for the unseen decays. The fits of Section IV-C1 and C3 agree with this cross section. The fit of Section IV-C2 indicates that only (22 ± 3)% of the events in the mass region are in the resonance; the corresponding cross section is (200 ± 30) μb for the $(K\pi)^o$ decay mode after correcting for the unseen decays.

For the K^-P reaction the $\overline{K^{*o}(1420)}$ cross section for the $(K\pi)^o$ decays was found to be (340 ± 40) μb.[7] This cross section for the mass region 1.20 to 1.64 GeV was obtained by making a least squares fit to equation VII-4 in which the resonance parameters, the constant C and the coefficients of the linear polynomial were adjusted. The $K^{*o}(1420)$ and $\overline{K^{*o}(1420)}$ cross sections agree well if the $K^{*o}(1420)$ comprises about 35% of the events in the mass region 1.20 to 1.64 GeV for the K^+N reaction.

The differential cross section, $d\sigma/dt'$, for the $K^{*o}(1420)$ production in the K^+N reaction at 3.8 GeV/c was obtained by making t' cuts on the $K\pi$ mass spectrum and then making a background subtraction in the mass region 1.20 to 1.64 GeV. The mass region was fit using a chi square fit to equation VII-5 in the same way that the differential cross section was obtained for the $K^{*o}(890)$ (see Section VII-B2). The mass was set to 1.43 GeV and the width to .1 GeV.

Table VII-6 shows the differential cross section, $d\sigma/dt'$ for the $K^{*o}(1420)$ region for the K^+N reaction at 3.8 GeV/c. Figure VII-9 shows the differential cross section. Figure VII-10 shows the differential cross section, $d\sigma/dt'$, for $\overline{K^{*o}(1420)}$ production in the K^-P reaction at 3.9 GeV/c.

A comparison of $d\sigma/dt'$ for $K^{*o}(1420)$ production and $\overline{K^{*o}(1420)}$ shows that $d\sigma/dt'$ for the $K^{*o}(1420)$ can be fit by a linear exponential while the $\overline{K^{*o}(1420)}$ appears to require a quadratic exponential. The $\overline{K^{*o}(1420)}$ appears to have a steeper forward slope. A linear fit to $\log(d\sigma/dt')$ for $K^{*o}(1420)$ gives a slope of $(4.8 \pm .5)$ $(GeV/c)^{-2}$ with a chi square per degree of freedom of 0.16 for the t' region 0.0 to 1.0 $(GeV/c)^2$. A linear fit to $\log(d\sigma/dt')$ for $\overline{K^{*o}(1420)}$ gives a slope of $(6.5 \pm .08)/(GeV/c)^2$ for the region 0.0 to 0.5 $(GeV/c)^2$ while a fit to the form $bt' + ct'^2$ gives b equal to (8.5 ± 0.3) and c equal to (5.4 ± 0.4) for the region 0.0 to 1.0 $(GeV/c)^2$.[7]

t' region	total number of events	$d\sigma/dt'$ $(mb/(GeV/c)^2)$
.00 - .05	408	1.34 ± .24
.05 - .10	270	.93 ± .20
.10 - .20	332	.79 ± .12
.20 - .30	178	.43 ± .09
.30 - .50	160	.225 ± .042
.50 -1.00	160	.041 ± .017

TABLE VII-6. Table VII-6 shows the differential cross section for the $K^{*o}(1420)$ for the K^+N reaction at 3.8 GeV/c.

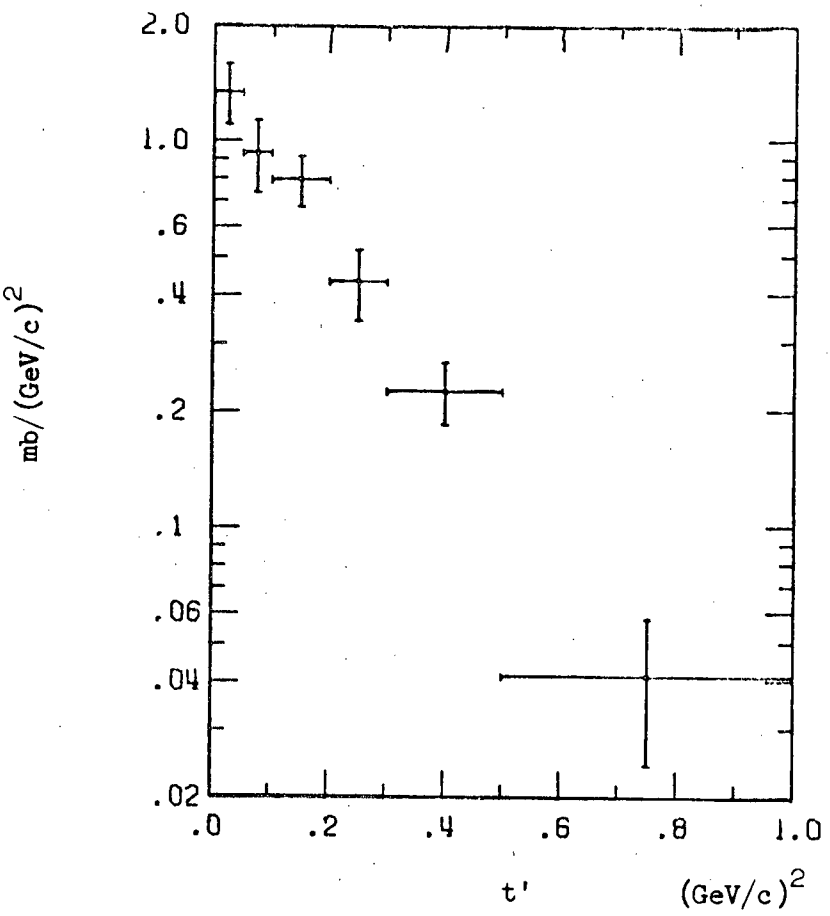

FIGURE VII-9. Figure VII-9 shows the differential cross section, $d\sigma/dt'$, for the $K^{*0}(1420)$ in the K^+N reaction at 3.8 GeV/c. The differential cross section has been corrected for the neutral $K\pi$ mode.

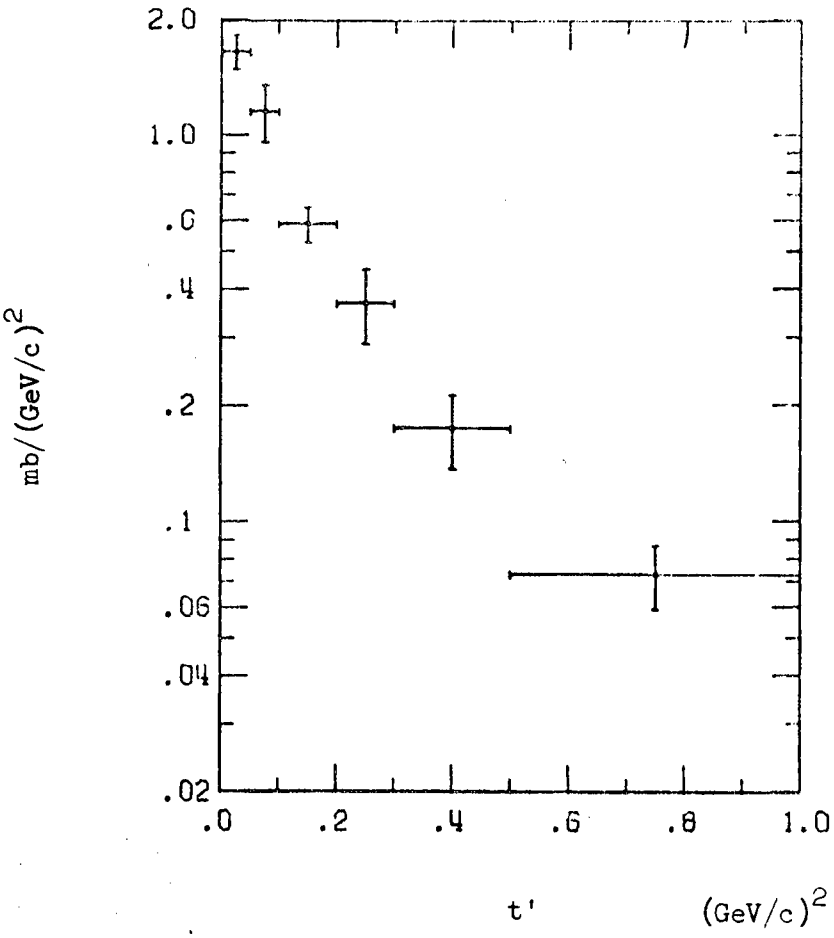

FIGURE VII-10. Figure VII-10 shows the differential cross section, $d\sigma/dt'$, for the $\overline{K^{*0}(1420)}$ in the K^-P reaction at 3.9 GeV/c.

VIII. CONCLUSIONS

In Chapter II the cross section for reaction VIII-1 at 3.8 GeV/c was found to be 1.62 ± .11 mb.

$$K^+N \rightarrow K^+\pi^-P \qquad \text{VIII-1}$$

In Chapter III the general features of reaction VIII-1 were surveyed and it was seen that the reaction is dominated by the quasi-two body interaction VIII-2.

$$K^+N \rightarrow (K\pi)^oP \qquad \text{VIII-2}$$

$K^{*o}(890)$ production is the major feature of the $K\pi$ mass spectrum, however there is a significant amount of $K^{*o}(1420)$ production. There appears to be a shoulder on the low mass side of the $K^{*o}(1420)$ which may be due to an S-wave enhancement (the effect of Firestone et al.[4]). Pion exchange is the dominant exchange mechanism.

Chapter IV presents a method for studying the mass dependence of various partial waves contributing to the $K\pi$ system. The method parameterizes the decay angular distributions well and shows that much information can be gained by studying the interference moments. Fits to the moments do not require that the S-wave resonate in the region of the $K^{*o}(890)$ or that either the S or P-wave resonate in the region of the $K^{*o}(1420)$. There does however appear to be some sort of enhancement in the S-wave slightly below the $K^{*o}(1420)$. A potential model suggests

that only the P, D and F-partial waves have resonances in them and that the S-wave does not have any resonances, although it may have antiresonant behavior. There are some problems about unphysical values for some of the generalized density matrix elements; these problems can only be removed by reformulating the method for studying the mass dependence of the partial waves. These problems also prevent any definite statement from being made about the existence or nonexistence of resonances in lower lying partial waves.

Chapter V studies the $K\pi$ system in the region of the $K^{*o}(1420)$ for the effect reported by Firestone et al.[4] in reaction VIII-1 at 12 GeV/c. The effect was seen, but the interpretation of the effects as a resonance in the S-wave is clouded by a possible interpretation involving a secondary scattering between the spectator proton and the decay products of the $K^{*o}(1420)$.

Chapter VI studies the $K^{*o}(890)$. The density matrix elements for the S and P-partial waves were extracted as a function of t. The one pion exchange model with absorption,[5] OPEA, was found in fair agreement with the t dependence of the quantities $\rho_{00}^{PP}\frac{d\sigma}{dt}$, $\rho_{11}^{PP}\frac{d\sigma}{dt}$, and $Re(\rho_{10}^{PP})\frac{d\sigma}{dt}$; however the model gave the wrong sign for $\rho_{1-1}^{PP}\frac{d\sigma}{dt}$. The t dependence of $\rho_{00}^{PP}\frac{d\sigma}{dt}$ agreed well with a Reggeized one pion exchange model of Abrams and Maor.[6]

Chapter VII compares $K^{*o}(890)$ and $K^{*o}(1420)$ production in reaction VIII-1 at 3.8 GeV/c with $\overline{K^{*o}(890)}$ and $\overline{K^{*o}(1420)}$ production in reaction VIII-3 at 3.9 GeV/c.[7]

In the low t region, differences in the density matrix elements $\rho_{00}^{PP}-\rho_{11}^{PP}$, and Re ρ_{10}^{PP} for $K^{*o}(890)$ and $\overline{K^{*o}(890)}$ production can be understood in terms of the OPEA model. There is some evidence that the $K^{*o}(890)$ cross section is slightly larger than the $\overline{K^{*o}(890)}$ cross section and that the slope for $d\sigma/dt$ is steeper for $K^{*o}(890)$. In the $K^{*o}(1420)$ region, on the other hand, the $\overline{K^{*o}(1420)}$ cross section appears larger and the $K^{*o}(1420)$ has a steeper slope for $d\sigma/dt'$. The $\overline{K^{*o}(1420)}$ signal appears to be much cleaner than the $K^{*o}(1420)$ signal and hence the $K^{*o}(1420)$ cross section and differential cross section depend upon the exact details of the analysis.

REFERENCES

1. G. S. Abrams, L. Eisenstein, J. Kim, D. Marshall, T. A. O'Halloran, Jr., W. Shufeldt and J. Whitmore, Phys. Rev. D 1, 2433 (1970).

2. W. E. Shufeldt, "The K-zero Proton Pi-plus Channel in K-plus Proton Interactions at 3.2 GeV/c," (Ph.D. Thesis) University of Illinois (1970).

3. R. Mercer, P. Antich, A. Callahan, C. Y. Chien, B. Cox, R. Carson, P. Denegri, L. Ettlinger, D. Feiack, G. Goodman, J. Haynes, A. Pevsner, R. Sekulin, V. Speedhar, and R. Zdanis, Nucl. Phys. B32, 381 (1971).

4. A. Firestone, G. Goldhaber and D. Lissauer, PRL 26, 1460 (1971).

5. J. T. Donohue, Phys. Rev. 163, 1549 (1967).

6. G. S. Abrams and U. Maor, PRL 25, 621 (1970).

7. M. Aguilar-Benitez, R. L. Eisner and J. B. Kinson, Phys. Rev. D 4, 2583 (1971).

8. J. Park, "The $K^-\pi^-\pi^+$ System in the Reaction $K^-p \to K^-p\pi^-\pi^+$ at 5.5 GeV/c," (Ph.D. Thesis) University of Illinois (1966).

9. H. Gordon, C. Klabunde, G. Scharf, J. Merrill, (Internal Report) University of Illinois (1970).

10. W. Moninger, "A Study of K^+ Neutron Charge Exchange Scattering Using the Reaction K^+N Goes to PPK^o at 3.8 GeV/c," (Ph.D. Thesis) University of Illinois (1971)

11. L. Eisenstein, "The Reaction $K^+P \to K^+P\pi^+\pi^-$ at 3.2 GeV/c," (Ph.D. Thesis) Harvard University (1969).

12. E. Flanines, J. D. Hanson, D. R. Morrison and N. Lovey, "Compilation of Cross Sections III - K^+ Induced Reactions," CERN/HERA 70-4.

13. M. Firebaugh, "Strange Particle Production in 8 BeV/c Proton-Proton Interactions," (Ph.D. Thesis) University of Illinois (1966).

14. M. R. Robinson, "Coherent Production of the Kaon, Pion, Pion System by Positive 3.8 GeV/c Kaons on Deuterium," (Ph.D. Thesis) University of Illinois (1971).

15. Wonyon Lee, "Charge Exchange Scattering of Positive K Mesons on Deuterons," (Ph.D. Thesis) University of California, UCRL 9691 (1961).

16. R. J. Glauber, Phys. Rev. 100, 242 (1955).

17. G. C. Benson, "Mesons and Spectator Protons in $\pi^+ D \rightarrow \pi^+\pi^-\pi^0 PP$ at 3.65 BeV/c," (Ph.D. Thesis) University of Michigan, COO-1112-4 (1966).

18. M. Moravcsik, Nucl. Phys. 7, 113 (1958).

19. The author wishes to expressly thank D. Brockway for many helpful discussions of the generalized density matrix formalism. All phase conventions are those of Jacob and Wick, Ann. Phys. (N.Y.) 7, 404 (1959).

20. R. Hagedorn, Relativistic Kinematics, W. A. Benjamin, New York, 1964.

21. S. DeBenedetti, Nuclear Interactions, John Wiley and Sons, New York, 1964.

22. J. D. Jackson, Nuovo Cimento 34, 1644 (1964).

23. D. Cords, D. D. Carmony, H. W. Clopp, A. F. Garfinkel, R. F. Holland, F. J. Loeffler, H. B. Mathis, L. K. Kangan, J. Erwin, R. L. Honder, D. E. Pellett, P. Yage, F. T. Meiere and W. L. Yen, Phys. Rev. D 4, 1974 (1971).

24. E. Ferrari and F. Selleri, Nuovo Cimento Suppl. 24, 453 (1962).

25. A. Firestone, G. Goldhaber, D. Lissauer and G. H. Trilling, Phys. Rev. D (to be published) (1972).

26. A. Landé, "Optical Model for Pion Nucleon Scattering," Seminar at University of Illinois, Sept. 15, 1971.

27. A. Messiah, Quantum Mechanics, Vol. 1, John Wiley and Sons, New York (1966).

28. J. V. Beaupre, M. Deutschmann, H. Graessler, P. Schmitz, R. Speth, H. Boettcher, J. Kaltwasser, H. Kaufmann, S. Nowak, A. Angelopoulos, K. W. J. Barnham, J. R. Campbell, V. T. Cocconi, P. F. Dalpiaz, J. D. Hansen, G. Kellner, W. Kittel and D. R. O. Morrison, Nucl. Phys. B28, 77 (1971).

29. J. Benecke and H. O. Dürr, Nuovo Cimento 56A, 269 (1966).

30. C. Schmid, Rapporteur talk given at the Amsterdam Conference on Elementary Particles, June 30-July 6, 1971.

31. A. H. Rosenfeld, A. Barbaro-Galtiere, W. J. Podolsky, L. R. Price, P. Soding, C. G. Wahl, M. Roos and W. Willis, Rev. Mod. Phys. 39, 1 (1967).

32. This data was taken from an international collaboration on K^+P interactions. The principal experimentalists, laboratory and lab momentum for members of the collaboration are listed below.
Y. Goldschmidt-Clermont, F. Muller, Brussels-CERN K^+ collaboration, 3.0 GeV/c.
T. O'Halloran, University of Illinois, 3.2 GeV/c.
Y. Goldschmidt-Clermont, F. Muller, Brussels-CERN K^+ collaboration, 3.5 GeV/c.
N. Gelfand, University of Chicago, 4.27 GeV/c.
G. Goldhaber, University of California, Berkeley, 4.6 GeV/c.
Y. Goldschmidt-Clermont, F. Muller, Brussels-CERN K^+ collaboration, 5.0 GeV/c.
A. Pevsner, John Hopkins University, 5.5 GeV/c.
P. Schlein, H. Ticho, and E. Malamud, University of California, Los Angeles, 7.3 GeV/c.
G. Goldhaber, University of California, Berkeley, 9.0 GeV/c.
J. Mulvey, D. Colley, I. S. Hughes, Biritish K^+ collaboration (Oxford, Birmingham, Glasgow), 10.0 GeV/c.
T. Ferbel, University of Rochester, 12.7 GeV/c.

33. The author is indebted to J. Kim for examining this point in great detail.

34. E. Berger, private communication.

35. A. Rettenberg, A. Barbaro-Galtieri, T. Lasenski, A. H. Rosenfeld, T. G. Trippe, M. Roos, C. Bracman, P. Soding, N. Barash-Schmidt and C. G. Wohl, Rev. Mod. Phys. 43, 51 (1971).

36. D. Lissauer, "K^+D Interactions at 12 GeV/c," (Ph.D. Thesis) University of California, ULRL 20644 (1971).

37. T. A. O'Halloran, private communication.

38. L. R. Price, N. Barash-Schmidt, D. Benary, R. W. Bland, A. H. Rosenfeld, C. G. Wohl, "A Compelation of K^+N Reactions,+ LRL Report No. UCRL-2000, 1969 (unpublished).

39. R. Keyser, "Program to Calculate Cross Sections According to the Peripheral Model," CERN/DD/CO/66/3 (unpublished).

40. M. Aguilar-Benitez, V. E. Barnes, D. Bassano, R. L. Eisner, J. B. Kinson and N. P. Samios, Phys. Rev. Letters 26, 466 (1971).

41. J. D. Jackson and H. Pilkuhn, Nuovo Cimento 33, 906 (1964).

42. S. Goldhaber, J. L. Brown, J. Butterworth, G. Goldhaber, A. A. Hirata, J. A. Kadyk and G. H. Trilling, Phys. Rev. Letters 15, 736 (1965).

43. G. Bassompierre, Y. Goldschmidt-Clermont, A. Grant, V. P. Henri, B. Jongejans, U. Kundt, F. Muller, J. M. Perreau. H. Peotrowska, R. L. Sekulin, J. K. Tuominiemi, J. M. Crispuls, J. Debaisieux, J. DeJongh, M. Delabaye, P. Dufour, F. Gerard, J. Henghebaert, J. Naisse, S. Tavernier, G. Thill, K. Buchmer, G. Dehm, G. Goebel, H. Hupe, T. Joldersoma, I. S. Mittra, W. Wittek and G. Wolf, Nucl. Phys. B16, 125 (1970).

44. A. Firestone, G. Goldhaber, D. Lissauer, "K^{*o} Production in $K^{+}d$ Interactions at 12 GeV/c," LRL Report No UCRL-20076 (unpublished).

45. M. Dickenson, S. Siyashita, D. Huwe, F. Ayer and C. Marshall, Phys. Letters 23, 505 (1966).

46. F. Schweingruber, M. Derrick, T. Fields, D. Griffiths, L. G. Hyman, R. J. Jabbur, J. Loken, R. Annar, R. E. P. Davis, W. Kropac and J. Mott, Phys. Rev. 166, 1317 (1968).

47. Nijmegen-Amsterdam Collaboration Report, 1971 (unpublished).

48. M. Markyton, Nucl. Phys. B10, 193 (1969).

49. B. D. Hyams, W. Koch, D. C. Potter, J. D. Wilson, L. Van Lindern, E. Lorenz, G. Lutgens, U. Stierlin and P. Weilhammer, Nucl. Phys. B7, 1 (1968).

VITA

Don Allen Marshall was [redacted]. After graduating from Moscow High School, Moscow, Idaho in 1961, he attended the University of Oregon for two years. In 1963 he transferred to the University of Idaho where he earned his B.S. in Physics (summa cum laude) in June 1966. During his last year at Idaho, he worked as an NSF Undergraduate Researcher in solid state physics.

Mr. Marshall entered the University of Illinois in 1966 as a NASA Trainee in Physics and earned his Master of Science in Physics in August 1967. He joined the University of Illinois bubble chamber group in 1968 and since September 1969 has worked as a Research Assistant under the direction of Professor T. A. O'Halloran.